EXPLORING THE OPTICAL PROPERTIES OF MIE RESONATOR NANOPARTICLES FOR CATALYTIC AND PHOTOCATALYTIC APPLICATIONS

By

FARSHID MOHAMMADPARAST

Bachelor of Science in Chemical Engineering

Sistan & Baluchestan University

Zahedan, Sistan & Baluchestan

2011

Master of Science in Chemical Engineering
AmirKabir University
Tehran, Tehran
2014

Submitted to the Faculty of the
Graduate College of the
Oklahoma State University
in partial fulfillment of
the requirements for
the Degree of
DOCTOR OF PHILOSOPHY

December, 2021

EXPLORING THE OPTICAL PROPERTIES OF MIE RESONATOR NANOPARTICLES FOR CATALYTIC AND PHOTOCATALYTIC APPLICATIONS

Thesis Approved:

Alan Tree

Thesis Adviser

Mari Andiappan

Seokjhin Kim

Kaan Kalkan

ACKNOWLEDGEMENTS

First I would like to extend my deeply gratitude to my advisor, Dr.Marimuthu Andiappan, These Projects were not possible without his continues support and guidance. Then, I would like to thank Dr. Kaan Kalkan , Dr. Alan Tree, and Dr. Seok-Jhin Kim for serving as my advisory committee members and supporting me in my research projects. I would like to thank my research team members Ravi Teja Addanki Tirumala, Sundaram Bharadwaj Ramakrishnan and Andishaeh Dadgar for their help with the research projects. I would like to thank Brent Johnson and Lisa Whitworth at the Oklahoma State University (OSU) Microscopy Laboratory for their assistance with TEM and SEM. I would like thank Dr. James Puckette for using XRD facility at Nobel Research Centre, Oklahoma State University. I would like to Thank Dr. Steven Harston for his assistance with ESI-MS and HPLC at the OSU DNA and Protein Core Facility. I would like to Thank the staff of School of Chemical Engineering at Oklahoma State University. These projects were supported by grant from the Oklahoma Center for the Advancement of Science and Technology (Award Number # HR18-093). I also would like to thank Oklahoma State University, School of Chemical Engineering for giving me scholarship that supported me in my work.

To My Parents, Words cannot begin to describe my appreciation and gratitude for all you have done for me, for your consistent love and endless support. You have always inspired me to do my best and have supported me in every decision I have made. My Thanks also go to my two sisters, my brother and my friends who helped me and encouraged me through my life.

Name: FARSHID MOHAMMADPARAST

Date of Degree: DECEMBER, 2021

Title of Study: EXPLORING THE OPTICAL PROPERTIES OF MIE RESONATOR NANOPARTICLES FOR CATALYTIC AND PHOTOCATALYTIC APPLICATIONS

Major Field: CHEMICAL ENGINEERING

Abstract: Heterogeneous metal nano catalysts have recently emerged as attractive catalysts for variety of couplings (e.g., C-C, C-N, C-S, C-O, etc.). However, the characterization of catalytic pathway remains challenging. By exploiting localized surface plasmon resonance (LSPR) of catalytically relevant gold (Au) nanostructure, we show UV-Vis spectroscopy can be used to confirm the homogeneous catalytic pathway. Specifically, we have demonstrated that Au nanoparticles under C-C coupling conditions undergo substrate-induced leaching to form homogeneous Au catalytic species. The LSPR spectroscopic approach opens a new door to tracking stability of nano catalysts and characterizing the catalytic pathway in a range of coupling reactions. Furthermore, By exploiting localized surface plasmon resonance of catalytically relevant nanostructures, such as monometallic (Pd, Pt, Ni, Rh, Au, and Cu) nanoparticles and bimetallic core-shell (Ag-Pd) nanoparticles, we show UV-Vis spectroscopy can be used to determine the size of functioning nanocatalyst. Based on our finite-difference time-domain simulations, it is possible to detect leaching of even a monolayer of atoms from the surface of widely used metal nano catalysts with a conventional UV-Vis spectrometer. This sensitive, inexpensive and robust spectroscopic approach can be potentially used as in-line process analytical technology (PAT) in pharmaceutical development and manufacturing.

The ability of plasmonic metal nanostructures (PMNs), such as silver and gold nanoparticles, to manipulate and concentrate electromagnetic fields at the nanoscale is the foundation for wide range of applications, including nanoscale optics, solar energy harvesting and photocatalysis. However, there are inherent problems associated with plasmonic metals, such as high Ohmic losses, and poorer compatibility with the conventional complementary metal-oxide-semiconductor (CMOS) microfabrication processes. These limitations inhibit the broader use of PMNs in practical applications. Herein, we report submicron cuprous oxide and cupric oxide particles can exhibit strong electric and magnetic Mie resonances with extinction/scattering cross sections comparable to or slightly exceeding those of Ag particles. Using size- and shape-controlling particle synthesis techniques, optical spectroscopy, and finite-difference-time-domain simulations, we show that the Mie resonance wavelengths are size- and shape-dependent and tunable in the visible to near-infrared regions. Therefore, submicron copper oxide particles may potentially emerge as high-performance alternatives to PMNs in a wide range of applications.

TABLE OF CONTENTS

Chapter Page

LIST OF TABLES

Table Page

LIST OF FIGURES

Figure Page

CHAPTER I

INTRODUCTION

Background

The field of advanced nanomaterials capable of energy capture, catalysis, and novel electromagnetic properties is one of the most active and promising research areas in advanced materials science. Advanced Nanoparticles exhibit new and improved properties based on specific characteristics such as size, distribution and morphology, and it is possible to tailor the properties of nanoparticles using different preparation methods. Controlling the size and shape of nanoparticles is an ongoing challenge. However, there have been huge efforts and immense developments in the field of advanced Nanomaterials in the recent past years, with numerous methodologies developed to synthesize nano particles of particular shape and size depending on specific applications. Moreover, new applications of advanced nanoparticles and nano catalysts are emerging rapidly. The intrinsic properties of nanoparticles and nano catalysts are mainly determined by size, shape, composition, crystallinity and morphology. The high surface-to-volume ratio along with morphology effects (size and shape) gives nanoparticles distinctively different properties (chemical, electronic, optical, magnetic and mechanical). Functioning advanced nanoparticles and nano catalysts synthesized with various methods are attractive to apply them in many fields. Because of their distinct properties, these materials are offering many new developments in the fields of catalysis, photocatalysis, photovoltaic, optic, biosensor, biomedical, pharmaceuticals, agrochemical, petrochemical and etc. For example, nanotechnology to make various nanoparticles is an enormously powerful technology, which holds a huge promise for the design and development of many types of novel products with its potential medical applications on early disease detection, treatment, and prevention.

Catalysis & Photocatalysis

Nowadays, most of chemical and energy products are produced with catalytic reactions and processes; Agrochemical products, pharmaceutical products, polymers, plastics, textiles, and various other chemicals and renewable energy products are produced through catalytic processes (Figure 1). Extensive number of studies have been carried out in developing catalytic and photocatalytic materials, and immense efforts have been made in understanding the catalytic and photocatalytic processes using various nano catalysts [1–13]. The interest in photocatalysis has been increasing since studies done by Honda and Fujishima in 1972 and Reiche and Bard in 1979[14,15].

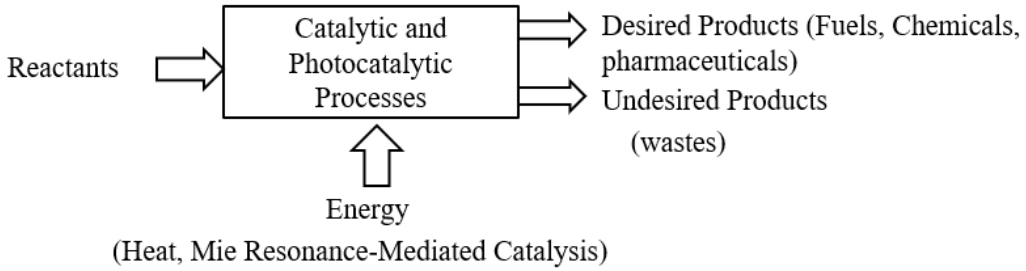

Figure 1. Catalytic and Photocatalytic Processes

In both Fields (catalysis and photocatalysis), the goal is to make nanocatalyst with high activity, stability and selectivity (close to 100% product selectivity. For thermal catalysis to increase the catalyst activity, the principal is to reduce the reduce activation energy of a desired chemical reactions. For photocatalysis, the desired chemical reactions are driven by photoexcitation of a photocatalyst followed by electron/positive hole transfer to reaction substrates (as shown in figure 2 for water splitting). Various photocatalyst nanomaterials and photocatalytic applications have been investigated since then, and considerable works have been devoted into designing and developing photocatalyst nanomaterials with high activity, stability and selectivity for practical applications. For example, the photocatalyzed solar-to-hydrogen conversion (PSC) from water

splitting using TiO_2 photocatalyst has been recently highlighted as a promising method to fully utilize solar energy[16,17].

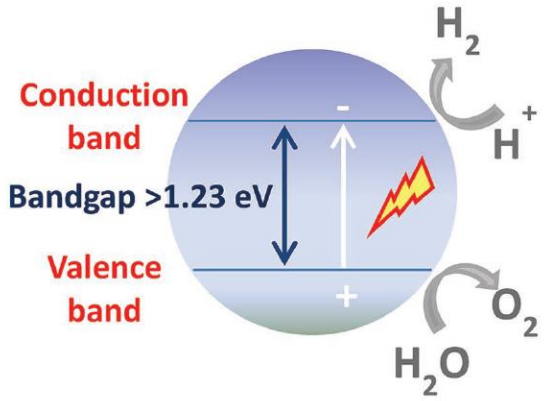

Figure 2. Mie Resonance – Mediated Photo redox Reaction for Water Splitting

When it comes to photocatalyst design and different types of photocatalysts, the catalyst development strategies are mainly centered on maximizing the efficiency by increasing the absorption of light and charge transfer at the surface, and diminishing recombination of charge carrier. The first step for the photocatalysis is the light absorption process, a high-efficient exploitation of the incident light is the main strategy to improve the photocatalytic performance. Light can be scattered and redirected in different directions. Especially, when the size of the particles is comparable to the wavelength of the incident light, the Mie's scattering happens. It is crucial not only to make novel photocatalyst materials and show their high performance but also to know what structural optical properties can enhance the catalytic and photocatalytic activities for finding the optimal Mie resonator nano catalysts. Furthermore, it is necessary to optimize the system design of the Mie resonator nanocatalyst to achieve the optimal photocatalytic efficiency, since a well-designed Mie resonator nanocatalyst can not only improve the reaction performance, but also decrease the waste of energy and catalyst and increase the economic benefit.

Mie Resonance & Mie Resonators (Plasmonic & Dielectric Particles)

According to Mie theory, both plasmonic and dielectric Mie Resonator particles can show strong scattering resonances (as shown in Figure 3). Their scattering optical properties is function of almost two parameters: the dielectric permittivity(ℰ)t and a size parameter q that is proportional to the ratio between the nanoparticle radius (R) and the wavelength of light(ʎ), ($q=2\pi R/ʎ$). The difference between plasmonic and dielectric Mie resonators nanocatalyst is the dielectric permittivity. Dielectric permittivity for plasmonic Mie resonator is negative and for dielectrics Mie Resonator nanocatalyst is positive. Plasmonic Mie resonators generate only localized surface plasmon resonances (LSPR) of an electric type—dipole, quadrupole, etc. Their LSPR response of a magnetic type is almost negligible. While, for dielectric Mie Resonator particles, both electric- and magnetic-type responses have comparable strengths and we can observe both of them at the same time. For both types of Mie Resonator nano catalysts (Plasmonic and dielectric), Strong optical resonances can be achieved with specific geometry (size and shape), This provides tremendous opportunities for designing and developing a variety of Mie Resonator nanostructures with desire optical properties for various applications. Moreover, the strong electric and magnetic resonances in Mie Resonator nanoparticles can pave the way for brining entirely new functionalities to specific geometries in Mie Resonator nanostructures.

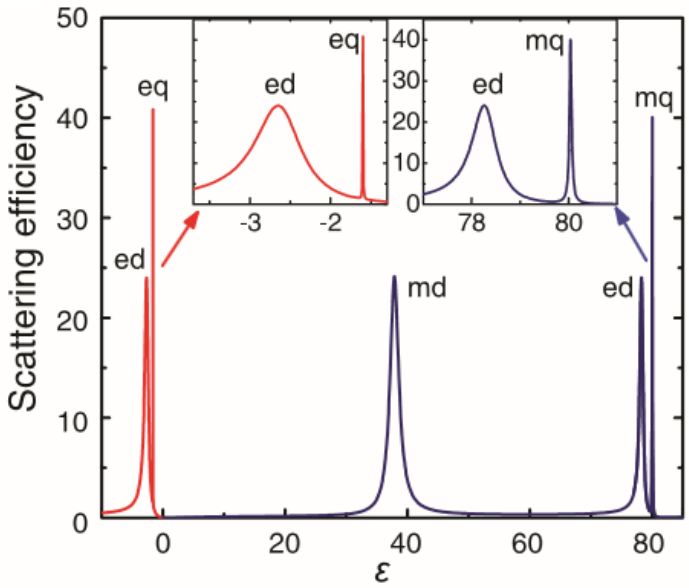

Figure 3. Scattering Efficiency versus Dielectric Permittivity ε for Plasmonic and Dielectric Mie Resonator Materials. (Boris Luk'yanchuk et. Al., Science, 2016).

Although the study of Mie resonances nanostructures has a long history, only recently have researchers started to use these Mie resonances nanostructures as nano catalysts to enhance the performance of catalytic and photocatalytic reactions[13,18–20]. Because of their unique optical properties (electric and magnetic resonances) these Mie Resonator nano catalysts are anticipated to complement or even replace conventional nano catalysts in a range of potential catalytic and photocatalytic applications. By changing the geometrical parameters such as size and shape of the Mie Resonator particles, both electric and magnetic resonances can be tuned.

Variety of strategies have been used to optimize the physical and chemical properties of photocatalysts in order to effectively maximize the light absorption, minimize the recombination of photogenerated charge carriers, and accelerate the charge transfer on the surface functioning Mie Resonator nano catalysts. To meet these goals, our methods and strategies are:

- Size Dependent Optical Properties Studies using different Mie resonator nano catalysts.

- Shape Dependent Optical Properties Studies using different Mie resonator nano catalysts.
- Develop predictive approach that guide us using these optical properties for photocatalytic and photovoltaic applications.

Size and Shape Dependent Optical Properties Studies

When light hits the surface of a Mie resonator nanoparticle, it can be absorbed or scattered (the sum of scattering and absorption is referred to as extinction). Mie Resonance Nanoparticles are in the size and shape regime where the amount of light that is scattered or absorbed can change significantly depending on the particle size and shape. For example, at size less than 15 nm, almost all of the extinction is because of absorption and, at sizes above 150 nm, the extinction is nearly because of scattering. By designing a Mie resonator particle with a specific morphology (size and shape), the optimal amount of scattering and absorption can be achieved. Mie Resonator Nanomaterials exhibit a variety of interesting optical properties that can change significantly with size and shape. By carefully adjusting the size and shape of functioning Mie Resonator nanoparticles, a wide range of optical effects can be produced with many useful applications. For example, the structure of a mie resonator nanocatalyst is known to affect its photocatalytic efficiency, photocatalytic efficiency can be increased or decreased by nanostructure size. The desired optical responses in a Mie resonator nanomaterial depending on the target application, can be generated through several geometry (size and shape) controlled synthesis techniques. Depending on the Mie resonator nanomaterial size and shape, each synthesis procedure provides certain benefits, based on the target application.

The optical absorptions of Mie resonator nanomaterials are characterized by spectroscopic techniques (Uv-vis, Raman and IR spectroscopy) and calculated by optical computational simulations tools such as Finite Difference Time Domaine (FDTD) and COMSOL.

Goal and Specific Aims

In this work, the main aim was to study the optical properties of plasmonic and dielectric nanoparticles both theoretically and experimentally. Far-field effects (extinction, scattering and absorption) and near- field effects (electric and magnetic resonances) for different sizes and shapes of plasmonic Mie Resonator Particles (Au, Ag, pt, pd Rh and Cu) and Dielectric Mie Resonator Particles (Cu_2O, CuO, CeO_2, Fe_2O_3 and TiO_2) were investigated in the wide wavelengths range (UV, visible and near IR spectra range). Finite Difference Time Domaine (FDTD) simulation was presented as an optical computational tool to model the optical properties of plasmonic and dielectric nanostructures. For size and shape optical properties studies, a combination of geometry-controlled synthesis techniques (microemulsion and seeded growth methods) and spectroscopic techniques, and some other characterization tools such Gas Chromatographic Mass Spectroscopy (GC/MS), Electron Spray Ionization Mass Spectroscopy (ESI-MS), Transmission Electron Microscopy (TEM), Scanning Electron Microscopy (SEM), X-Ray Diffraction (XRD), etc..) were utilized. Here, we discuss different types of Mie resonator nano catalysts and their applications and outline various challenges that need to be addressed in the development of practically relevant optimal Mie resonator nano catalysts and systems. At the end, we demonstrate a new approach which can be applied as a useful tool for designing optimal Mie Resonator Nano catalyst with desired optical properties for particular photocatalysis and solar energy harvesting applications.

CHAPTER II

REVIEW OF LITERATURE

Nanomaterials

Nanomaterials are chemical substances or components that are prepared with at least one dimension in nanoscale or all dimensions in the nanoscale. Nanostructured materials are designed and developed to provide the novel and unique properties such as optical, chemical, and physical, compared to other materials without nanoscale features. In the past three decades, nanomaterials exhibited many interesting and promising applications in a wide variety of fields including pharmaceuticals, polymers, agrochemicals, electronics, sensors, photovoltaic devices, drug delivery, catalysis, fuel cells, light-emitting diodes, industrial lithography, quantum dots, quantum devices, optical and biological devices and etc[21–31].Properties of nanoparticles are greatly related to their distinctive shape and size , surrounding media, and fabrication method. Different shapes and sizes of particular nanostructures allow exploring their applications in many fields that include catalysis, photocatalysis, photovoltaics, electronics, sensors, optical devices and etc.

Plasmonic Nanomaterials:

Plasmonic metallic nanostructures have a broad range of applications especially biomedical, energy, catalysis, lithography and information technologies[7,32–36]. They are very attractive for their immense potential applications in various advanced nanomaterial fields, due to their Localized Surface Plasmon Resonance (LSPR) feature.

Localized Surface plasmon Resonances (LSPR) are coherent and collective electron oscillations confined at the dielectric–metal interface. These LSPR plasmon resonances can dramatically harvest the optical field and energy on the nanoscale and greatly improve various light–matter interactions. These properties of surface plasmons strongly depend on the materials and structures, so that plasmonic metals with various morphologies (size and shape) and structures can have distinctive plasmonic wavelengths ranging from ultraviolet, visible, near infrared to far infrared. Because the electric field can be enhanced by orders of magnitude within plasmonic structures, various light–matter interaction processes including photocatalysis, solar energy conversion, heat generation, and optical conversion can be greatly enhanced and these have been investigated and confirmed by both theoretical computational and experimental studies [37–39].

Several physical, chemical and biological synthesis procedures have been employed to increase the performance of plasmonic metal nanoparticles showing improved properties with the aim to have a better control over the particle size, distribution and morphology [40–42]. Chemical reduction is the most common, stable, and high yield used method for the fabrication of plasmonic metal nanoparticles[43–45]. The reduction of metal ions (+) in aqueous solution generally yields colloidal metal with particle diameters in nanoscale. The synthesis of plasmonic metal nanoparticles by chemical reduction techniques are performed in the presence of stabilizers in order to prevent unwanted agglomeration of the colloidal metal nanoparticle solution. One of the recent, high conversion and ideal technique for the preparation of plasmonic nanoparticle like gold is seeded-growth method[46–49]. In the present study, plasmonic metallic nanoparticles were synthesized by seeded-growth and chemical reduction methods at room temperature.

Furthermore, in this work, with combination of computational and experimental studies we investigated and discussed the optical properties of different plasmonic metallic nanostructures, with a hope to deliver guidelines for making future high-performance plasmonic nanostructures for various applications, and technologies.

Dielectric Nanomaterials

As plasmonic nanomaterials find novel applications in different fields, dielectric nanoparticles are not an exemption due to their unique optical and chemical properties. They can be easily polarized when subjected to electrical field, degree of polarization is measured by electromagnetic fields enhancement. This quantity also determines the electric permeability of the dielectric material. The larger dielectric constant results in more electromagnetic field enhancement and energy storage capacity. Due to lack of free electrons, conductivity for these materials is low. The band gap energy is high above 3ev, and they possess high refractive index. They have very promising applications both in photovoltaic and photocatalysis fields[50–53].

In this work, variety of dielectric nanomaterials were prepared and analyzed. Two main synthesis methods were micro-emulsion and chemical reduction. Furthermore, in this work, with combination of computational and experimental studies we investigated and discussed the optical properties of different dielectric nanostructures, with a hope to deliver guidelines for making future high-performance dielectric nanostructures for photocatalysis and photovoltaic applications.

Optical Properties

The plasmonic and dielectric nanoparticles optical properties are mostly influenced by size and shape[24,40,42,54–56]. For plasmonic nanostructure, the size and shape dependence on the optical properties of nanoparticles is the result of two distinct phenomena: Surface plasmon resonance for metals – Increased energy level spacing due to the confinement of delocalized energy states. In metal nanoparticles, the quasi-continuous density of states in valence and conduction bands divides into separate electronic levels, the layout between these levels is increasing with decreasing in particle size. In metal nanoparticle, the sea of electrons behaves like a fluid and will move under the influence of an electric field. If the electric field is oscillating (like a photon), then the sea of electrons will oscillate too. These oscillations are quantized and resonate at a specific frequency. Such oscillations are called surface plasmons. Surface Plasmons are the coherent excitation of free electrons in a metal. Metals can be modeled as an arrangement of positive ions surrounded by a sea

of free electrons. The plasmon resonance frequency (f) depends on particle size, shape, and material type. The optical properties of metal nanoparticles are dominated by the interaction of surface plasmons with incident photons. Surface Plasmons – Metal nanoparticles like gold and silver have plasmon frequencies in the visible range. When white light impinges on metal nanoparticles the wavelength corresponding to the plasmon frequency is absorbed. The spectral locations, strengths, and number of plasmon resonances for a given particle depend on the particle's shape and size. For the dielectric materials, this phenomenon is different, because there is the band gap in bulk state. This band gap increases when the particle size is decreased. In dielectric materials, the valance band corresponds to the ground states of the valance electrons. The conduction band corresponds to excited states where electrons are a free to move about in the material and participate in conduction. In order for conduction to take place in a dielectric material, electrons must be excited out of the valance band, across the band gap into the conduction band. This process is called carrier generation. Conduction takes place due to the empty states in the valence band (holes) and electrons in the conduction band.

Surface Area to Volume Ratio

Nanoparticles have a much greater surface area per unit volume ratio compared with the materials made up of bigger particles. The surface area to volume ratio for a material or component made of nanoparticles has a great effect on the properties of the functioning material. Nanoparticles exhibit unique properties due to their high surface area to volume ratio. Large surface area to volume ratio of nanomaterials provides many opportunities for designing new and novel materials for various applications. For example, they can be used as nano catalysts in pharmaceutical and petrochemical processes or be applied in thin solar cells for harvesting more fraction of solar energy[21,25,57–59]. The effectiveness of a drug or automobile catalytic converters is dependent upon surface area available for interaction or reaction. Most of the chemical reactions and interactions are dependent upon the amount of surface area available for the reaction. Thermal transfer, optical response, and electrical conduction are also properties that are dependent on surface area of functioning nanomaterial.

Plasmonic and Dielectric Nanomaterials Applications

Photocatalysis & photovoltaic

The global current energy crisis encourages us to find a new pollution-free, sustainable energy source. Solar energy is the most promising one to provide the future energy demand as the energy that comes from the sun is in limitless amount. Photocatalysis and photovoltaics are the main important processes for the conversion of solar energy, which transform and/or store photon energy to chemical bonds and electricity, respectively. Dielectric and plasmonic nanostructures have been proven as an effective and promising nanomaterial to absorb the solar light and act as subwavelength antennas to concentrate light[7,18,37,60]. These advantages motivate implementation of dielectric and plasmonic nanostructures as promising platforms for photocatalysis and photovoltaics applications.

Optic and Data Storage

The optical resonant behavior of plasmonic nano-structures or nano-particles in the presence of ultraviolet, visible, and near-infrared light was used for the purpose to achieve high data storage density and retrieving the stored information. Plasmonic nanostructures have high potential application for optical data storage[61–66]. Various plasmonic nanostructures using various synthesis techniques with nanoscale dimensions have been fabricated and have shown considerable enhancement in data storage due to resonance and charge transfer effects.

Biomedical

The dielectric and plasmonic nanoparticles have gained great interest as a new platform for biomedical application, because of unique, tunable and functional optical properties and convenient surface bioconjugation with molecular probes related with the resonance effects. Dielectric and plasmonic nanocomposites have been widely investigated and used for biomedical application, since they exhibited promising potential for biomedical applications such as imaging, sensing, and photothermal therapy [67–71]. For example ,by utilizing the plasmonically enhanced Rayleigh scattering from gold or silver nanoparticles targeted to specific cell components, it has been

possible to obtain the real-time cellular imaging of cancer cells during the complete cell cycle [72].Although functional nanomaterials have significantly enhanced the overall performances of biocompatibility, some particular characteristics, including electromagnetic properties, as well as resonance effects still need be further investigated and improved.

Pharmaceutical

The rapid pace of advancements in the field of advanced nanoparticles/ nano catalysts has driven innovations in all the disciplines of science including pharmaceuticals where cutting-edge research is carried out for the development of novel nano catalysts including plasmonic nanostructures. The pharmaceutical companies are significantly interested on using advanced nanoparticles to find out the solutions for the ongoing challenges in the pharmaceuticals and come up with novel and low cost engineered nano catalysts for product development. This focus is opening new opportunities in different segments of pharmaceutical R&D. Plasmonic nanoparticles can act as efficient nano catalysts and support a wide variety of pharmaceutical reactions such as coupling reactions[41,49,73–75] . The Pharmaceutical product development involves the discovery and development of new plasmonic nanoparticles as heterogeneous nano catalysts and hence, it is an area of continuous and committed research.

In this study, plasmonic gold nanoparticle catalysts have been utilized in C-C coupling reaction, to find that gold nanoparticles are efficient catalysts for coupling reaction. Furthermore, we measured amount of leaching of functioning gold nanocatalyst under the C-C coupling reaction condition.

Lithography

Among all nanoparticles, only plasmonic nanoparticles have great potential to be used in lithography field. Plasmonic nanostructures such as gold and silver have been used as masks for lithography. Plasmonic nanolithography is a nanofabrication technique which exploits surface plasmons to generate subdiffraction patterns[76–78].

CHAPTER III

METHODOLOGY

Preparation of Gold (Au) Nanocatalyst -seeded growth synthetic method

The quasi-spherical Au nanoparticles were synthesized using a seeded growth synthetic approach reported in the literature.[79,80] The growth solution was prepared by adding 52 mg of precursor, gold chloride trihydrate [$HAuCl_4*3H_2O$] to 370 mL DI water. Next, 6 grams of cetyltrimethylammonium bromide (CTAB) was added to the solution. The solution under stirring was then heated on a hot plate to 70˚C.Seed preparation**:** In order to make seeds, 180 mL of the growth solution was kept aside. To this solution, 20 mL of an aqueous solution containing 15 mg of sodium citrate was added first, followed by 6 mL of the aqueous solution containing 24 mg of sodium borohydride. This seed solution was then stirred for 1 hour at room temperature to allow enough time for the seed particles to grow. The size of seed particles synthesized using this procedure averages approximately 3 nm in diameter.

Growth of Gold nanoparticles: First, 88 mg of ascorbic acid was added to 5 mL of DI water. Then 0.1 mL of this solution was added to 18 mL of the growth solution. Then, 2 mL of seed solution prepared before was added to the 18 mL of growth solution with ascorbic acid and stirred for 15 min. This procedure yielded Au nanospheres of approximately 7-8 nm in diameter.

In order to make large Au nanoparticles, 180 mL of growth solution is stirred with additions of 1 mL ascorbic acid stock solution (88mg/5mL) and the small nanoparticle solution prepared before. This solution was stirred at room temperature for 1.5 hours. After the nanoparticles were grown, the solution was chilled to 0˚C with an ice water bath in order to allow enough time for the crystallization of CTAB. The solution was then centrifuged as close to 0˚C as possible to settle out the CTAB crystals. The nanoparticle suspension was then transferred to a rotary evaporator to concentrate the solution for use in reactions. The evaporation conditions were set at a bath temperature of 95˚C, a vacuum of 300 mmHg and 60 rpm. This procedure allowed good concentration without excessive aggregation of the nanoparticles. The solvent was evaporated until 120 mL was left. This solution was used for catalyzing C-C coupling reaction.

Preparation of Cu_2O Nanocatalyst – Microemulsion Method

Microemulsion method for Cu_2O spheres: The spherical Cu_2O particles were prepared using the water-in-oil microemulsion synthesis method. In this method, n-heptane, polyethylene glycol-dodecyl ether (Brij, average Mn ~362), copper nitrate, and hydrazine were used as the continuous oil phase, surfactant, copper precursor and reducing agent, respectively. These chemicals were added in the following sequence and quantity. First, 7.75 mL of n-heptane was added to three-neck round bottom flask at room temperature, followed by 1.15 mL of Brij surfactant. During the process of surfactant addition, the system was stirred vigorously, then 0.81 mL of 0.1 M copper nitrate aqueous solution was added, followed by 0.81 mL of 1 M of aqueous hydrazine solution. To understand the evolution of extinction spectra as a function of particle size, samples were taken at different time intervals for UV-Vis-near IR extinction measurements.

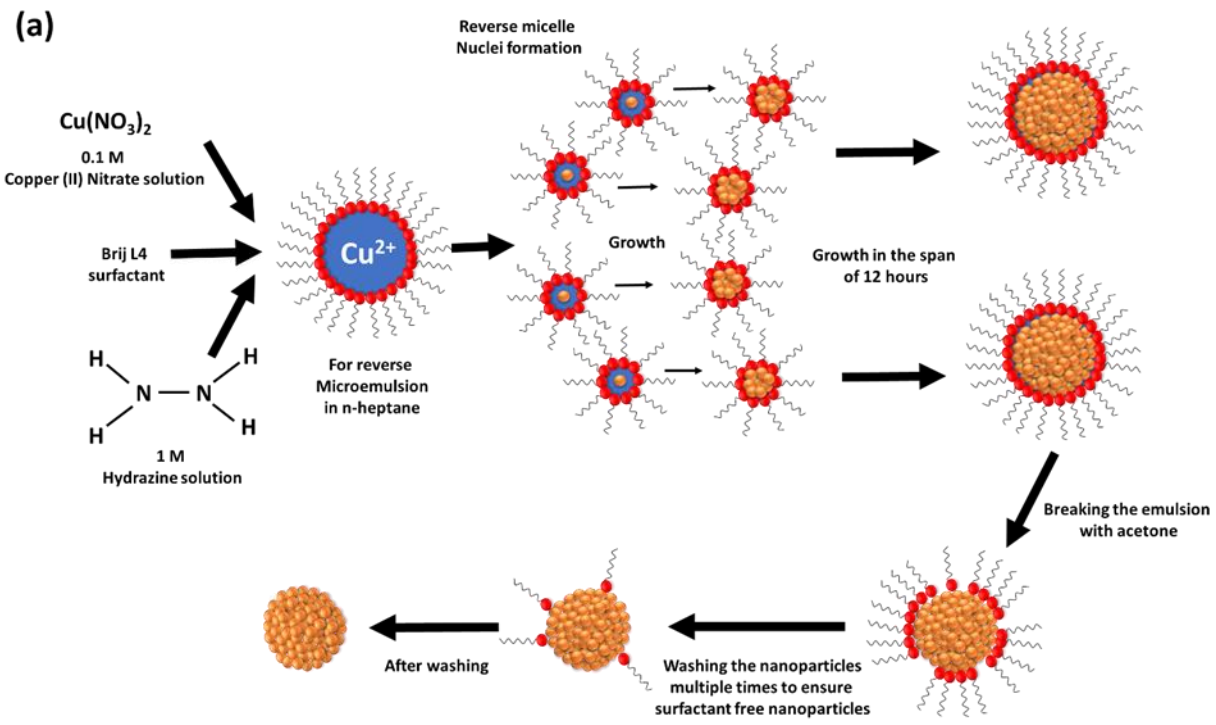

Figure 4. Microemulsion method for making Cu_2O spheres.

Representative Procedure for Coupling Reaction

Procedure for C-C coupling reaction: The homocoupling of phenylacetylene was selected as a model reaction. The reaction procedure started with the addition of concentrated Au nanoparticle solution to 24 mL of dimethylformamide (DMF) in the three neck round bottom flask. The solvent mixture in the flask after this addition was 17%/83% (volume %) mixture of DMF/water. The solution was heated to 85˚C while stirring in a round bottom flask. 2 mL of reactant, phenylacetylene (PA, 18.2 mmol) and 2 grams of potassium carbonate (K_2CO_3) were then added under stirring. To predict the size of functioning Au nanocatalyst in the reaction sample, operando UV-Vis extinction measurements were acquired at frequent time intervals. The transmission electron microscopy (TEM) images of Au nanoparticle samples of the reaction mixture at the respective reaction time were taken using JEOL JEM-2100. The reaction conversion was measured

using gas chromatography-mass spectrometry (GC-MS, Shimadzu QP2010SE) system with helium as the carrier gas with a 5% polar column.

Finite Difference Time Domain (FDTD) simulation

We utilized a reliable and widely used Lumerical FDTD package to perform FDTD simulations.[81,82] The in-build material model in the program Au-Palik was used for the optical constants of Au. This material model in the program is based on the experimental data (real and imaginary parts of the refractive index at different wavelengths), rather than an analytic model. For the experimental data, the program uses the real and imaginary parts of the refractive index values taken from Palik handbook.[83] For small size of nanoparticles, the surface-scattering effect may play a role.[84] This effect is not captured in the Lumerical FDTD simulations. The simulations were used to calculate the extinction cross section for the nanostructures as a function of the incident wavelength. The boundary conditions used for the simulations were periodic in the x,y directions and perfectly matched layer (PML) in the z direction. The extinction cross sections as a function of wavelengths were calculated using the total-field/scattered-field (TFSF) formalism. The incident light source used for the simulation was Gaussian source in the simulated wavelength region. For Au simulations, the box sizes used for simulation box, scattered-field monitor, TFSF source, total-field monitor were 100, 60, 50 and 40 nm, respectively. The TFSF source was set to originate from +z direction. The mesh size used for the simulations was 0.1 nm. To predict the change in gold nanoparticle size for growth and leaching processes, the percentage change in extinction intensity calculated at LSPR peak wavelength is matched to that of experimental value measured from UV-Vis extinction spectra.

The LSPR spectrum of metal nanoparticles of a given size is characterized by extinction intensity, peak wavelength and full width at half maximum (FWHM). Therefore, when the nanoparticles undergo leaching of surface atoms, changes in these characteristics can be exploited to trace the

change in the size of the nanoparticles. To investigate how these characteristics, change as a function of nanoparticle size, we utilized finite-difference time-domain (FDTD) simulations. Through the analysis of the LSPR peaks, we quantified the changes in values of FWHM, peak position, and extinction intensity as a function of size of the nanostructure. We have found that extinction intensity at LSPR peak wavelength can be a sensitive measure to determine the change in nanostructure size. The representative results show the size of Au nanospheres as a function of percentage change in extinction intensity at LSPR peak wavelength of 515 nm. If the diameter of an Au nanosphere is reduced from 10 to 9.5 nm (e.g., due to leaching), there will be approximately 12% decrease in the corresponding extinction intensity at LSPR wavelength of 515 nm. In the case of most later transition metals, change of 0.5 nm in diameter can easily account for leaching of approximately one monolayer of surface atoms (See monolayer calculations section for more details). The optical properties for Pd, Pt, Ni, Rh, Au and Cu were all taken from optical properties data bank by Palik.[85] The boundary conditions used for the simulations were periodic in the x,y directions and perfectly matched layer (PML) in the z-direction. The extinction cross sections as a function of wavelengths were calculated using the total field/scattered-field (TFSF) formalism (Table 1).[86,87] The incident light source used for the simulation was a Gaussian source in the simulated wavelength region. To predict the optical behavior of Cu_2O, CuO, TiO_2, CeO_2, and Fe_2O_3 particles of varying sizes and shapes, we utilized the Lumerical FDTD package. The optical data were obtained from Palik.[85]. The procedures for FDTD simulations, Cu_2O, CuO, TiO_2, CeO_2, and Fe_2O_3 particles preparation, and UV-Vis extinction are mentioned as below.

The optical properties of Cu_2O, CuO, TiO_2, CeO_2, and Fe_2O_3 were taken from Palik.[85] The real (n) and imaginary (k) parts of the refractive index used in the simulations for Cu_2O . CuO, CeO_2, TiO_2, and Fe_2O_3 are shown in Table 2,3,4, and 5. The boundary conditions used for the simulations were perfectly matched layer (PML) conditions in the x, y, and z directions. For the simulations of extinction, scattering, and absorption spectra, the respective cross sections as a function of wavelengths were calculated using the total-field/scattered-field (TFSF) formalism. The incident

light source used for these simulations was the Gaussian source in the simulated wavelength region. For the simulations of the magnetic and electric field distributions, a plane wave was used for electromagnetic field incidence with propagation in the x-axis direction, and polarization along the y-axis and the z-axis for the electric field and the magnetic field, respectively. For all the simulation results shown in the main draft, the simulations were performed for Cu_2O. CuO, CeO_2, TiO_2, and Fe_2O_3 particles in a surrounding medium with the refractive index of 1. Monolayer calculations: For Au, Ni, Pt, Rh, Pd and Cu spherical nanoparticles, the parameters used are shown below:

Gold

Atomic radii: 0.166 nm

1 monolayer =0.166 x 2 = 0.332 nm

Expected change in particle diameter due to leaching of 1 monolayer of surface atoms =

$$2 * 0.332\ nm = 0.664\ nm$$

Nickel

Atomic radii: 0.163 nm

1 monolayer =0.163 x 2 = 0.326 nm

Expected change in particle diameter due to leaching of 1 monolayer of surface atoms = $2 * 0.326\ nm = 0.652\ nm$

Platinum

Atomic radii: 0.175 nm

1 monolayer =0.175 x 2 = 0.350 nm

Expected change in particle diameter due to leaching of 1 monolayer of surface atoms = $2 * 0.350\ nm = 0.700\ nm$

Rhodium

Atomic radii: 0.200 nm

1 monolayer = 0.200 x 2 = 0.400 nm

Expected change in particle diameter due to leaching of 1 monolayer of surface atoms = $2 * 0.400\ nm = 0.800\ nm$

Palladium

Atomic radii: 0.163 nm

1 monolayer =0.163 x 2 = 0.326 nm

Expected change in particle diameter due to leaching of 1 monolayer of surface atoms = $2 * 0.326\ nm = 0.652\ nm$

Copper

Atomic radii: 0.128 nm

1 monolayer = 0.128 x 2 = 0.256 nm

Expected change in particle diameter due to leaching of 1 monolayer of surface atoms = $2 * 0.256\ nm = 0.512\ nm$

Formulae for percentage (%) change in extinction

1) The percentage decrease in extinction (i.e., scattering + absorption) at LSPR wavelength for monometallic nanoparticles is calculated based on the following formulae

$$\%\ change = \frac{E_{intial} - E_{final}}{E_{intial}} * 100$$

where $E_{initial}$ and E_{final} are extinction values of initial and final particle sizes, respectively.

2) The percentage increase in extinction at LSPR wavelength for bimetallic core-shell Ag-Pd nanoparticles is calculated based on the following formulae

$$\%\ change = \frac{(E_{final} - E_{intial})}{E_{intial}} * 100$$

where E_{final} and $E_{initial}$ are extinction values of final and initial particle sizes, respectively.

Table 1. FDTD simulated values of extinction cross section at the dominant LSPR peak wavelength for Au, Ni, Pt, Rh, Pd and Cu nanoparticles (NP) of various sizes.

Particle Size (nm)	Extinction Cross section of Au NP (m^2)	Extinction Cross section of Ni NP (m^2)	Extinction Cross section of Pt NP (m^2)	Extinction Cross section of Rh NP (m^2)	Extinction Cross section of Pd NP (m^2)	Extinction Cross section of Cu NP (m^2)
12.5	7.87×10^{-17}	1.46×10^{-16}	8.73×10^{-17}	2.18×10^{-16}	2.74×10^{-16}	4.84×10^{-17}
12	6.95×10^{-17}	1.30×10^{-16}	7.78×10^{-17}	1.95×10^{-16}	2.42×10^{-16}	4.29×10^{-17}
11.5	6.07×10^{-17}	1.15×10^{-16}	6.83×10^{-17}	1.72×10^{-16}	2.14×10^{-16}	3.81×10^{-17}
11	5.35×10^{-17}	9.97×10^{-17}	5.95×10^{-17}	1.49×10^{-16}	1.87×10^{-16}	3.29×10^{-17}
10.5	4.64×10^{-17}	8.77×10^{-17}	5.23×10^{-17}	1.30×10^{-16}	1.63×10^{-16}	2.87×10^{-17}
10	3.99×10^{-17}	7.43×10^{-17}	4.44×10^{-17}	1.11×10^{-16}	1.41×10^{-16}	2.48×10^{-17}
9.5	3.42×10^{-17}	6.38×10^{-17}	3.79×10^{-17}	9.45×10^{-17}	1.22×10^{-16}	2.16×10^{-17}
9	2.92×10^{-17}	5.44×10^{-17}	3.23×10^{-17}	8.19×10^{-17}	1.04×10^{-16}	1.83×10^{-17}
8.5	2.45×10^{-17}	4.63×10^{-17}	2.74×10^{-17}	6.9×10^{-17}	8.76×10^{-17}	1.53×10^{-17}
8	2.02×10^{-17}	3.78×10^{-17}	2.25×10^{-17}	5.65×10^{-17}	7.33×10^{-17}	1.28×10^{-17}
7.5	1.67×10^{-17}	3.2×10^{-17}	1.89×10^{-17}	4.75×10^{-17}	6.08×10^{-17}	1.08×10^{-17}
7	1.38×10^{-17}	2.56×10^{-17}	1.53×10^{-17}	3.82×10^{-17}	4.97×10^{-17}	8.69×10^{-18}
6.5	1.1×10^{-17}	2.07×10^{-17}	1.21×10^{-17}	3.07×10^{-17}	4×10^{-17}	6.94×10^{-18}
6	8.72×10^{-18}	1.58×10^{-17}	9.45×10^{-18}	2.33×10^{-17}	3.17×10^{-17}	5.5×10^{-18}
5.5	6.74×10^{-18}	1.23×10^{-17}	7.35×10^{-18}	1.78×10^{-17}	2.46×10^{-17}	4.32×10^{-18}
5	4.99×10^{-18}	8.98×10^{-18}	5.4×10^{-18}	1.34×10^{-17}	1.87×10^{-17}	3.8×10^{-18}

Table 2. The refractive index values of Cu_2O and CuO used in the simulations.[85]

	Cu_2O		**CuO**	
Wavelengths (nm)	**n**	**k**	**n**	**k**
300	2	1.85	2.18	1.5
350	2.4	1.44	2.24	1.03
400	2.8	0.99	2.34	0.87
450	3.06	0.6	2.45	0.77
500	3.12	0.35	2.54	0.68
550	3.1	0.19	2.58	0.59
600	3.02	0.13	2.65	0.5
650	2.9	0.1	2.72	0.4
700	2.83	0.083	2.88	0.31
750	2.77	0.07	2.97	0.22
800	2.7	0.06	2.94	0.11
850	2.66	0.053	2.81	0.04
900	2.63	0.048	2.74	0.03
950	2.61	0.043	2.69	0.02
1000	2.6	0.04	2.65	0.01
1100	2.59	0.033	2.61	0
1200	2.58	0.027	2.58	0
1300	2.57	0.021	2.57	0
1400	2.57	0.017	2.56	0
1500	2.57	0.013	2.56	0
2000	2.56	0.002	2.55	0

Table 3. The real (n) and imaginary (k) parts of refractive index values of CeO_2 used in the simulations.[88]

CeO_2											
λ (nm)	**n**	**k**	**λ (nm)**	**n**	**k**	**λ (nm)**	**n**	**k**	**λ (nm)**	**n**	**k**
401	2.47	0.11	624	2.16	0.00	854	2.13	0.00	929	2.12	0.00
410	2.41	0.08	635	2.15	0.00	864	2.13	0.00	940	2.12	0.00
421	2.38	0.03	646	2.15	0.00	876	2.13	0.00	951	2.12	0.00
429	2.36	0.02	657	2.15	0.00	886	2.13	0.00	962	2.11	0.00
439	2.31	0.01	668	2.15	0.00	897	2.12	0.00	973	2.11	0.00
450	2.29	0.01	679	2.15	0.00	908	2.12	0.00	984	2.11	0.00
461	2.28	0.00	690	2.15	0.00	919	2.12	0.00	996	2.11	0.00
471	2.25	0.00	701	2.15	0.00	929	2.12	0.00	929	2.12	0.00
483	2.24	0.00	712	2.14	0.00	940	2.12	0.00	940	2.12	0.00
494	2.22	0.00	722	2.15	0.00	951	2.12	0.00	951	2.12	0.00
504	2.21	0.00	733	2.15	0.00	962	2.11	0.00	962	2.11	0.00
516	2.20	0.00	744	2.14	0.00	973	2.11	0.00	973	2.11	0.00
526	2.19	0.00	755	2.14	0.00	984	2.11	0.00	984	2.11	0.00
537	2.18	0.00	766	2.14	0.00	996	2.11	0.00	996	2.11	0.00
548	2.18	0.00	777	2.14	0.00	854	2.13	0.00	929	2.12	0.00
559	2.18	0.00	788	2.14	0.00	864	2.13	0.00	940	2.12	0.00
570	2.18	0.00	799	2.13	0.00	876	2.13	0.00	951	2.12	0.00
581	2.17	0.00	810	2.14	0.00	886	2.13	0.00	962	2.11	0.00
592	2.16	0.00	821	2.13	0.00	897	2.12	0.00	973	2.11	0.00
602	2.16	0.00	831	2.13	0.00	908	2.12	0.00	984	2.11	0.00
613	2.16	0.00	842	2.13	0.00	919	2.12	0.00	996	2.11	0.00

Table 4. The real (n) and imaginary (k) parts of refractive index values of α-Fe_2O_3 used in the simulations.

	α-Fe_2O_3	
λ (nm)	**n**	**k**
400	2.756	1.294
450	3.181	1.02
500	3.282	0.675
550	3.318	0.498
600	3.265	0.149
650	3.074	0.057
700	2.972	0.031
750	2.903	0.021
800	2.853	0.02
850	2.824	0.027
900	2.805	0.024
950	2.789	0.022
1000	2.775	0.015
1050	2.759	0.011
1100	2.745	0.011
1150	2.734	0.01
1200	2.723	0.011

89

Table 5. The real (n) and imaginary (k) parts of refractive index values of TiO_2 used in the simulations.[90,91]

TiO_2								
λ (nm)	**n**	**k**	**λ (nm)**	**n**	**k**	**λ (nm)**	**n**	**k**
180	1.37	1.998	330	5.291	1.5698	480	3.08	0.0001
190	1.535	1.831	340	4.969	1.0926	490	3.054	0.0001
200	1.536	1.696	350	4.477	0.6508	500	3.03	0.0001
210	1.46	1.65	360	3.87	0.251	510	3.014	0.0001
220	1.433	1.806	370	3.661	0.033	520	3	0.0001
230	1.443	2.084	380	3.498	0.0001	530	2.985	0.0001
240	1.363	2.454	390	3.375	0.0001	540	2.97	0.0001
250	1.365	2.847	400	3.286	0.0001	550	2.954	0.0001
260	1.627	3.197	410	3.225	0.0001	560	2.94	0.0001
270	1.952	3.432	420	3.186	0.0001	570	2.929	0.0001
280	3.355	3.561	430	3.162	0.0001	580	2.92	0.0001
290	3.835	3.535	440	3.149	0.0001	590	2.91	0.0001
300	4.732	3.28	450	3.141	0.0001	600	2.9	0.0001
310	5.235	2.734	460	3.13	0.0001	610	2.889	0.0001
320	5.391	2.076	470	3.104	0.0001	620	2.88	0.0001

TiO_2								
λ (nm)	**n**	**k**	**λ (nm)**	**n**	**k**	**λ (nm)**	**n**	**k**
630	2.875	0.0001	780	2.8	0.0001	930	2.759	0.0001
640	2.87	0.0001	790	2.794	0.0001	940	2.76	0.0001
650	2.86	0.0001	800	2.79	0.0001	950	2.761	0.0001
660	2.85	0.0001	810	2.79	0.0001	960	2.76	0.0001
670	2.844	0.0001	820	2.79	0.0001	970	2.755	0.0001
680	2.84	0.0001	830	2.785	0.0001	980	2.75	0.0001
690	2.835	0.0001	840	2.78	0.0001	990	2.749	0.0001
700	2.83	0.0001	850	2.78	0.0001	1000	2.75	0.0001
710	2.825	0.0001	860	2.78	0.0001	1010	2.75	0.0001
720	2.82	0.0001	870	2.775	0.0001	1020	2.749	0.0001
730	2.814	0.0001	880	2.77	0.0001	1030	2.749	0.0001
740	2.81	0.0001	890	2.77	0.0001	1040	2.748	0.0001
750	2.81	0.0001	900	2.77	0.0001	1050	2.747	0.0001
760	2.81	0.0001	910	2.765	0.0001	1060	2.747	0.0001
770	2.806	0.0001	920	2.76	0.0001	1070	2.746	0.0001

TiO_2								
λ (nm)	**n**	**k**	**λ (nm)**	**n**	**k**	**λ (nm)**	**n**	**k**
1080	2.745	0.0001	1230	2.729	0.0001	1380	2.721	0.0001
1090	2.744	0.0001	1240	2.729	0.0001	1390	2.721	0.0001
1100	2.742	0.0001	1250	2.728	0.0001	1400	2.72	0.0001
1110	2.741	0.0001	1260	2.728	0.0001	1410	2.719	0.0001
1120	2.74	0.0001	1270	2.727	0.0001	1420	2.719	0.0001
1130	2.739	0.0001	1280	2.727	0.0001	1430	2.718	0.0001
1140	2.738	0.0001	1290	2.726	0.0001	1440	2.717	0.0001
1150	2.737	0.0001	1300	2.726	0.0001	1450	2.716	0.0001
1160	2.736	0.0001	1310	2.725	0.0001	1460	2.715	0.0001
1170	2.735	0.0001	1320	2.725	0.0001	1470	2.714	0.0001
1180	2.734	0.0001	1330	2.724	0.0001	1480	2.713	0.0001
1190	2.733	0.0001	1340	2.724	0.0001	1490	2.711	0.0001
1200	2.732	0.0001	1350	2.723	0.0001	1500	2.71	0
1210	2.731	0.0001	1360	2.723	0.0001			
1220	2.73	0.0001	1370	2.722	0.0001			

Characterization Techniques

Uv-Vis Spectroscopy

UV-Vis extinction spectra were acquired using an Agilent Cary 60 Spectrophotometer. In-operando measurements were taken using a dip probe accessory and a fiber optic coupler with a stainless-steel tip. To predict the size of functioning Au nanocatalyst in the reaction sample, operando UV-Vis extinction measurements were acquired at frequent time intervals. The in-operando measurements were taken during growth of Au nanospheres at room temperature in aqueous solution. The data sampled for all Au growth measurements was from 800-300 nm with sampling every 0.5 nm and a scan speed of 300 nm/min. For sampled UV-Vis measurements, 100 µL was taken from the reaction mixture and diluted into 10 mL of 200 proof ethanol. This diluted sample was then used for UV-Vis spectra. For the spherical Cu_2O particles, all UV-Vis-near IR extinction spectra were taken using an Agilent Cary 60 Spectrophotometer. 150 µL of the synthesis mixture was diluted into 2 mL of deionized water. This diluted sample was then used for UV-Vis-near IR extinction measurements.

Gas Chromatography- Mass Spectroscopy (GC-MS)

The reaction solution was characterized by GC-MS . GC-MS samples were prepared by diluting 100 µL of the reaction mixture into 10 mL of dichloromethane. Reaction data was collected on a Shimadzu QP2010SE GC-MS system with helium as the carrier gas with a 5% polar column. The GC-MS spectrum of diphenyldiacetylene (DPDA) observed in reaction mixture taken from Au nanoparticles-catalyzed homo-coupling of phenylacetylene. The main manuscript shows the PA conversion as a function of reaction for the homocoupling reaction. Shimadzu C184-E037A GC Column (Phase: SH-Rxi™-5Sil MS Column, Length-30 m; ID – 25 mm; df – 0.25 µm) was used for gas chromatography. The column has an operating temperature range of -60°C to 350°C. Peak detection and integration were handled by the software provided by Shimadzu Corporation.

Identification was verified using NIST spectral libraries with matching higher than 95%. No smoothing was used to process the samples to ensure accurate peak identification and quantification. The calibration curve was built using area versus concentration response from prepared reference samples.

The conversion was calculated based on the equation shown below:

$$Conversion\ (X, \%) = \frac{C_{A0} - C_A}{C_{A0}} * 100$$

where CA0 is the initial concentration (in mmol) of reactant (i.e., PA) and CA is the concentration at any time, t.

Electron Spray Ionization Mass Spectroscopy (HR-ESI-MS)

The reaction solution was also characterized using HR-ESI-MS. HR-ESI-MS spectra of the reaction samples were collected on a LTQ Orbitrap system with an ESI source. HR-ESI-MS spectra for the reaction was collected on a LTQ Orbitrap system with an ESI source. The spray voltage was set at 5.0 kV with 15.0 mL/min sample flow rate. The sample was prepared by mixing 1 mL of sample with 1 mL of a mixture of 18 mL DCM, 2 mL Acetone, 400 µL DI water. The sample was sprayed with nitrogen as the sheath and auxiliary gas. Figure S4 shows the predicted isotope distribution for the proposed gold complex, $[Au(PA)_2]^-$.

X-Ray Diffraction (XRD)

XRD patterns were acquired using a Philips X-Ray diffractometer (Phillips PW 3710 mpd, PW2233/20 X-Ray tube, Copper tube detector – wavelength - 1.5418 Angstroms), operating at 45 KW, 40 mA.

Transmission Electron Microscopy (TEM)

TEM images were taken using JEOL JEM-2100. The system is equipped with a LaB6 gun and accelerating voltage of 200 kV. Samples were prepared by taking 100 µL of growth or reaction mixture and diluting into 2 mL of 200 proof ethanol. This dilution solution was sonicated to

ensure good dispersion. Next 10 µL was taken and placed onto a copper mesh carbon background TEM grid. The ethanol was allowed to evaporate at room temperature.

CHAPTER IV

FINDINGS

Tracing Stability and Monitoring Particle Size of Functioning Mie Resonator Nanocatalyst Using Localized Surface Plasmon Spectroscopy

Heterogeneous metal nano catalysts have recently emerged as attractive catalysts for variety of couplings (e.g., C-C, C-N, C-S, C-O, etc.). However, the characterization of catalytic pathway remains challenging. By exploiting localized surface plasmon resonance (LSPR) of catalytically relevant gold (Au) nanostructure, we show UV-Vis spectroscopy can be used to confirm the homogeneous catalytic pathway. Specifically, we have demonstrated that Au nanoparticles under C-C coupling conditions undergo substrate-induced leaching to form homogeneous Au catalytic species. The LSPR spectroscopic approach opens a new door to tracking stability of nano catalysts and characterizing the catalytic pathway in a range of coupling reactions.

Metal-catalyzed coupling reactions (MCCRs) have found widespread application in premier organic synthesis from pharmaceutical compounds to polymers.[73,74] MCCRs have been traditionally carried out by homogeneous Pd-complexed catalysts.[74,75] However, Pd and most of the ligands associated with the homogeneous catalysts are toxic.

Therefore, conventional homogeneous Pd-catalyzed processes typically require several expensive downstream unit operations to reduce the metal residue below the maximum allowable level in the final product (e.g., active pharmaceutical ingredient, API).[92–94] In recent years, heterogeneous metal nano catalysts have emerged as high-performance alternatives to conventional homogenous complexes to drive coupling reactions.[41,73,95–116] For example, nano catalysts built on Au, Cu, Pd and their alloys can drive variety of couplings (e.g., C-C, C-N, C-S, C-O, etc.) and exhibit excellent yield, catalytic activity and broad substrate scope.[49,95–103,117–124] These catalysts do not require ligands and are in general not sensitive to air and moisture. They have the potential to reduce the need for the expensive downstream operations for separating the metal catalyst from the final product (e.g., API).

While recent years have witnessed a growing demand for nano catalysts, there is also a continuing controversy whether the catalysis occurs on the surface of nanoparticles (i.e., heterogeneous pathway) or on leached metal ions in solution (i.e., homogeneous pathway). Therefore, characterization of catalytic pathway and determination of nanocatalyst stability under relevant reaction conditions remain ongoing challenges within the field.[49,95–103,117–124] The leaching of surface atoms into solvent can depend on the reaction temperature, size of the nanoparticle, nature of the solvent, substrate, base, and stabilizer.[49,125] A common leaching test used to determine nanocatalyst stability mainly employs filtration. This test involves post-catalytic analysis of the leached metal atoms in the filtered supernatant reaction solution using techniques such as inductively coupled plasma mass spectrometry (ICP-MS) and characterization of the spent nanocatalyst using transmission electron microscopy (TEM). This test has several drawbacks; for example, it has been reported that the leached metal atoms can redeposit quickly onto the catalyst during filtration and may not be detected in the supernatant solution.[117]

Herein, for coupling reaction involving Au nanoparticles, we propose an alternative method, which is based on localized surface plasmon resonance (LSPR). LSPR of metal nanoparticles can conveniently be monitored by ultraviolet-visible (UV-Vis) light extinction spectroscopy.[7,18,36,126,127]

Specifically, the LSPR spectrum of metal nanoparticles of a given average size is characterized by a certain extinction intensity, peak wavelength and full width at half maximum (FWHM). Therefore, when the nanoparticles undergo leaching of surface atoms, changes in these characteristics can be exploited to trace the change in the average size of the nanoparticles.[128]

The homocoupling reaction of PA was carried out at 85 ºC using potassium carbonate (K_2CO_3) and 83/17 (volumetric ratio) mixture of water/dimethylformamide (DMF) as base and solvent, respectively. The samples of reaction mixture were taken at frequent time intervals for UV-Vis extinction spectra measurements and TEM imaging. In Figure 5, we show the UV-Vis extinction spectra of reaction mixture measured before the addition of substrate (i.e., PA) and at different reaction times. Upon addition of phenylacetylene, the LSPR peak is attenuated along with the appearance of new peaks in the 400-500 nm region. It has been shown that organometallic complexes of noble metals exhibit absorption peaks in this region.[129,130] After PA addition, the LSPR peak of Au NPs also red-shifts slightly as seen from Figure 5. This adsorbate-induced red-shift in LSPR peak position is due to the expected adsorbate-induced change in the dielectric constant of the surrounding medium.[127,131] The decrease in LSPR extinction and the appearance of new extinction peaks in the 400-500 nm region suggest that the phenylacetylene is inducing a leaching process from the surface of the Au nanoparticles and forming soluble Au complexes in the reaction solution. It is worth mentioning here that the leaching of Au nanoparticles has also been confirmed in the literature using other spectroscopic techniques such as inductively coupled plasma mass spectrometry and X-ray photoelectron spectroscopy for similar reaction conditions in Au nanoparticle catalyzed Sonogashirah coupling between phenylacetylene and iodobenzene.[49] It could be argued that the changes observed in the UV-Vis extinction spectra may be due to Au nanoparticle aggregate formation. However, when there is aggregate formation, an additional lower energy LSPR peak is expected for Au aggregates. Since the UV-Vis extinction spectra in Figure 5 does not show any such features, we rule out any significant aggregation formation.[132]

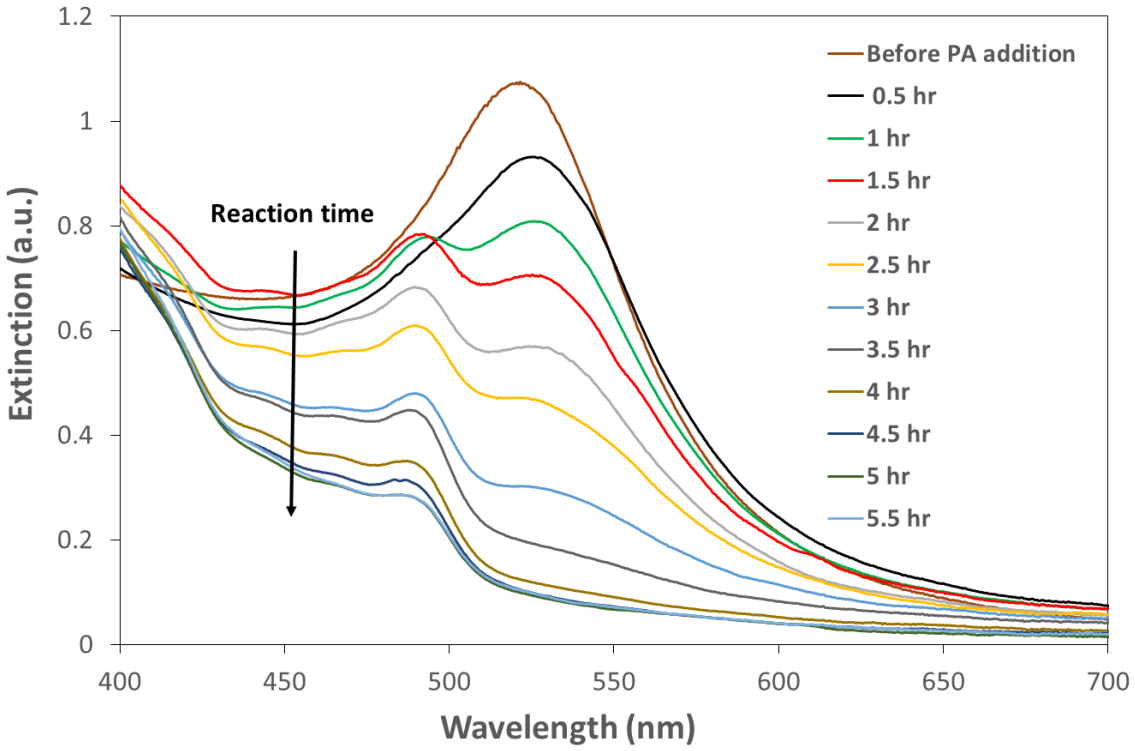

Figure 5. UV-Vis extinction spectra of reaction mixture measured before the addition of phenylacetylene (PA, 0 hour) and at different reaction times during homocoupling of phenylacetylene.

We also verified that the reactant (i.e., PA) and the expected homocoupling product, diphenyldiactyelene (DPDA), exhibit absorption peaks only in the 200-350 nm region and do not exhibit any absorption features in the 400-500 nm region (Appendix , see Figure S1).[128,133] Therefore, the new extinction peaks observed in the 400-500 nm region are most likely due to the different Au homogeneous catalytic species that participate in the homogeneous catalytic cycle.

To identify the soluble Au complexes, present in the reaction solution, we performed high-resolution electrospray ionization mass spectrometry (HR-ESI-MS) on the supernatant solution of reaction solution. In the HR-ESI-MS spectrum (Figure 6a and Appendix Figure S4), we observe seven negative ions in the m/z range of 400. Five of these ions have a fractional mass of 0.22 and

the other two ions (with m/z = 399.04 and 400.04) have a fractional mass of 0.04. These fractional masses indicate that these ions are derived from two different compounds. Since the ions with fractional mass of 0.22 give an isotope distribution inconsistent with gold's single isotope, we disregard them for further consideration. The ions with fractional mass of 0.04 give an isotope distribution consistent with that predicted for $[Au(PA)_2]^-$ compound, and the mass error for the predicted compound is less than 5 ppm.[128] We have also analyzed the reaction samples with gas chromatography-mass spectrometry (GC-MS) and confirmed the presence of homocoupling product, DPDA in the solution . The leaching of Au nanoparticles and the presence of a homogenous Au species confirm the homogeneous catalytic pathway contribution for the homocoupling of phenylacetylene (PA) investigated in this study. Although these results confirm the contribution of the homogeneous catalytic pathway in Au nanoparticles mediated C-C coupling of PA, we do not rule out the possible heterogeneous pathway that can happen in parallel.

To further support our conclusions that Au complexes can catalyze the homocoupling reaction, we carried out the reaction using the supernatant solution containing homogeneous Au complexes as the only catalytic species. The homocoupling reaction of PA was first carried out using Au nanoparticles, and reaction progress was monitored using GC-MS. The DPDA was observed as the only product of the homocoupling of PA. When the PA conversion was ~52%, the reaction was stopped, and Au nanoparticles were removed from the reaction solution using centrifugation. The reaction was then allowed to continue, and PA conversion was monitored in the supernatant solution containing homogeneous Au complexes. Figure 6.b shows PA conversion observed as a function of reaction time from this experiment. The results shown in Figure 6.b confirm that the homogeneous Au complexes can indeed catalyze the homocoupling reaction to 100% conversion.

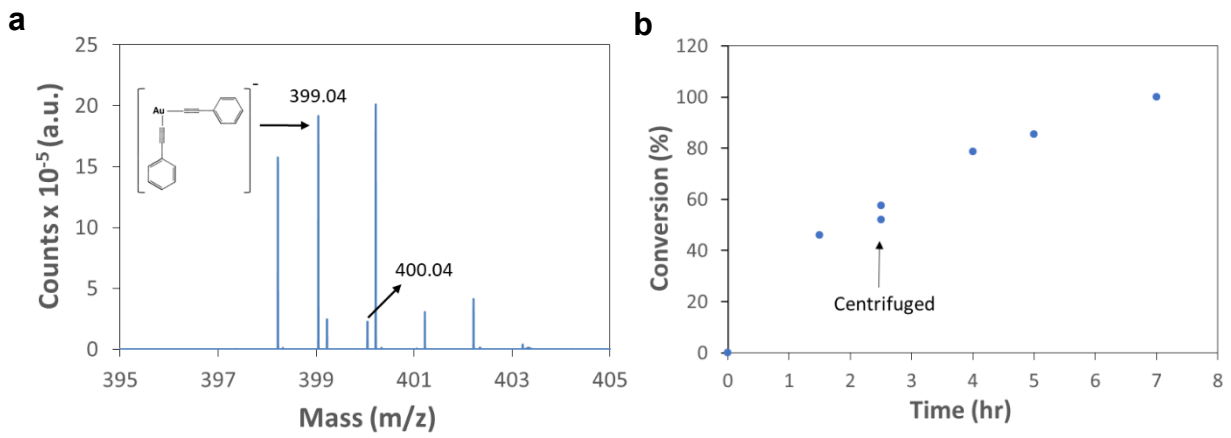

Figure 6. (a) Representative HR-ESI-MS spectrum of supernatant solution of reaction mixture taken from Au nanoparticles-catalyzed homo-coupling of phenylacetylene. **(b)** Reaction conversion as a function of reaction time for the homo-coupling of phenylacetylene.

To test the applicability of LSPR spectroscopy to predict the average size of Au nanoparticles in the reaction samples, the samples collected after 1, 1.5, 2 and 2.5 hours of reaction were characterized using TEM to determine the average size of nanoparticles, and the deconvoluted LSPR peaks of the respective Au nanoparticle samples were matched with finite-difference time-domain (FDTD) simulations. We utilized a reliable and widely used Lumerical FDTD program to perform FDTD simulations.[81,82] The in-build material model in the program Au-Palik was used for the optical constants of Au. This material model in the program is based on the experimental data (real and imaginary parts of the refractive index at different wavelengths), rather than an analytic model. For the experimental data, the program uses the real and imaginary parts of the refractive index values taken from Palik handbook.[83]

Figure 7a shows the simulated extinction spectra that are matched with LSPR spectra of Au nanoparticles. In Figure 7b, we show the comparison between Au nanoparticle sizes predicted from LSPR responses and average nanoparticle sizes measured from TEM for different reaction samples collected as a function of reaction time. As seen from Figure 7b, the LSPR-predicted and TEM-measured average sizes matches well. We also show in Figure 7c, the representative particle size

distributions measured from TEM for the reaction samples collected after 1.0 and 2.5 hours of reaction. The decreasing trend in average particle size in Figure 7b along with shift in particle size distribution towards smaller sizes in Figure 7c further confirm the leaching of Au nanoparticles during the homocoupling reaction.

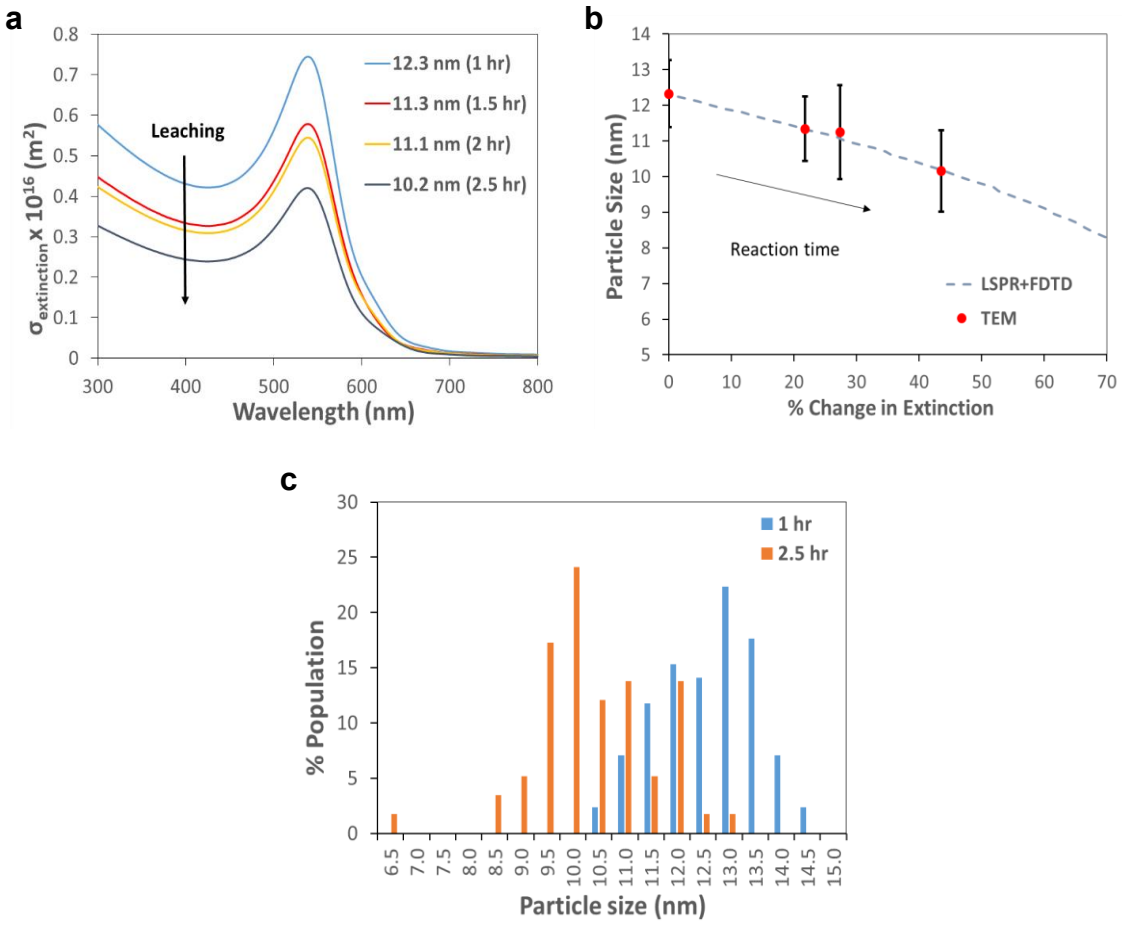

Figure 7. (a) Simulated LSPR responses for the leaching of Au spherical nanoparticles. The legend shows the reaction time and the predicted average size of Au nanoparticles in the respective reaction sample. **(b)** Average size of Au nanoparticles predicted from LSPR responses and FDTD simulations for different reaction samples as a function of % change in extinction intensity of the respective samples at LSPR peak wavelength. For comparison, TEM-measured average sizes of Au nanoparticles are also shown. **(c)** Size distributions of Au nanoparticles

measured from TEM images for the reaction samples collected after 1 and 2.5 hours of C-C homocoupling reaction.

We also investigated the applicability of LSPR spectroscopy for nanoparticle growth systems. For this system, we selected the growth of spherical Au nanoparticles using a seeded growth approach.[134]In this approach, we prepared quasi-spherical Au nanoparticles (average size = 8.0 nm and standard deviation in size distribution = 0.6 nm), and used those as seeds for growth. Figure 8a shows the representative TEM image of seed nanoparticles. We also show the representative TEM image of larger nanoparticles obtained at the end of growth process. For the growth of larger nanoparticles, a known amount of growth solution comprised of gold precursor was added step-by-step to the seed solution. For each addition, in-operando UV-Vis extinction spectra measurements were made and TEM samples were taken to determine the LSPR response and average size of nanoparticles, respectively. Figure 8b shows the in-operando extinction spectra of Au nanoparticles measured during this growth process. Figure 8c shows the representative particle size distributions measured from TEM for the seed and larger Au nanoparticles obtained at the end of the growth process. In-operando LSPR responses acquired for each addition during the growth process were matched with FDTD-simulated results to predict Au nanoparticle size for each growth step.[128] The comparison between nanoparticle sizes predicted from in-operando LSPR responses and average nanoparticle sizes measured from TEM is shown in Figure 8d. The shift in particle size distribution towards larger sizes in Figure 8c along with increasing trend in average particle size in Figure 4d confirm the growth of Au nanoparticles. Figure 8d shows that there is also a consistency between TEM analysis and the LSPR spectral changes for seeded growth of the particles.

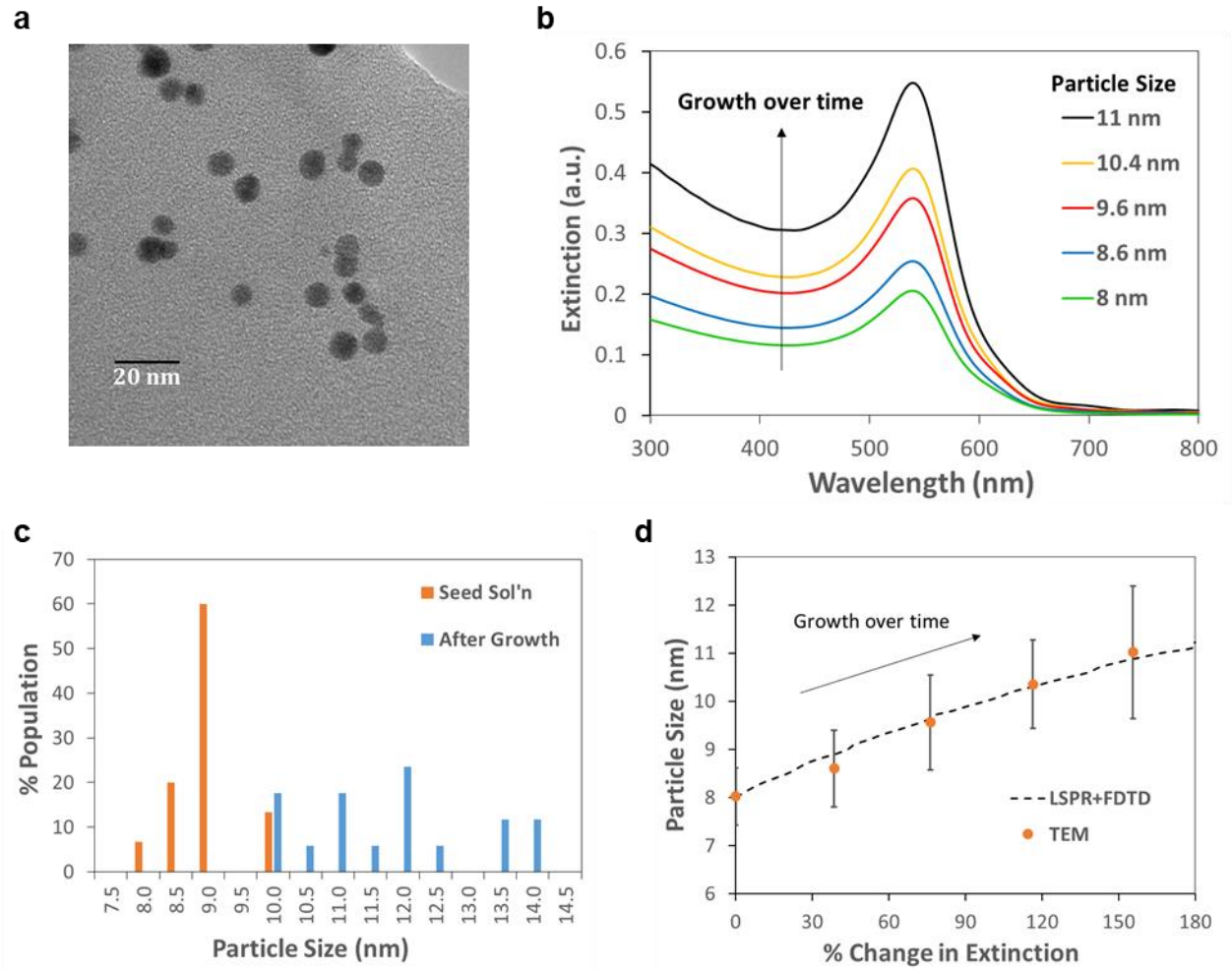

Figure 8. (a) Representative TEM image of spherical Au nanoparticles used as seeds for growth. **(b)** In-operando UV-Vis extinction spectra that show LSPR responses for growth of Au spherical nanoparticles from seed nanoparticles of 8.0 nm average diameter. The legend shows the predicted average size of Au nanoparticles in the respective samples. **(c)** TEM-measured size distributions of seed and larger Au nanoparticles obtained at the end of growth process. **(d)** Average size of Au nanoparticles predicted from LSPR responses and FDTD simulations for each growth step as a function of % change in extinction intensity at LSPR peak wavelength. For comparison, TEM-measured average sizes of Au nanoparticles are also shown.

By exploiting localized surface plasmon resonance (LSPR) of catalytically relevant Mie Resonator gold (Au) nanostructure for the selected C-C coupling reaction, we have shown that UV-Vis spectroscopy can be used to trace the stability, and to monitor size of functioning Mie Resonator nanocatalyst or nanoparticles during reaction. Determination the particle size from the instrument response to single particles was challenging because of the complicated dependence of the response on particle size and particle shape. A new model or approach was developed to determine particle size of nanoparticle from experimental extinction light measurements and computational optical responses. There was a clear relationship between particle size and scattered and extinction intensity.To predict nanoparticle size correctly with high accuracy, optical experimental and simulation studies were compared, in both investigations. This spectroscopic approach opens a new door to tracking stability of nano catalysts and characterizing the catalytic pathway in a range of metal-based catalyzed reactions. This methos provides new insight into distinguishing homogeneous and heterogeneous catalytic pathways, percentage contribution of each of them. Furthermore, the need to measure particle size of functioning nanoparticle has increased dramatically over the last few decades in various fields including catalysis, semiconductors, chemical manufacturing, pharmaceuticals, medicine, solar energy and air & water pollution. Therefore, the same experimental and simulation model is recommended for measuring and predicting particle size of functioning nanoparticle.

Operando UV-Vis Spectroscopy as Potential In-line PAT System for Testing Quality of Drug Molecules

Metal nanoparticle-catalyzed reactions such as hydrogenation, cross-coupling, carbonylation, and hydroformylation reactions are the most widely used reactions in the pharmaceutical and fine chemical industries. However, there is no operando spectroscopic technique that exists to monitor the size of functioning nanocatalyst. By exploiting localized surface plasmon resonance of catalytically relevant nanostructures, such as monometallic (e.g., Pd, Pt, Ni, Rh, Au, and Cu)

nanoparticles and bimetallic core-shell (e.g., Ag-Pd) nanoparticles, we show UV-Vis spectroscopy can be used to determine the size of functioning nanocatalyst. Based on our finite-difference time-domain simulations, it is possible to detect leaching of even a monolayer of atoms from the surface of widely used metal nano catalysts with a conventional UV-Vis spectrometer. This sensitive, inexpensive and robust spectroscopic approach can be potentially used as in-line process analytical technology (PAT) in pharmaceutical development and manufacturing.

Transition metal-catalyzed coupling reactions and metal nanoparticle-catalyzed hydrogenation reactions are the most widely used reactions in the pharmaceutical and fine chemical industries [135–153]. The hydrogenation reactions are conventionally performed using supported metal nano catalysts such as palladium (Pd), platinum (Pt) and nickel (Ni) nanoparticles supported on inert supports such as alumina, silica or carbon in batch or packed-bed reactors [139,154,155]. In contrast, the cross-couplings have been conventionally carried out by homogeneous palladium Pd-catalyzed batch processes. Compared to the conventional batch processes, the continuous processes have the potential to (i) reduce manufacturing cost, (ii) improve product quality, (iii) lower waste generation, (iv) shrink the manufacturing facility space, and (v) decrease fluctuations in production ("A Snapshot of Priority Technology Areas Across the Federal Government,"). Given these advantages, in recent years, heterogeneously catalyzed cross-couplings have been of great interest since they can be used as a platform to switch cross-couplings from traditional batch mode to continuous flow mode. In that vein, metal nano catalysts such as Pd, Au, Cu, and their alloys have also recently emerged as promising catalysts to drive a variety of cross-coupling reactions such as C-C, C-N, C-S, C-O, and C-Se couplings with excellent yield and broad-substrate scop. Heterogeneous metal nano catalysts have also been reported as high-performance alternatives to the conventional homogeneous catalysts to catalyze a wide range of other reactions such as carbonylation and hydroformylation [140,157].

Although the metal nanoparticles have emerged as high performance alternatives to the conventional homogeneous catalysts, the characterization and predictability of the performance of the nanoparticle-catalyzed systems such as packed bed systems still remain an ongoing challenge in pharmaceutical process development [139,140,154,158]. One main reason for this difficulty is that the metal nanoparticles generally undergo leaching during the reaction and results in a change in the size of functioning nanocatalyst as a function of time. Since the critical reaction parameters such as conversion, impurity levels and leached metal content in the outlet reaction stream mainly depend on the size and total surface area of the nanocatalyst in the catalyst bed, the real-time monitoring of the size of the nanocatalyst is critical to design a robust process. However, there is no operando spectroscopic technique that exists, as of today, to monitor the size of functioning nanocatalyst.

Herein, for nanoparticle-catalyzed reactions involving metal nanoparticles such as Pd, Pt, Ni, Cu, Au, and their alloys, we propose an operando ultraviolet-visible (UV-Vis) light extinction spectroscopy, which is an inexpensive and easily transportable analytical technique. Specifically, we show that when the nanoparticles undergo leaching, changes in extinction intensity, peak position, and full width at half maximum (FWHM) of extinction peak can be exploited to trace the change in the size of the nanoparticles with only knowing the initial nanoparticle size. The size- and shape-dependent optical properties of metal nanoparticles such as silver (Ag) and gold (Au) are previously investigated in the literature and extensively used for applications such as biomolecules sensing applications [24,127]. The novel findings of this work are the operando use of LSPR spectroscopy for monitoring the size of metal nanoparticles under reaction conditions, and the prediction of the use of this technique for a wide range of metal nanoparticles such as Ag, Au, Cu, Ni, Pt, Pd, and bi-metallic (e.g., Ag-Pd) nano catalysts.

To demonstrate the use of UV-Vis spectroscopy in the characterization of nanoparticle-catalyzed reactions, we have selected monometallic nanoparticles, such as Pd, Pt, Ni, Rh, Au, and Cu

nanoparticles, and core-shell Ag-Pd nanoparticles. These nanostructures have been shown to be efficient catalysts for a wide range of reactions including hydrogenation and cross-coupling reactions ranging from aryl halides with aryl borates (Suzuki), terminal alkenes (Heck), terminal alkynes (Sonogashira), as well as oxidative homocoupling of terminal alkynes (Glaser) [135–137,139–141,154,159–162,162–180]. In order to predict extinction spectra for varying sizes of Pd, Pt, Ni, Rh, Au, and Cu nanoparticles, and varying shell thicknesses of Ag-Pd core-shell nanoparticles, we utilized FDTD simulations. The representative simulated extinction spectra (i.e., extinction cross section as a function of wavelength) of these nanoparticles are shown in Figures 9a-f. In the simulated extinction spectra, the dominant peak for localized surface plasmon resonance (LSPR) centered at 530, 205, 235, 200, 225 and 570 nm are observed for Au, Ni, Pt, Rh, Pd, and Cu spherical nanoparticles, respectively.

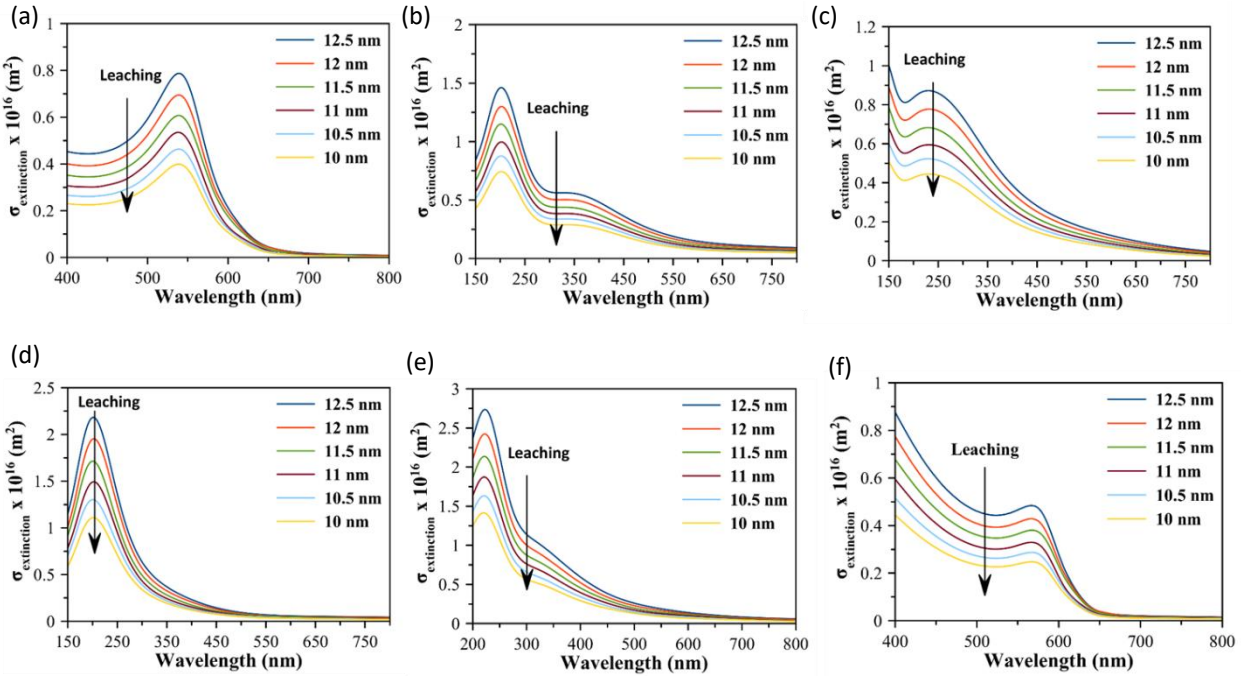

Figure 9. Finite-difference time-domain (FDTD) simulated extinction spectra for **(a)** Au, **(b)** Ni, **(c)** Pt, **(d)** Rh, **(e)** Pd, and **(f)** Cu nanoparticles of various diameters, respectively. The legends show the particle diameter.

To develop a correlation between nanoparticle size and LSPR peak response, we quantified the changes in the values of peak position, peak extinction intensity, and full width at half maximum (FWHM), as a function of the size of the nanoparticle. We have found that extinction intensity at LSPR peak wavelength can be a good descriptor to determine the change in nanostructure size. The representative results in Figure 10a-f, show the size (i.e., diameter) of Au, Ni, Pt, Rh, Pd, and Cu nanoparticles as a function of the percentage change in extinction intensity at the main LSPR peak wavelength, respectively. The corresponding extinction cross section values are also shown (Table 1) in Supporting Information. As seen in Figure 10a, if the diameter of the Au nanosphere is reduced from 12.5 to 12 nm (e.g., due to leaching), there will be approximately 12% decrease in the corresponding extinction intensity at LSPR wavelength of 530 nm. For transition metals, a change of 0.5 nm in diameter can easily account for leaching of approximately one monolayer of surface atoms. Therefore, our FDTD simulation results reveal that the changes in the extinction intensity are detectable for leaching of even a monolayer of atoms from the surface of metal nanoparticles.

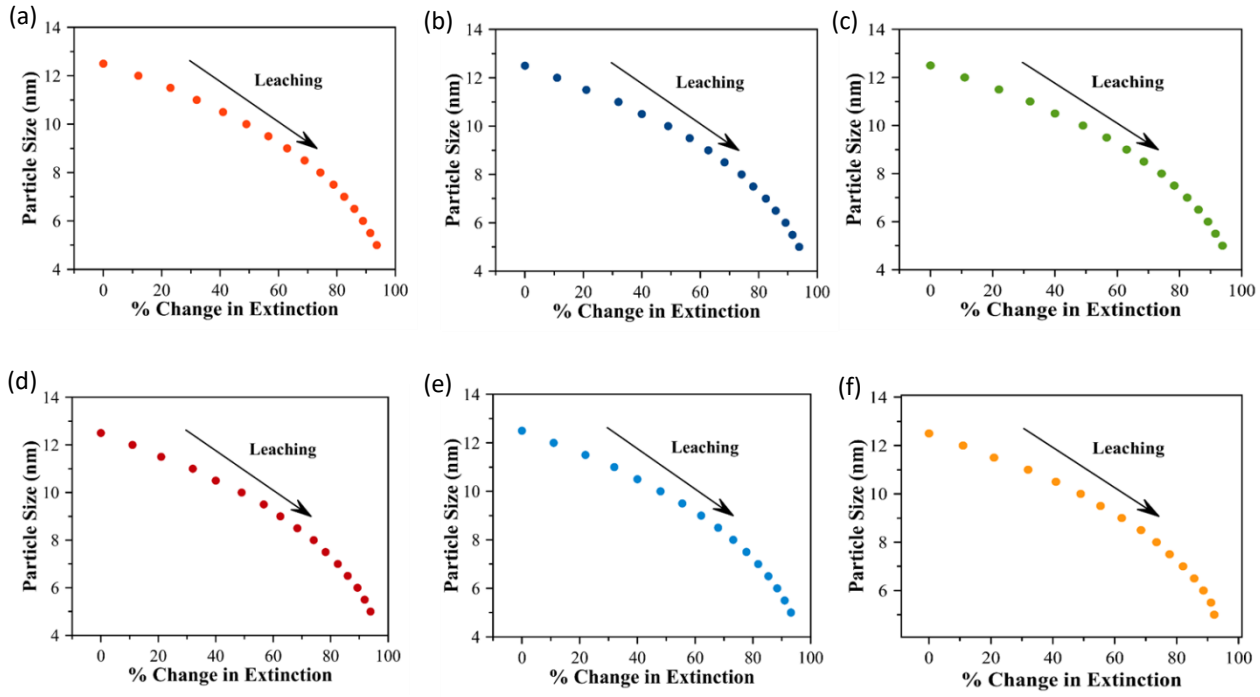

Figure 10. FDTD simulated particle size of nanoparticle as a function of percentage change (i.e., decrease) in extinction intensity at the dominant LSPR peak wavelength for **(a)** Au, **(b)** Ni, **(c)** Pt, **(d)** Rh, **(e)** Pd, and **(f)** Cu nanoparticles, respectively.

For core-shell Ag-Pd nanoparticles, the simulated extinction spectra of Ag nanoparticle of 16 nm core diameter with varying Pd shell thicknesses are shown in Figure 11a. For this system, we found that the extinction intensity, peak position, and FWHM can be adopted as sensitive measures of nanoparticle leaching as shown in Figure 11b-d. Figure 11a shows that the LSPR extinction intensity of Ag nanoparticle of 16 nm diameter is decreased when coated with Pd shell of 1 nm thickness. This decrease in plasmonic intensity is expected due to the damping of LSPR of Ag by the Pd shell. This prediction is in agreement with the experimental results reported in the literature for similar hybrid plasmonic nanocatalysts such as Au-Pd and Cu-Cu_2O nanoparticles [181,182].

As seen from Figures 11c-d, as Pd surface atoms are leached, the LSPR peak redshifts and narrows until the plasmonic Ag core is exposed. For Ag-Pd nanosphere of 16 nm core diameter and 1 nm

shell thickness, as the Pd shell is completely leached into solution, Figure 11b, 11c and 11d show that the extinction intensity, FWHM and peak position change by 82%, 35 nm and 22 nm, respectively. Our simulation results also predict that the changes in FWHM and peak position are 10 nm and 8 nm, respectively, for leaching of a single monolayer of Pd atoms from the nanoparticle surface. The quantification of this change is within the measurement capabilities of spectrophotometers used within research today.

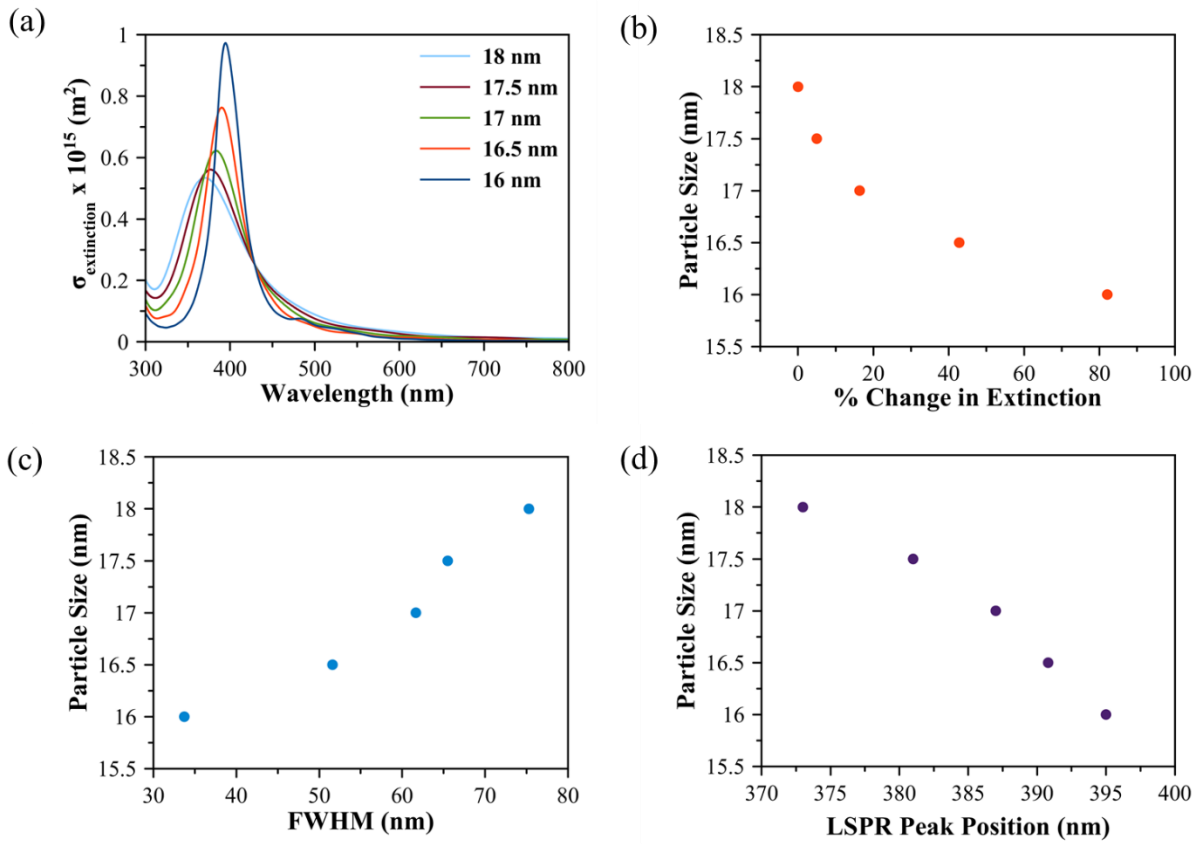

Figure 11. (a) FDTD simulated extinction spectra of core-shell Ag-Pd spherical nanoparticles of various sizes. FDTD simulation predicted particle size as a function of **(b)** percentage change (i.e., increase) in extinction intensity, **(c)** FWHM, and **(d)** peak position of LSPR peak.

The legend in Figure 11.a. show the particle size. For example, the particle size of 18 nm corresponds to Ag-Pd nanosphere of 16 nm core diameter and 1 nm shell thickness.

Our simulation results shown in Figures 9a, predict that operando UV-Vis spectroscopy of metal nanoparticles will not show any major changes in the LSPR responses, i.e., extinction intensity, peak position or FWHM, if the size of nanoparticle is truly stable; whereas for nanoparticles that undergo change in size, there will be change in extinction intensity, FWHM and peak position in the LSPR spectra. To validate the predictions of our simulated results and test the applicability of UV-Vis light extinction spectroscopy, we investigated two different systems. The first system is the growth of spherical gold (Au) nanoparticles using a seeded growth approach. In this approach, we used spherical Au nanoparticles of 8.02 ± 0.59 nm diameter as seed for the growth of larger particles. To allow gradual increase in the size of Au nanoparticles, a known amount of growth solution comprised of Au precursor was added step-by-step to this seed solution. For each addition, operando UV-Vis extinction spectra measurements were made to predict the increase in Au nanoparticle size and the samples were also taken to measure the average size of Au nanoparticles from TEM. Figures 12a and 12b show the representative TEM image of seed particles and Au nanoparticles obtained at the end of the growth process.

Figure 8c shows the operando UV-Vis extinction spectra of Au nanoparticles of 8 nm average diameter in seed solution and for each step-by-step addition during the growth process. The FDTD simulated extinction spectrum of seed Au nanoparticle of 8 nm average diameter is shown in Figure 12d. From the measured operando extinction spectra, the increase in extinction intensity value at LSPR peak wavelength is quantified. Using this value, the FDTD simulation predicted average size of Au nanoparticle that exhibits a similar increase in extinction intensity is then identified. Figure 12d shows the FDTD simulation predicted extinction spectra of the respective Au nanoparticles for each step-by-step addition during the growth process. As seen from Figures 12c and 12d legends,

the TEM-measured average sizes and the sizes predicted from the combination of UV-Vis

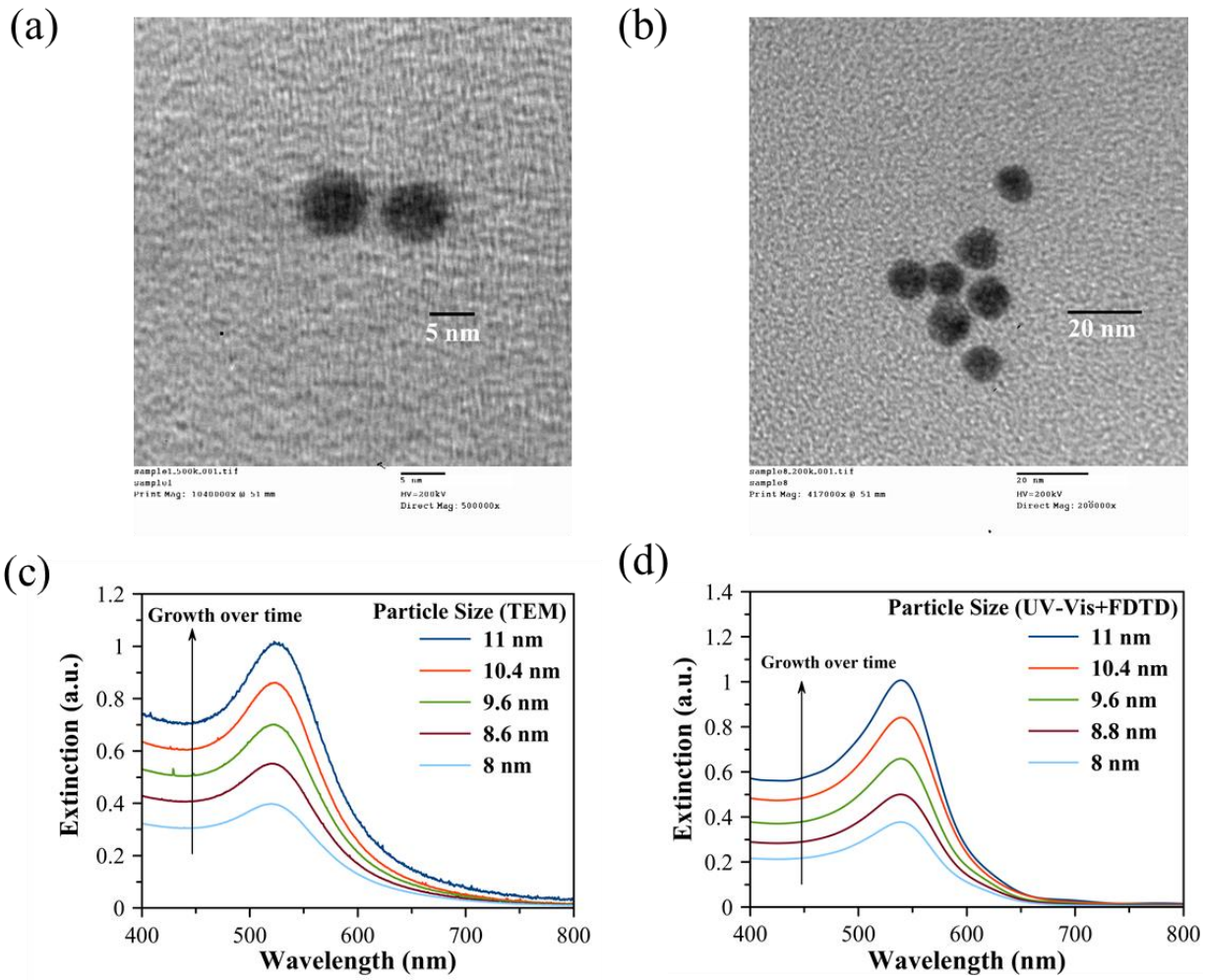

spectroscopy and FDTD simulation match very well.

Figure 12. Representative TEM image for **(a)** seed Au nanoparticles (average diameter = 8.02), and **(b)** Au nanoparticles obtained after the process of growth (average diameter = 11 nm). **(c)** Operando UV-Vis extinction spectra of Au nanoparticles measured during growth process. (**d**) FDTD simulated extinction spectra of Au nanoparticles for the growth process. The legends in Figures 12c and 12d show the particle diameter.

The second system, for which we validated the applicability of the UV-Vis light extinction spectroscopy is the Au nanoparticles-catalyzed C-C coupling reaction. Specifically, the

homocoupling of phenylacetylene was selected as a model reaction. For this system, we used spherical Au nanoparticles as a catalyst to drive the homo-coupling of phenylacetylene (PA). The operando UV-Vis extinction spectra measurements and samples of the reaction mixture for TEM imaging were taken at frequent time intervals. In Figure 13a, we show the operando UV-Vis extinction spectra of the reaction mixture at different reaction times. The dominant extinction peak observed at ~530 nm is due to the LSPR dipole mode of Au nanoparticle. It is worth mentioning that the operando UV-Vis extinction measurements can also be used to capture the LSPR peak of metal nanoparticles when they are supported on inert support such as alumina and silica [19,181].

As seen from Figure 13a, the extinction intensity at LSPR peak wavelength of ~530 nm decreases with increasing reaction time. The decreasing trend in the extinction intensity at ~530 nm in Figure 5a indicates the decrease in the particle size due to the leaching (Arunachalam et al., 2015, 2016). The extinction peak observed at ~490 nm is most likely due to the expected Au complex as a result of leaching. To confirm the catalytic activity of Au nanoparticles, we also analyzed the reaction mixture with GC-MS. The GC-MS analysis of the reaction samples showed that the PA conversion into the homocoupling product, diphenyldiacetylene was 30% after 2 hours of reaction. When the reaction sample was analyzed after 6.5 hours of reaction, 100% PA conversion was observed.

To predict the decrease in the average size of Au nanoparticles from the extinction spectra acquired at different reaction times, the decrease in extinction intensity value at LSPR peak wavelength of ~530 nm is quantified. The average size of Au nanoparticle that exhibits a similar decrease in extinction value is then identified from the FDTD simulations. Figure 13b shows the FDTD simulation predicted extinction spectra of Au nanoparticles for different reaction times during the C-C coupling reaction.

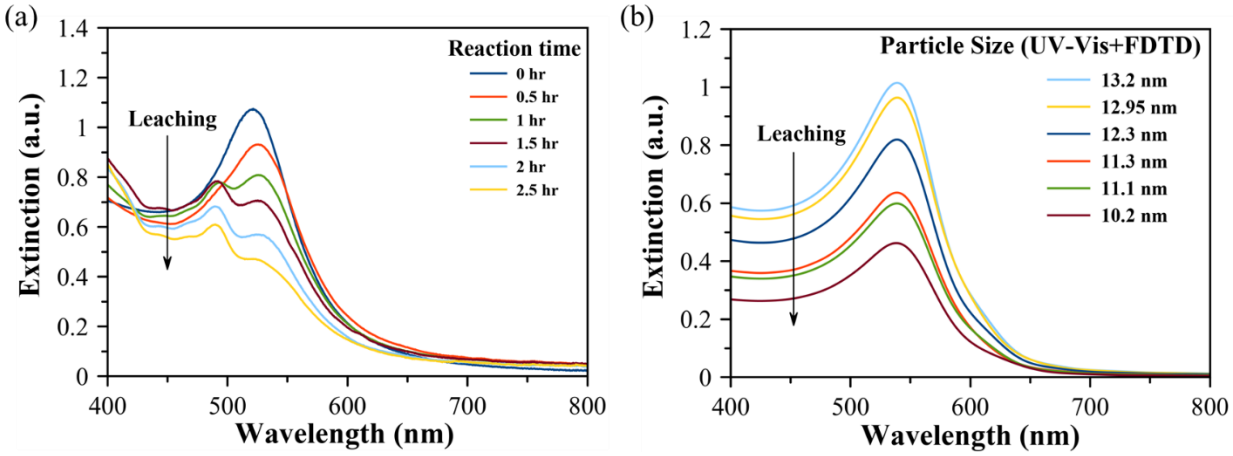

Figure 13. (a) Operando UV-Vis extinction spectra of Au nanoparticles measured during C-C coupling reaction**. (b).** FDTD simulated extinction spectra of Au nanoparticles for the corresponding conditions.

Table 6. Comparison of average sizes measured from TEM and average sizes predicted from the combination of UV-Vis spectroscopy and FDTD simulations.

Predicted Particle Size from UV-Vis + FDTD (nm)	**Measured Particle Size TEM (nm)**
8.85	$\mathbf{8.6 \pm 0.7}$
9.65	$\mathbf{9.56 \pm 0.98}$
10.2	$\mathbf{10.15 \pm 1.14}$
10.4	$\mathbf{10.35 \pm 0.91}$
11	$\mathbf{11.04 \pm 1.3}$
11.1	$\mathbf{11.24 \pm 1.32}$
11.3	$\mathbf{11.34 \pm 0.91}$

To verify the accuracy of nanoparticle size prediction from the combination of UV-Vis spectroscopy and FDTD simulation, in Figure 14, we plotted the parity plot that compares the average sizes measured from TEM and nanoparticle sizes predicted from combination UV-Vis light extinction spectroscopy and FDTD simulation for both growth and leaching processes (Table 6). The parity plot shows a good fit with R^2 value of 0.985. Hence, our results confirm that the combinations of UV-Vis extinction spectra of nanoparticles and FDTD simulation can be used to predict the change in nanoparticle sizes for both growth and leaching processes with only knowing the initial nanoparticle size. The UV-Vis spectroscopy demonstrated in this study can also be applied to trace the size of functioning metal nanocatalysts even when they are supported on support such as alumina, silica or carbonaceous supports [185].

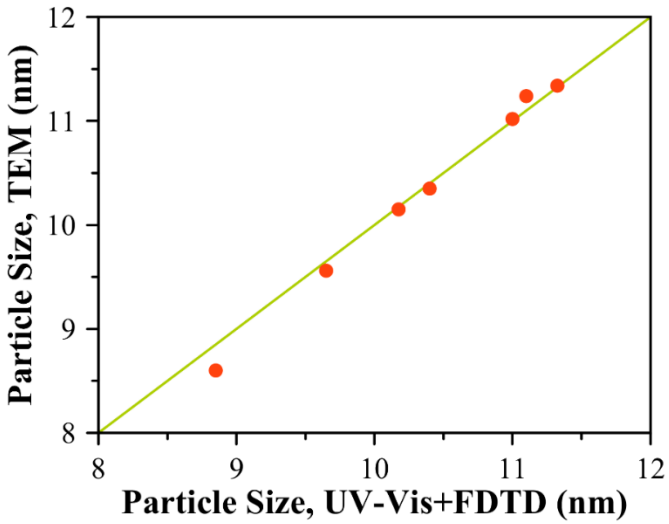

Figure 14. Parity plot showing the average diameters of Au nanoparticles measured from TEM versus Au nanoparticle sizes predicted from combination of UV-Vis spectroscopy and FDTD simulations for both growth and leaching processes.

It is worth mentioning here that this UV-Vis spectroscopy demonstrated in this contribution may not be a sensitive technique that can be used in all situations. The sensitivity of the LSPR technique will depend on the size and concentration ranges. The size ranges investigated in this contribution is less than 18 nm. The decrease in extinction peak intensity is still expected even for larger particle size (e.g., 50 nm). However, the percentage change in the extinction intensity is expected to be relatively smaller, but the technique can still be applied, albeit with a relatively lower sensitivity. Similarly, at a higher concentration range, the aggregation of metal nanoparticles could be a possible issue [36]. There could also be situations where this technique may not be a viable methodology. For instance, there could be situations where the LSPR peak of metal nanoparticles may significantly overlap with the absorption peak of the soluble metal complex, reactant, or product. In such situations, the UV-Vis LSPR extinction measurements alone may not be used as accurate methodology for predicting the size of functioning nano catalysts. The concentration of overlapping species such as reactant or product may need to be additionally quantified using gas chromatography-mass spectrometry (GC-MS) or high-performance liquid chromatography (HPLC). The concentrations quantified from these additional measurements can be used to deconvolute the absorption peak of the overlapping species and the LSPR peak of metal nanoparticles. The deconvoluted LSPR peak can then be possibly used to predict the size of functioning nano catalysts.

Our findings predict that this use of UV-Vis spectroscopy can be used as an in-line process analytical technology (PAT) tool for operando characterization of a variety of monometallic and bimetallic nanoparticle-catalyzed reactions. The operando UV-Vis spectroscopy demonstrated in this study offers a novel tool to use during pharmaceutical development and manufacturing. At an earlier stage of development, for example, during the catalyst screening stage, this technique can be used as an operando spectroscopic tool to quickly screen and identify the nano catalysts that exhibit minimal leaching with similar conversion and impurity profile. At a later stage of process

development, this technique can be used for real-time monitoring of nanocatalyst size in the batch as well as continuous flow packed bed reactors. This valuable data along with the corresponding conversion, impurity profile, and leached metal contents at the reactor outlet stream can be used to develop a robust kinetic model that can contribute to building the process design space in a Quality-by-Design (QbD) framework. Also, during pharmaceutical manufacturing, this in-line PAT tool can be potentially used to take on-the-spot decision-making and/or provide inputs to control systems, for example, to decide when to switch the reactor inlet stream from one packed bed reactor to another reactor to maintain the quality of the reactor outlet stream while avoiding any fluctuation in the production. This sensitive, inexpensive and robust spectroscopic approach can be potentially used as in-line process analytical technology (PAT) in pharmaceutical development and manufacturing. For future works, we suggest other spectroscopic techniques such Raman and FT-IR as in real time In-line PAT techniques to characterize pharmaceutical reagents (Reactants, functioning catalysts, Intermediates, Products).

Finding Optimal Mie Resonant Nano catalysts for Photocatalytic and Photovoltaic Applications

The ability of plasmonic metal nanostructures (PMNs), such as silver and gold nanoparticles, to manipulate and concentrate electromagnetic fields at the nanoscale is the foundation for wide range of applications, including nanoscale optics, solar energy harvesting and photocatalysis. However, there are inherent problems associated with plasmonic metals, such as high Ohmic losses, and poorer compatibility with the conventional complementary metal-oxide-semiconductor (CMOS) microfabrication processes. These limitations inhibit the broader use of PMNs in practical applications. Herein, we report submicron cuprous oxide and cupric oxide particles can exhibit strong electric and magnetic Mie resonances with extinction/scattering cross sections comparable to or slightly exceeding those of Ag particles. Using size- and shape-controlling particle synthesis

techniques, optical spectroscopy, and finite-difference-time-domain simulations, we show that the Mie resonance wavelengths are size- and shape-dependent and tunable in the visible to near-infrared regions. Therefore, submicron copper oxide particles may potentially emerge as high-performance alternatives to PMNs in a wide range of applications.

Plasmonic metal nanostructures (PMNs), such as silver (Ag) and gold (Au) nanoparticles, exhibit extraordinarily high extinction cross sections due to localized surface plasmon resonances (LSPRs).[24,36,40,42,186–193] Since the LSPR wavelength is sensitive to geometry and physical environment, PMNs are very attractive for real-world applications such as sensors,[36,188] nano- and micro-optical devices,[194] photocatalysis[7,13,60,195–198] and photovoltaics.[199–202] Also, the dynamic interplay between plasmonic and metamaterials has demonstrated exceptional properties such as artificial magnetism[203–205] finding applications in subwavelength resonant cavities, sub diffraction near-field super lenses and phase compensators,[206] smart metamaterial cloaking,[207–209] plasmonic color printing and optical data storage.[210]

By virtue of their high extinction cross sections with resonances in the visible and near-IR, PMNs can act as nanoantenna's via electromagnetic (EM) field enhancement effect that has promising applications in third-generation photovoltaics such as dye-sensitized, organic, quantum dot- and perovskite-based solar cells.[199,200] However, these noble metals (Ag and Au) are scarce, expensive, and pose limitations such as intrinsic nonradiative optical losses and fabrication complexities.[208] To overcome this barrier, recent years have witnessed a growing interest in developing novel non-plasmonic and low-loss dielectric resonators that can support light manipulation at the nanoscale and exhibit strong extinction cross sections.[211]

While plasmonic metal[24,36,40,42,186–192] and metal-oxide[212,213] spheres exhibit only electric multipolar resonances (i.e., dipole, quadrupole, etc.), for optically resonant dielectric spheres, both electric- and magnetic multipolar resonances occur.[20,211,214] Similar to the electric multipolar modes in

plasmonic nanoparticles, the electric and magnetic multipolar modes in dielectric structures can lead to enhanced optical responses, such as surface-enhanced absorption, fluorescence and Raman scattering.[211] Therefore, optically-resonant submicron dielectric particles have recently emerged as high-performance alternatives to PMNs. For example, it has been demonstrated that submicron silicon (Si) sphere resonators exhibit lower dissipation losses, strong localization of electromagnetic fields, and superior performance in comparison to their lossy plasmonic silver counterparts.[211,215,216] Also, strong electric and magnetic multipolar resonances have recently been demonstrated in various dielectric nanostructures, such as Si hollow nanocylinders and nanodisks,[217] nanowires,[218–220] silicon carbide microrods,[221] GaAs nanodisks,[222] tellurium cubes,[223] and germanium particles.[224]

Herein, we report strong and tunable non-plasmonic Mie resonances in cuprous oxide (Cu_2O), cupric oxide (CuO), titanium dioxide (TiO_2), cerium dioxide (CeO_2) and Fe_2O_3 particles with sizes of few hundreds of nm. Using finite-difference time-domain (FDTD) simulations, we show that the copper oxide (Cu_2O, CuO, TiO_2, CeO_2, and Fe_2O_3) particles exhibit strong electric as well as magnetic near-field enhancements at the Mie resonances. We show experimentally and numerically that Mie resonances in cuprous oxide (Cu_2O) particles can be tuned from visible to near-infrared (NIR) by varying the particle size and shape. The high scattering cross sections of the Cu_2O particles allow for acquisition of single-particle scattering spectra, which are also observed to vary with particle size and shape.

Figures 15a-b and Figure 16a-d show the simulated extinction, Scattering and adsorption cross section spectra for varying sizes of Cu_2O spheres. In Figure 15a, a Mie resonance peak is seen to red shift with increasing particle size. The peak maximum enters the simulation window of 400-2000 nm for particle size of 125 nm and larger. In Figure 15b, as the particle size increases to 200 nm and above, more than one Mie resonance peaks become noticeable. For the largest spherical particle of 400 nm diameter, three of the resonance peaks are below the bandgap of Cu_2O (i.e.,

wavelength above 590 nm). Cu_2O and CuO are semiconductors with bandgaps of ~2.1 and ~1.2 eV, respectively.[195,225,226]

These resonance features are not expected for the bulk single crystalline Cu_2O.

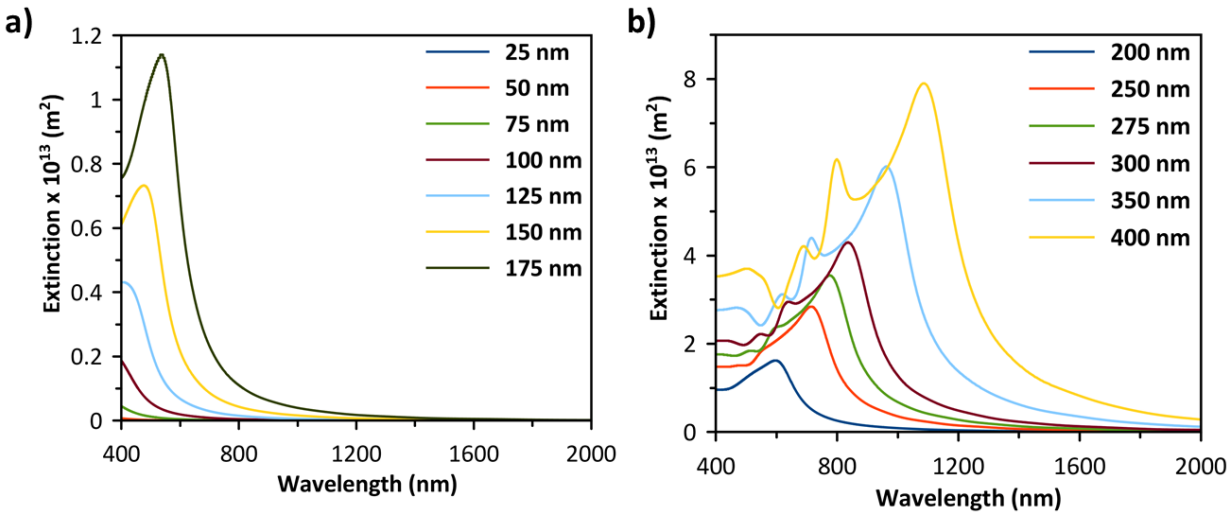

Figure 15. Simulated extinction cross section as a function of wavelength for Cu_2O spheres of various diameters ranging from (a) 25 to 175 nm, and (b) 200 to 400 nm.

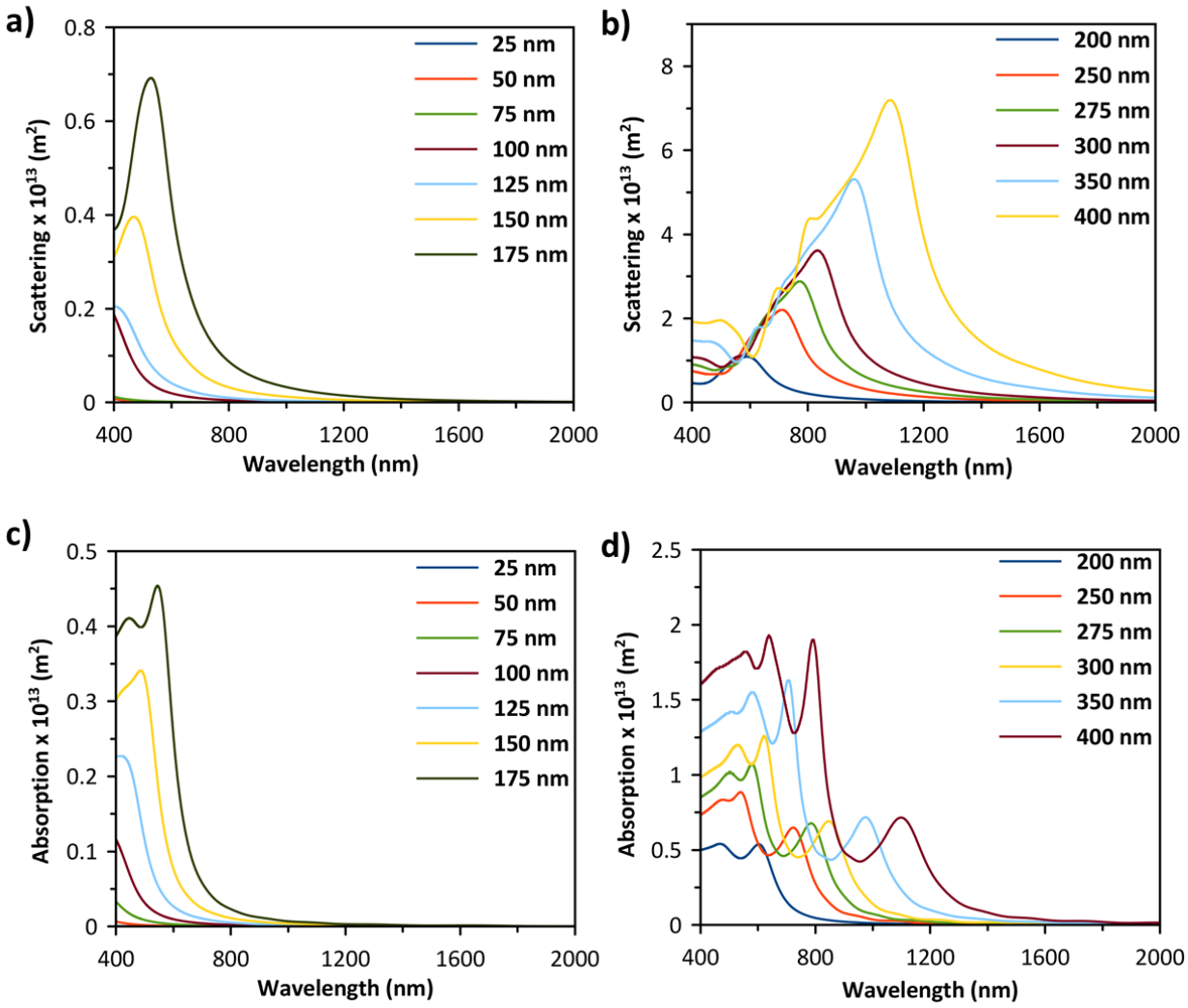

Figure 16. (a and b) Simulated scattering cross section as a function of wavelength for Cu_2O spheres of various diameters ranging from (a) 25 to 175 nm, and (b) 200 to 400 nm. (c and d) Simulated absorption cross section as a function of wavelength for Cu_2O spheres of various diameters ranging from (c) 25 to 175 nm, and (d) 200 to 400 nm.

To explicate Mie resonance peaks observed in the extinction spectra of Cu_2O particles, we first present detailed analysis of the simulation data for the 175 nm spherical particle, as an example. Figure 17a shows the simulated extinction spectrum of the 175 nm diameter Cu_2O sphere. For

comparison, we have also provided the simulated extinction spectrum of a 175 nm diameter Ag sphere in Figure 17b. The Cu_2O particle exhibits one resonance peak, being at 542 nm. In Figures 17c, 17d, 18 and 19 we show the corresponding magnetic and electric field spatial distributions, respectively. For the simulations of the field distributions, a plane wave is used for the incident radiation propagating in the direction of positive x-axis and polarized along the y- and the z-axes for the electric and magnetic fields, respectively.

The electric field distribution in Figure 17d shows the typical two-lobe distribution, characteristic of an electric dipole. Similarly, the magnetic field distribution pattern in Figure 17c confirms the magnetic dipole mode.[215] The enhanced magnetic near field pictured in Figure 17c is generated by the circular displacement currents, strongly coupled to the electric field penetrating into the particle.[211] The optimum current-field overlap/coupling leading to magnetic dipole resonance occurs when electric field is antiparallel at opposite edges of the particle. Hence, the condition for magnetic dipole resonance is that wavelength inside the particle equals approximately the particle dimension along the propagation direction (inside particle),[211] explaining the tunability of the resonance with size.

Figures 17c-d, 18 and 19 show that the 175 nm Cu_2O sphere can exhibit enhancements of up to 25 and 8 times for the near magnetic and electric field intensities, respectively, over the incident far field. The comparison of the magnetic and electric field distributions shown in Figures 17c-d. For comparison, in Figures 17e-f, we also provide the simulated magnetic and electric field distributions for a 175 nm diameter Ag sphere at the LSPR peak wavelength of 530 nm. As seen, the magnetic field enhancement is relatively weak for the Ag particle. Hence, the electric dipolar mode dominates the LSPR at 530 nm. Impressively, the extinction cross section of the Cu_2O sphere is comparable to that of Ag sphere.

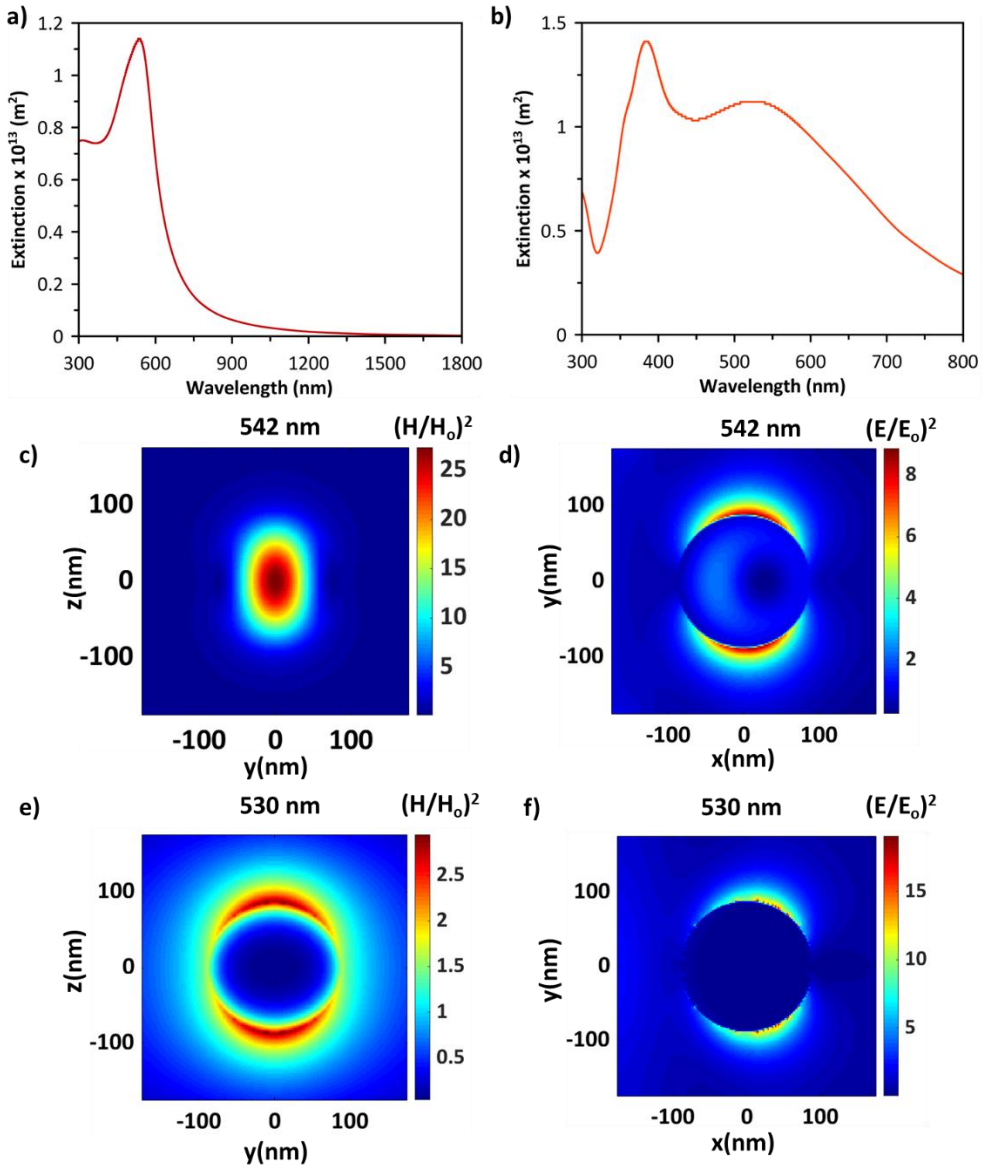

Figure 17. Simulated extinction cross section as a function of wavelength for (a) 175 nm Cu_2O sphere, and (b) 175 nm Ag sphere. Simulated spatial distribution of enhancement in (c) magnetic field intensity $[H^2/H_0^2]$ in YZ plane, and (d) electric field intensity $[E^2/E_0^2]$ in XY plane, for 175 nm Cu_2O sphere at the resonance wavelength of 542 nm. Simulated spatial distribution of

enhancement in (e) magnetic field intensity [H^2/H_0^2] in YZ plane, and (f) electric field intensity [E^2/E_0^2] in XY plane, for 175 nm Ag sphere at the resonance wavelength of 530 nm.

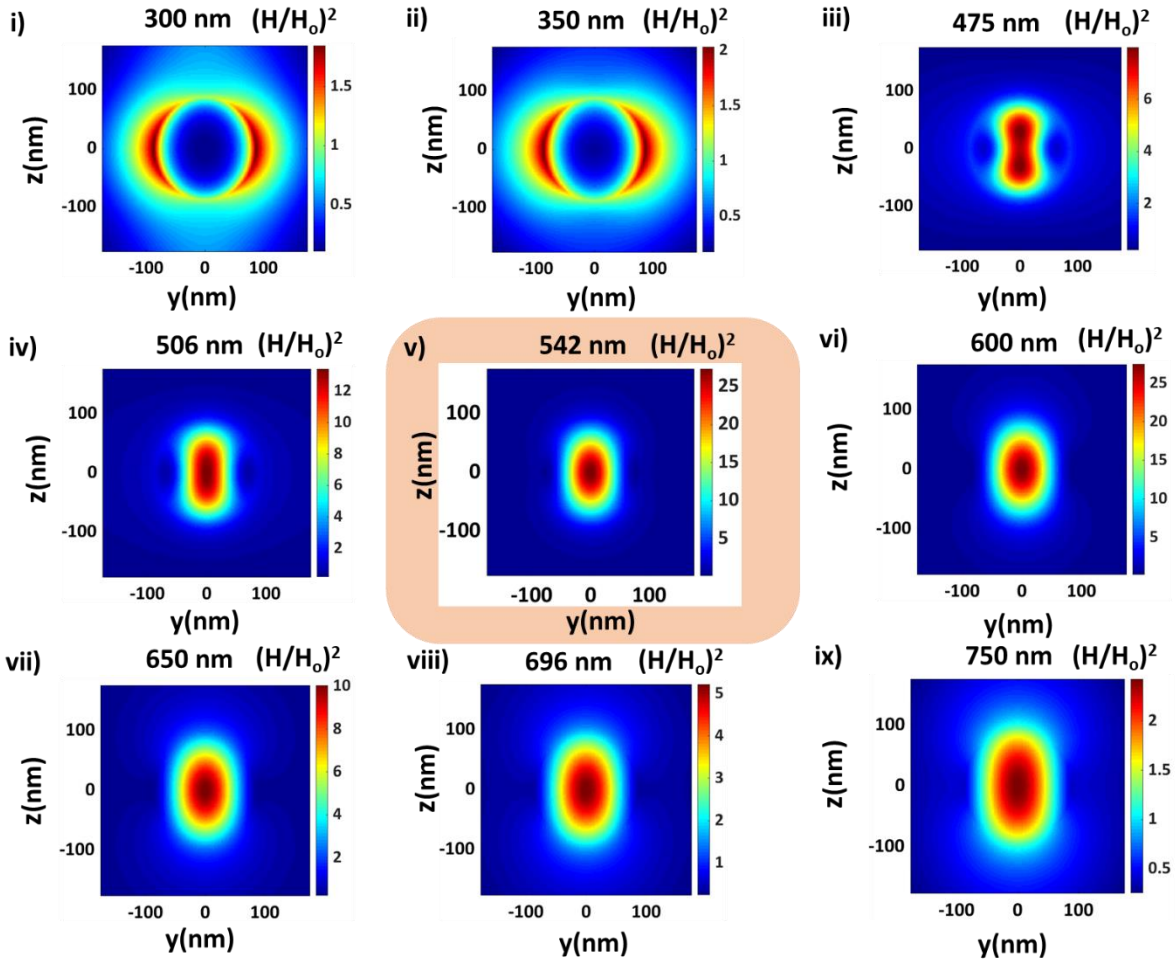

Figure 18. Simulated spatial distribution of enhancement in magnetic field intensity [H^2/H_0^2] in YZ plane at different wavelengths across the Mie resonance peak wavelength (i.e., **542 nm**) for Cu_2O sphere of 175 nm diameter.

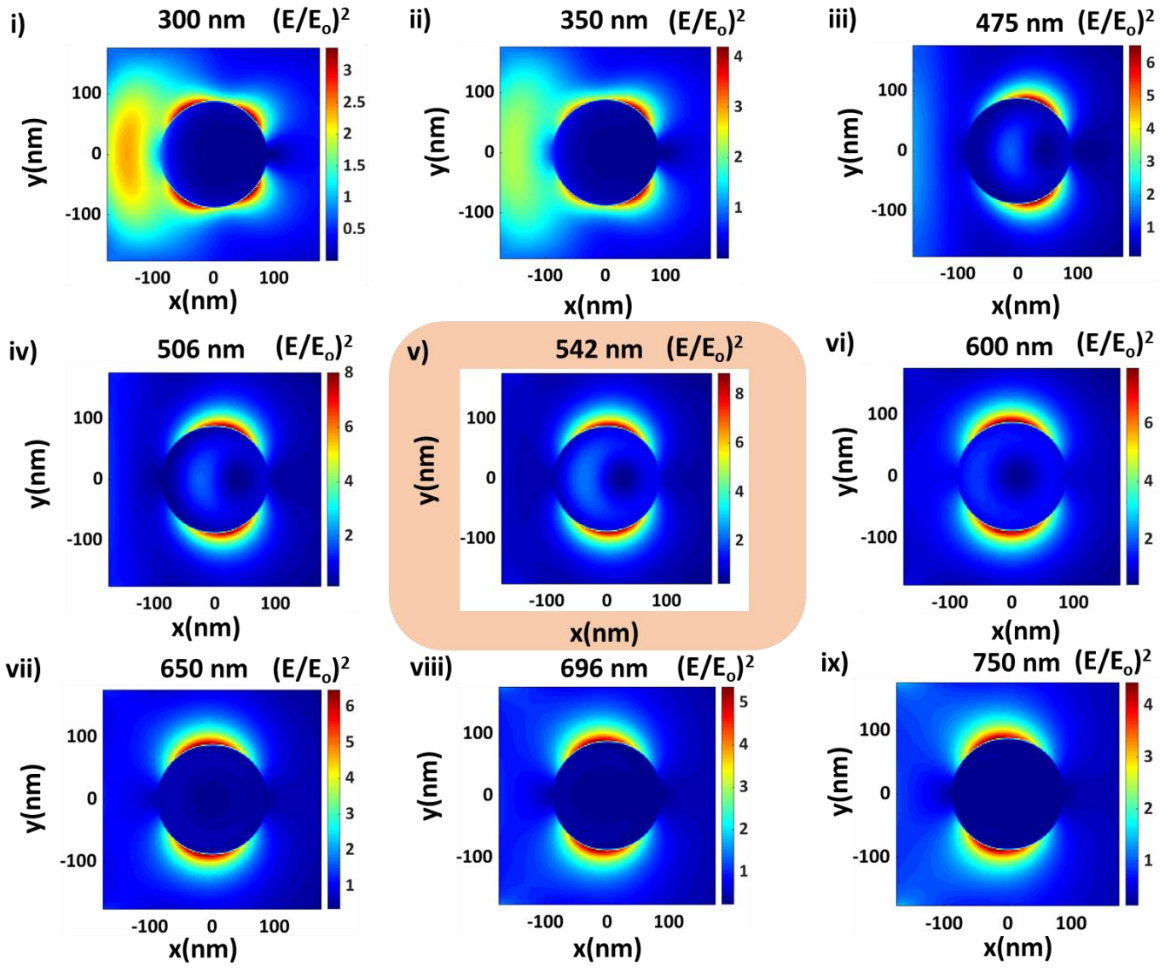

Figure 19. Simulated spatial distribution of enhancement in electric field intensity [E^2/E_0^2] in XY plane at different wavelengths across the Mie resonance peak wavelength (i.e., **542 nm**) for Cu_2O sphere of 175 nm diameter.

Figures 20a shows the UV-Vis-NIR extinction spectra of Cu_2O quasi-sphere samples measured at different times during the synthesis. XRD data analysis as shown in Figure 21 confirms Cu_2O preparation. Figures 20b shows the representative TEM images of the Cu_2O sphere. During the Cu_2O spherical particle synthesis, we monitored the extinction spectrum as a function of synthesis time until 20 h, after which no significant change was observed. Additionally, the TEM indicated

the average particle size increases with synthesis time and saturates beyond 20 h, being consistent with the extinction results.

As seen from Figure 20a, no resonance peaks for smaller Cu_2O spherical particles at the early stage of synthesis (e.g., 1-h sample, particle diameter = 5.3 ± 1.7 nm) can be captured in the measurement range of 300-800 nm. On the other hand, the 8-h sample with a size of 125 ± 28 nm, shows a clear Mie resonance peak at about 450 nm. Based on our FDTD simulation results (e.g., Figure 15a), we assign this resonance peak to the combination of magnetic and electric dipolar modes. Figure 22,23 and Table 7 show size distribution of Cu_2O spherical particles in different time.

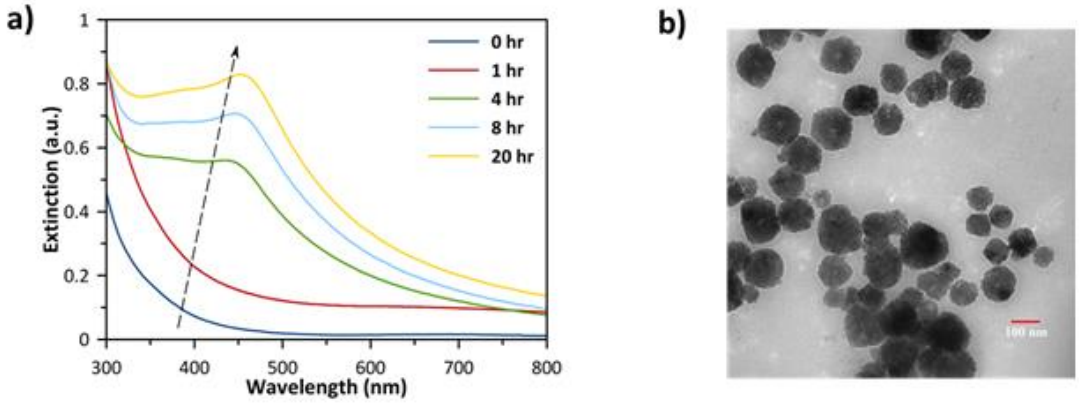

Figure 20. Measured UV-Vis-NIR extinction spectra of Cu_2O spherical particles (a) Representative TEM images of quasi-Cu_2O spheres after 8 h of synthesis (b).

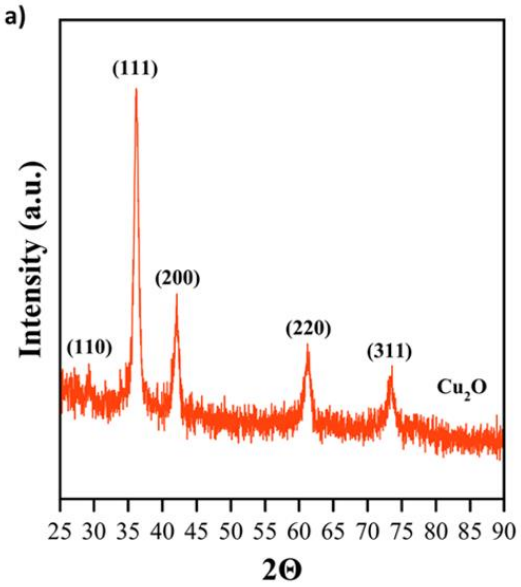

Figure 21. The representative X-ray diffraction pattern of Cu_2O **(a)** quasi-spherical.

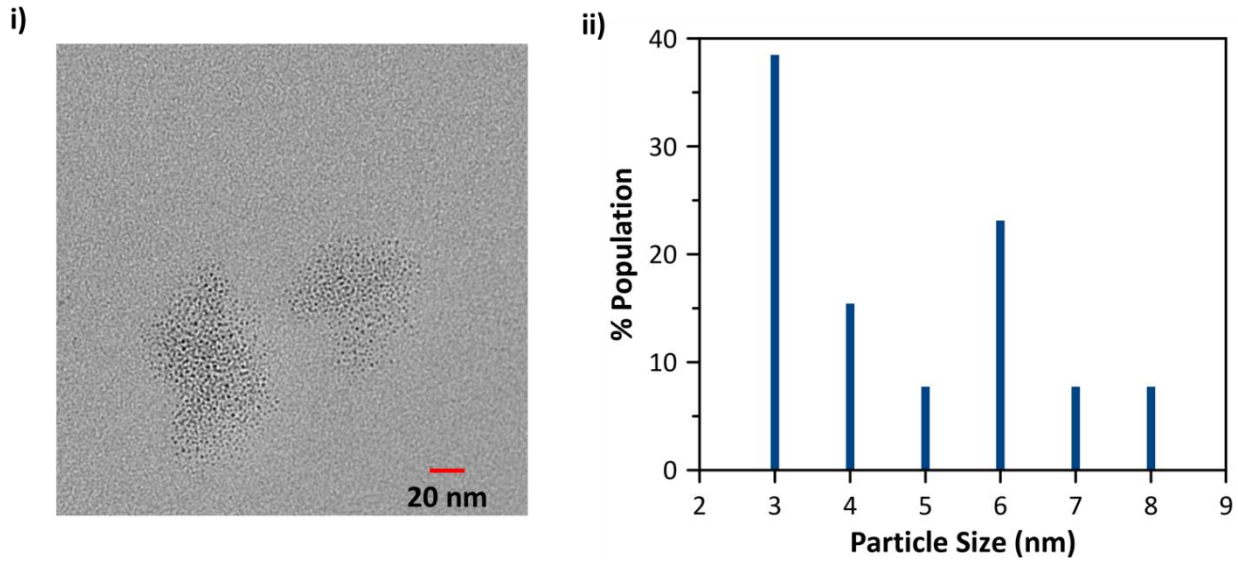

Figure 22. Representative TEM image of particles, and **ii)** size distribution of particles, for the sample collected at 1 hr during the synthesis of Cu_2O spheres. Average size of particles = 5.3 ± 1.7 nm.

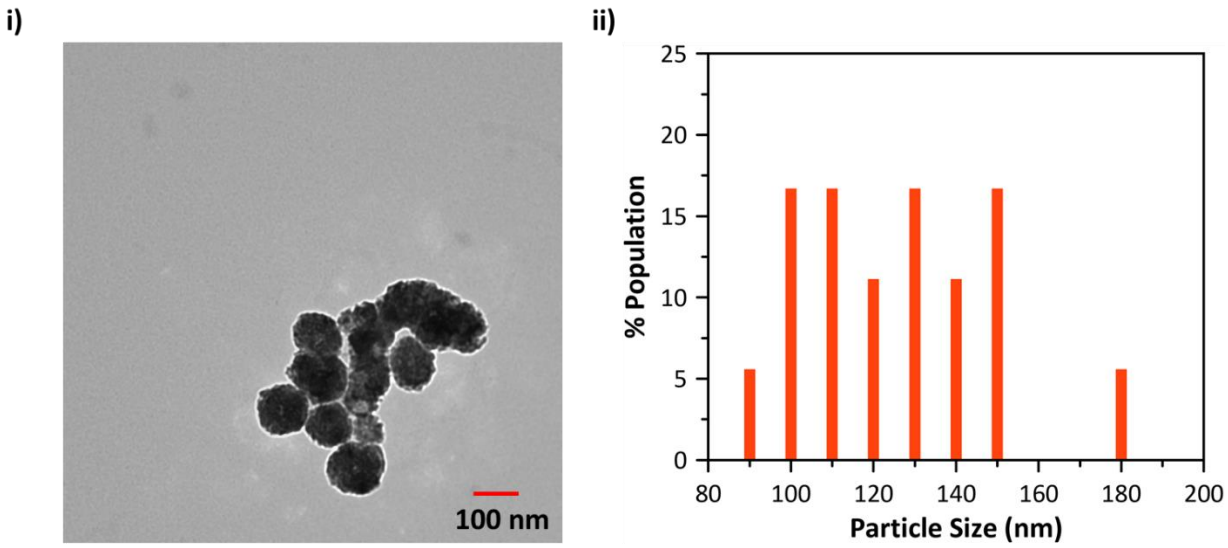

Figure 23. Representative TEM image of particles, and **ii)** size distribution of particles, for the sample collected at 4 hr during the synthesis of Cu_2O spheres. Average size of particles = 120 ± 22 nm.

Table 7. TEM-measured average particle sizes of Cu_2O spheres during growth synthesis at different time intervals.

Time (hr)	**Average size (nm)**
1	5.3 ± 1.7
4	120 ± 22
8	125 ± 28

The optical properties of other dielectric materials such as CuO, TiO_2, CeO_2, and Fe_2O_3 Mie Resonator nanoparticles are investigated using the finite difference time domain (FDTD) simulation. There are not many studies have been reported on the optical properties of these Mie Resonator nanoparticles. We investigated the electronic and magnetic structures (optical properties) of TiO_2, CeO_2 , Fe_2O_3 and CuO in the UV, Visible and near-infrared regions with various sizes and shapes (Figures 24,25,27and 29). By examining the optical properties, we found that the TiO2, CeO_2 , Fe_2O_3 and CuO with different sizes and shapes showed excellent optical properties in the Uv, visible and near-infrared regions. Furthermore, the optical properties of the corresponding materials are characterized by UV–Visible spectrophotometry (Figures 26,28 and 30). The optical properties are varying with size and shape and can be tuned over wide wavelengths range. Our combined analysis, FDTD simulation and Uv-Vis's spectroscopy, allows us to find optimal Mie Resonator nanocatalyst with specific size and shape that exhibits desired Mie resonances in the UV, Visible and near-infrared regions for photocatalytic and photovoltaic applications.

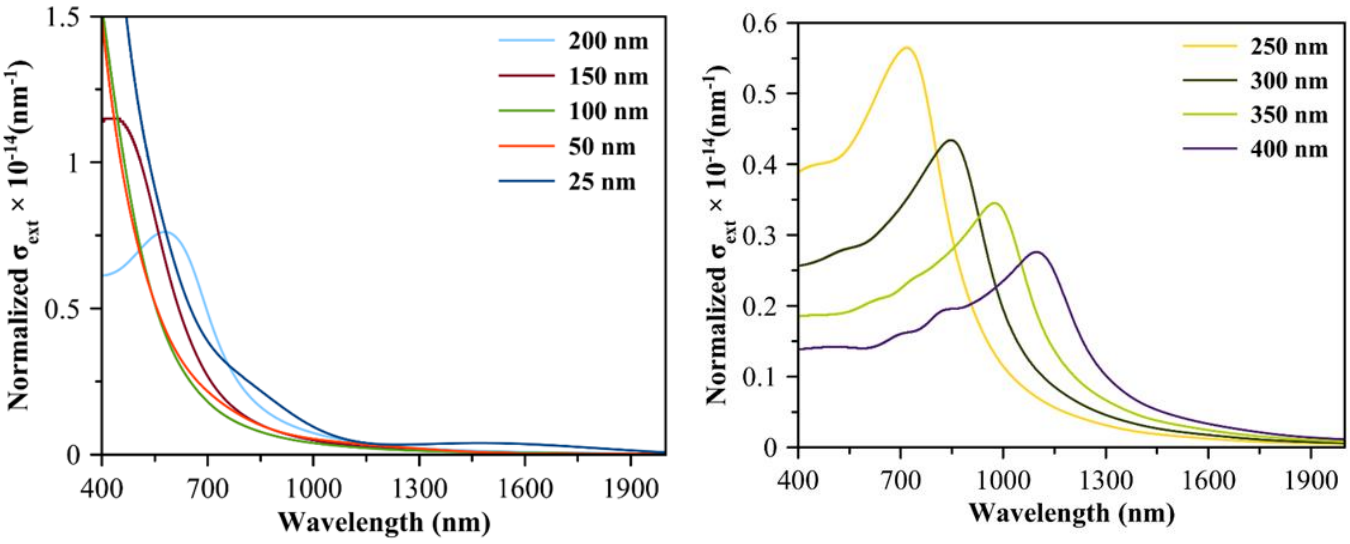

Figure 24. Simulated extinction cross section as a function of wavelength for CuO spheres of various diameters ranging from (a) 25 to 200 nm, and (b) 250 to 400 nm.

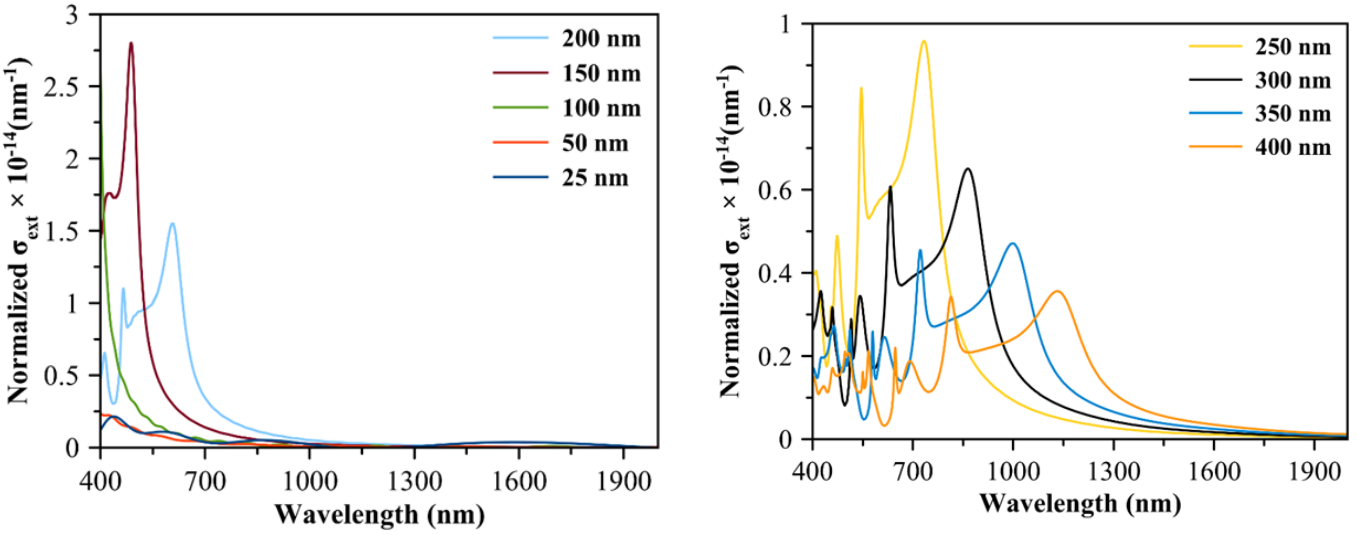

Figure 25. Simulated extinction cross section as a function of wavelength for TiO_2 spheres of various diameters ranging from (a) 25 to 200 nm, and (b) 250 to 400 nm.

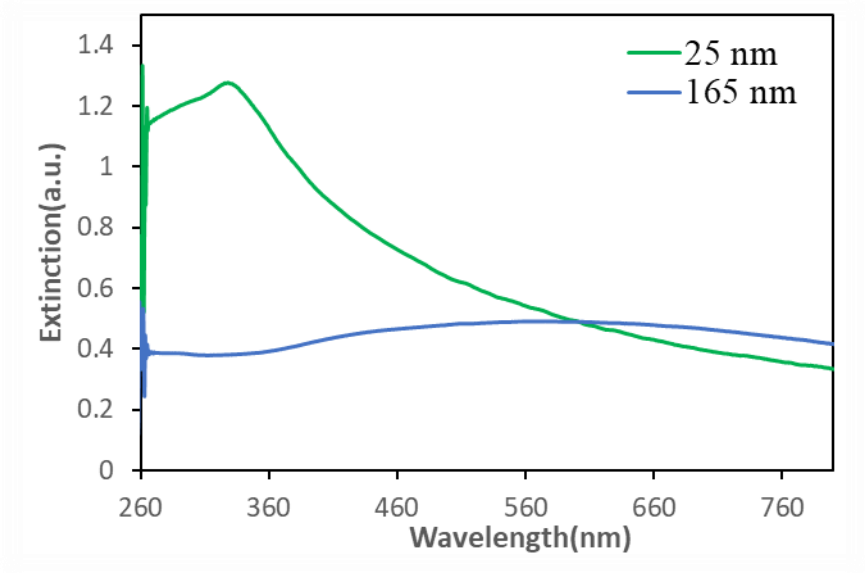

Figure 26. Measured UV-Vis-NIR extinction spectra of TiO_2 spherical particles.

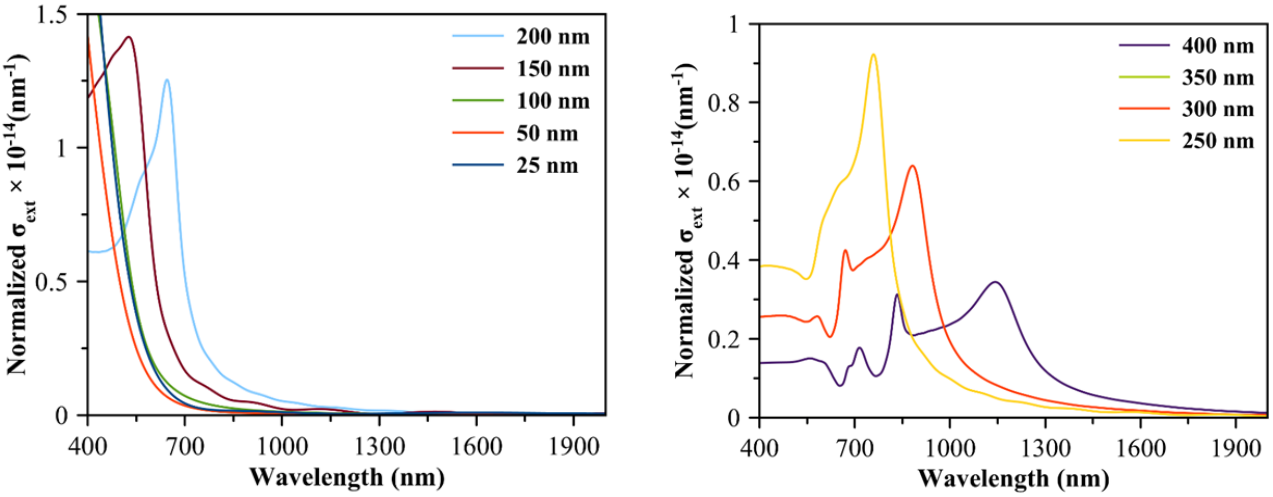

Figure 27. Simulated extinction cross section as a function of wavelength for Fe_2O_3 spheres of various diameters ranging from (a) 25 to 200 nm, and (b) 250 to 400 nm.

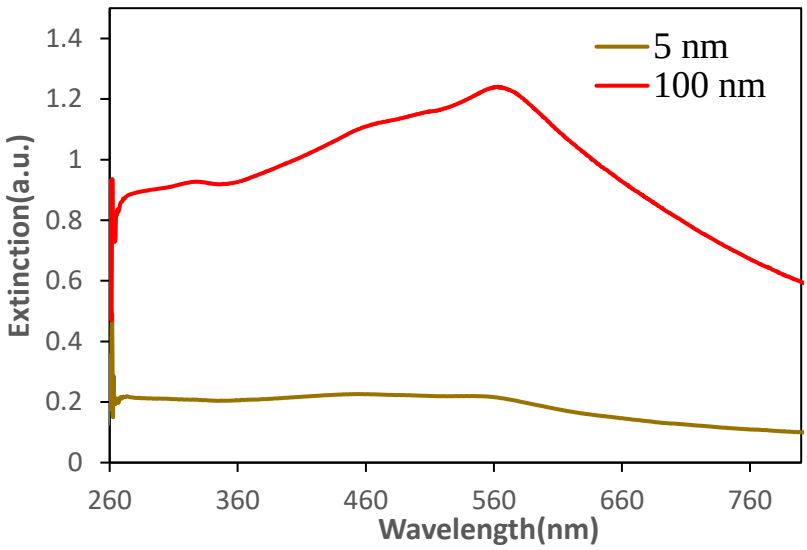

Figure 28. Measured UV-Vis-NIR extinction spectra of Fe_2O_3 spherical particles.

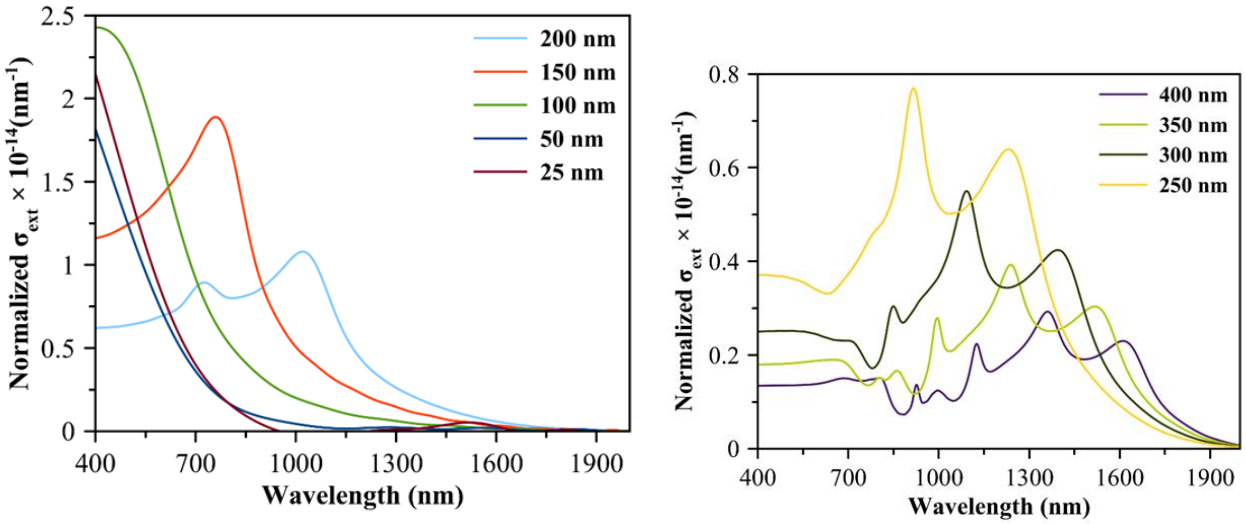

Figure 29. Simulated extinction cross section as a function of wavelength for CeO_2 Spheres of various diameters ranging from (a) 25 to 200 nm, and (b) 250 to 400 nm.

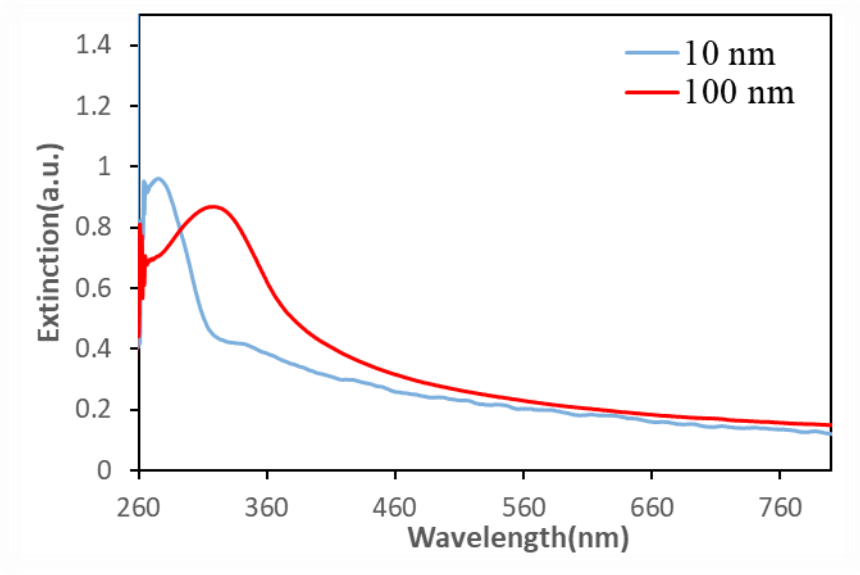

Figure 30. Measured UV-Vis-NIR extinction spectra of CeO_2 spherical particles.

Using size- and shape-controlling particle synthesis techniques, optical spectroscopy, and finite-difference-time-domain simulations, we demonstrated that the Mie Resonance wavelengths in Mie Resonator nano catalysts are size- and shape-dependent and tunable in the visible to near-infrared regions. This work demonstrated strong and tunable Mie resonances in submicron Cu_2O, CuO ,TiO_2, CeO_2, and Fe_2O_3 particles. By the help of FDTD simulations, we associated these resonances with magnetic and electric multipoles, and they were not plasmonic in nature. The lowest-energy Mie resonance observed in the extinction spectrum is assigned to the combination of the magnetic and electric dipole excitations. Similarly, both the magnetic and electric quadrupole excitations contributed to the second-lowest-energy Mie resonance peak observed in the extinction spectrum. The Mie resonance peak wavelengths were tunable from the visible to the near-IR region by controlling the size and shape of the particles. They efficiently concentrated magnetic and electric near fields at Mie resonances. These high-performance and tunable submicron-antenna attributes of the Cu_2O , CuO ,TiO_2, CeO_2, and Fe_2O_3 submicron particles, combined with their low Ohmic losses and being semiconductors, make them attractive alternatives for wide range of applications,

including photocatalysis and photovoltaics. For future investigations, we suggest to test photocatalytic activity of various Mie Resonator nano catalyst to find the optimal Mie Resonator nano catalyst, we believe that optimal Mie Resonator nanocatalyst with specific size and shape will show more photocatalytic activity than others because of high Mie resonance effect at different wavelengths.

.

CHAPTER V

CONCLUSION

Conclusion

Particle size monitoring of functioning nanomaterials can be precisely accomplished via Uv-Vis spectroscopic technique and finite difference time Domaine (FDTD) simulation. With combination of both experimental and simulation studies, tracing particle size is achieved through monitoring localized surface plasmonic resonance (LSPR) of the functioning nanocatalyst. For UV-Vis spectroscopy, a broadband light source (Uv, visible and near IR regions) is used to directly measure single photon absorption and detect the distinctive LSPR response of a particular nanomaterial with specific size and shape. LSPR responses of nano catalysts were collected for various nano catalysts (plasmonic and dielectric nanomaterials) under different reactions and synthesis conditions. The effect of light that resonant with the LSPR peak of the functioning nano catalyst was used to verify the FDTD simulations results. To develop a real time and more precise method for the measuring amount of leaching of functioning nanocatalyst, we invented a new experimental approach and confirmed the effectiveness and accuracy of the approach with a powerful optical computational simulation tool. In the new experimental setup, we placed a stainless optical probe in the reaction solution which is inactive for the reactions we studied, on middle of the three-neck reaction vessel to measure light absorption of nanocatalyst in real time.

In this work, we built fundamental understanding on monitoring size of functional catalysts and the development of a light-based approach to trace the amount of leaching by combining experimental and simulation studies. Our approach can predict the particle size of catalysts and identify the reaction pathways (Homogeneous vs Heterogeneous) for important reactions. We compared the measured particle size of the catalysts with predicted particle size from simulation, both sizes were almost the same.

In the second part of this thesis, In-Situ Uv-Vis spectroscopy as In-line Process Analytical Technology (PAT) was employed for real-time monitoring of the reaction status. For obtaining real-time information on reaction status to control products quality, operando Uv-Vis spectroscopy was demonstrated as highly reliable, accurate, simple and transportable technology. It enables in-process data to be used for assessing the quality of products in batch or continuous manufacturing, it significantly improves the finished product quality. This PAT technique is on-line characterization tool, reaction sample is analyzed without being removed from the process stream with respect to post-analysis (reaction sample is removed and analyzed away from the process stream), it facilitates on spot decision within a very short time frame. The real-time process decision leads to make a product of desirable quality. This operando Uv-vis spectroscopy method has potential application in pharmaceutical and chemical industry for drug and chemical development and manufacturing.

In the last part of this thesis, we developed various synthesis methods to prepare uniform plasmonic and dielectric nanoparticles. Deep knowledge and protocols were established to prepare uniform plasmonic and dielectric nanoparticles. Size and shape control were important in this study since we were targeting optimal size and shape for particular application to enhance the performance which is directly related to size and shape. By providing the size and shape optical properties studies in this section, we can design the right catalysts (particular size and shape) with the desired binding energy that can resonant with light of specific wavelength to generate hot electrons with correct energy to activate the desired intermediate and product. To address challenges in the energy and

chemistry sectors, finding novel materials with the right size and shape for light-harvesting and energy conversion is a crucial and inevitable part. There is great interest in introducing and developing new methods to search for catalysts and materials with optimal or desired optical properties. Our approach can be used as a direct method where a library of promising advanced nanomaterials with various sizes and shapes through powerful optical computational tools like FDTD and COMSOL can be generated and then experimentally can be screened through size and shape-dependent studies to identify materials with suitable optical properties for a particular application. Optical computational screening of different plasmonic and dielectric materials with various sizes and shapes, followed by synthesizing and testing identified materials will be the promising strategy toward addressing those challenges. Furthermore, this new framework can be an important step toward establishing a reliable method to design novel materials and catalysts that account for high performance and using that method to guide the synthesis of new materials capable of energy capture and catalysis. The finding from these experiments and simulations will guide us to design and prepare targeted catalyst candidates that can enhance the performance of catalytic reactions as a general approach in catalysis, more specifically for photocatalysis and photovoltaic applications. We aimed to significantly enhance the applicability of plasmonic and dielectric nanomaterials for photocatalysis and solar energy conversion by controlling size and shape.

Future Works

In real time reaction monitoring via either Raman scattering or IR absorption technique.

Although there are some advantages and disadvantages for both Raman and IR spectroscopy, almost all most molecules and nano catalysts typically possess both Raman and IR-active transitions of different strength, making both approaches equally viable. The vibrational spectrum of catalysts, products, intermediates and reactants can be collected in real time under different applied reaction condition to obtain valuable information and, to monitor the reaction status. All of the collected spectra can be carefully analyzed to determine optimal catalyst and reaction condition to improve the selectivity of the reaction toward the desired products. Furthermore, these studies

will reveal detailed mechanism in the reaction and provide us more understanding on how to control the reaction paths using spectroscopic techniques. In operando spectroscopic techniques such as Raman and IR are important to gain control over products quality and distribution.

Monitoring particle size of bimetallic oxides and bimetallic nano catalysts

Our approach can be applied to bimetallic nanostructures. Bimetallic nano catalysts are among the most promising catalysts for various applications. Single-particle studies of this work can be used as a foundation for investigation of bimetallic nanoparticles. It is certainly possible, for computational and experimental groups to provide simulation results that is in agreement with an experimental result to predict precisely particle size of functioning bimetallic nanostructure. It requires more complex simulation and experimental analysis since bimetallic structure is mor sophisticated than single particle. Furthermore, Spectroscopic data in conjunction with optical simulation data will allow for the tailored design of bimetallic nanostructures. This capability can be used to prepare the bimetallic catalyst with the right size and shape in order to match the LSPR peak with the desired hot carrier energy as predicted by theory for photocatalysis and photovoltaic applications.

REFERENCES

(1) Well-defined Metal Nanostructures as Platform for Chemical Characterization and Catalytic Applications. https://deepblue.lib.umich.edu/handle/2027.42/100007 (accessed 2020 -04 -01).

(2) Marimuthu, A.; Zhang, J.; Linic, S. Tuning Selectivity in Propylene Epoxidation by Plasmon Mediated Photo-Switching of Cu Oxidation State. *Science* **2013**, *339* (6127), 1590–1593. https://doi.org/10.1126/science.1231631.

(3) Vaughan, O. P. H.; Kyriakou, G.; Macleod, N.; Tikhov, M.; Lambert, R. M. Copper as a Selective Catalyst for the Epoxidation of Propene. *Journal of Catalysis* **2005**, *236* (2), 401–404. https://doi.org/10.1016/j.jcat.2005.10.019.

(4) Beaumont, S. K. Heterogeneously Catalyzing C–C Coupling Reactions with Precious Metal Nanoparticles. *Journal of Chemical Technology & Biotechnology* **2012**, *87* (5), 595–600. https://doi.org/10.1002/jctb.3748.

(5) Zaniewski, A. M.; Schriver, M.; Gloria Lee, J.; Crommie, M. F.; Zettl, A. Electronic and Optical Properties of Metal-Nanoparticle Filled Graphene Sandwiches. *Appl. Phys. Lett.* **2013**, *102* (2), 023108. https://doi.org/10.1063/1.4772542.

(6) Mulvaney, P. Surface Plasmon Spectroscopy of Nanosized Metal Particles. *Langmuir* **1996**, *12* (3), 788–800. https://doi.org/10.1021/la9502711.

(7) Linic, S.; Christopher, P.; Ingram, D. B. Plasmonic-Metal Nanostructures for Efficient Conversion of Solar to Chemical Energy. *Nat Mater* **2011**, *10* (12), 911–921. https://doi.org/10.1038/nmat3151.

(8) Nanocatalysis: Synthesis and Applications | Wiley https://www.wiley.com/en-us/Nanocatalysis%3A+Synthesis+and+Applications-p-9781118148860 (accessed 2020 -04 -01).

(9) Walters, G.; Parkin, I. P. The Incorporation of Noble Metal Nanoparticles into Host Matrix Thin Films: Synthesis, Characterisation and Applications. *J. Mater. Chem.* **2009**, *19* (5), 574–590. https://doi.org/10.1039/B809646E.

(10) Barui, A. K.; Das, S.; Patra, C. R. 10 - Biomedical Applications of Green-Synthesized Metal Nanoparticles Using Polysaccharides. In *Functional Polysaccharides for Biomedical Applications*; Maiti, S., Jana, S., Eds.; Woodhead Publishing, 2019; pp 329–355. https://doi.org/10.1016/B978-0-08-102555-0.00010-8.

(11) Song, H. M.; Moosa, B. A.; Khashab, N. M. Water-Dispersable Hybrid Au–Pd Nanoparticles as Catalysts in Ethanol Oxidation, Aqueous Phase Suzuki–Miyaura and Heck Reactions. *J. Mater. Chem.* **2012**, *22* (31), 15953–15959. https://doi.org/10.1039/C2JM32702C.

(12) Fihri, A.; Bouhrara, M.; Nekoueishahraki, B.; Basset, J.-M.; Polshettiwar, V. Nanocatalysts for Suzuki Cross-Coupling Reactions. *Chem Soc Rev* **2011**, *40* (10), 5181–5203. https://doi.org/10.1039/c1cs15079k.

(13) Kamat, P. V. Photophysical, Photochemical and Photocatalytic Aspects of Metal Nanoparticles. *J. Phys. Chem. B* **2002**, *106* (32), 7729–7744. https://doi.org/10.1021/jp0209289.

(14) Fujishima, A.; Honda, K. Electrochemical Photolysis of Water at a Semiconductor Electrode. *Nature* **1972**, *238* (5358), 37–38. https://doi.org/10.1038/238037a0.

(15) Reiche, H.; Bard, A. J. Heterogeneous Photosynthetic Production of Amino Acids from Methane-Ammonia-Water at Platinum/Titanium Dioxide. Implications in Chemical

Evolution. *J. Am. Chem. Soc.* **1979**, *101* (11), 3127–3128. https://doi.org/10.1021/ja00505a054.
(16) Cheng, G.; Wei, Y.; Xiong, J.; Gan, Y.; Zhu, J.; Xu, F. Same Titanium Glycolate Precursor but Different Products: Successful Synthesis of Twinned Anatase TiO2 Nanocrystals with Excellent Solar Photocatalytic Hydrogen Evolution Capability. *Inorg. Chem. Front.* **2017**, *4* (8), 1319–1329. https://doi.org/10.1039/C7QI00278E.
(17) Pan, J.; Song, C.; Wang, X.; Yuan, X.; Fang, Y.; Guo, C.; Zhao, W.; Huang, F. Intermediate Bands of MoS2 Enabled by Co Doping for Enhanced Hydrogen Evolution. *Inorg. Chem. Front.* **2017**, *4* (11), 1895–1899. https://doi.org/10.1039/C7QI00432J.
(18) Linic, S.; Aslam, U.; Boerigter, C.; Morabito, M. Photochemical Transformations on Plasmonic Metal Nanoparticles. *Nat Mater* **2015**, *14* (6), 567–576. https://doi.org/10.1038/nmat4281.
(19) Linic, S.; Christopher, P.; Xin, H.; Marimuthu, A. Catalytic and Photocatalytic Transformations on Metal Nanoparticles with Targeted Geometric and Plasmonic Properties. *Accounts of Chemical Research* **2013**, *46* (8), 1890–1899. https://doi.org/10.1021/ar3002393.
(20) Kruk, S.; Kivshar, Y. Functional Meta-Optics and Nanophotonics Govern by Mie Resonances. *arXiv:1710.08595 [physics]* **2017**.
(21) Shamshirgaran, S. R.; Khalaji Assadi, M.; Viswanatha Sharma, K. Application of Nanomaterials in Solar Thermal Energy Storage. *Heat Mass Transfer* **2018**, *54* (6), 1555–1577. https://doi.org/10.1007/s00231-017-2259-1.
(22) Ahmed, S. F.; Khalid, M.; Rashmi, W.; Chan, A.; Shahbaz, K. Recent Progress in Solar Thermal Energy Storage Using Nanomaterials. *Renewable and Sustainable Energy Reviews* **2017**, *67*, 450–460. https://doi.org/10.1016/j.rser.2016.09.034.
(23) Khan, H. A.; Sakharkar, M. K.; Nayak, A.; Kishore, U.; Khan, A. 14 - Nanoparticles for Biomedical Applications: An Overview. In *Nanobiomaterials*; Narayan, R., Ed.; Woodhead Publishing, 2018; pp 357–384. https://doi.org/10.1016/B978-0-08-100716-7.00014-3.
(24) Kelly, K. L.; Coronado, E.; Zhao, L. L.; Schatz, G. C. The Optical Properties of Metal Nanoparticles: The Influence of Size, Shape, and Dielectric Environment. *J. Phys. Chem. B* **2003**, *107* (3), 668–677. https://doi.org/10.1021/jp026731y.
(25) Ghaffari, M.; Dolatabadi, J. E. N. Chapter 17 - Nanotechnology for Pharmaceuticals. In *Industrial Applications of Nanomaterials*; Thomas, S., Grohens, Y., Pottathara, Y. B., Eds.; Micro and Nano Technologies; Elsevier, 2019; pp 475–502. https://doi.org/10.1016/B978-0-12-815749-7.00017-7.
(26) Bao, Y.; Wen, T.; Samia, A. C. S.; Khandhar, A.; Krishnan, K. M. Magnetic Nanoparticles: Material Engineering and Emerging Applications in Lithography and Biomedicine. *J Mater Sci* **2016**, *51* (1), 513–553. https://doi.org/10.1007/s10853-015-9324-2.
(27) Holzinger, M.; Le Goff, A.; Cosnier, S. Nanomaterials for Biosensing Applications: A Review. *Frontiers in Chemistry* **2014**, *2*, 63. https://doi.org/10.3389/fchem.2014.00063.
(28) Kanne, T.; Marnauza, M.; Olsteins, D.; Carrad, D. J.; Sestoft, J. E.; de Bruijckere, J.; Zeng, L.; Johnson, E.; Olsson, E.; Grove-Rasmussen, K.; Nygård, J. Epitaxial Pb on InAs Nanowires for Quantum Devices. *Nat. Nanotechnol.* **2021**, *16* (7), 776–781. https://doi.org/10.1038/s41565-021-00900-9.
(29) Singh, H.; Sharma, A.; Bhardwaj, S. K.; Arya, S. K.; Bhardwaj, N.; Khatri, M. Recent Advances in the Applications of Nano-Agrochemicals for Sustainable Agricultural Development. *Environ. Sci.: Processes Impacts* **2021**, *23* (2), 213–239. https://doi.org/10.1039/D0EM00404A.
(30) Engineering precision nanoparticles for drug delivery | Nature Reviews Drug Discovery https://www.nature.com/articles/s41573-020-0090-8 (accessed 2021 -11 -06).
(31) Millstone, J. E.; Kavulak, D. F. J.; Woo, C. H.; Holcombe, T. W.; Westling, E. J.; Briseno, A. L.; Toney, M. F.; Fréchet, J. M. J. Synthesis, Properties, and Electronic Applications of

Size-Controlled Poly(3-Hexylthiophene) Nanoparticles. *Langmuir* **2010**, *26* (16), 13056–13061. https://doi.org/10.1021/la1022938.

(32) Wang, L.; Hasanzadeh Kafshgari, M.; Meunier, M. Optical Properties and Applications of Plasmonic-Metal Nanoparticles. *Advanced Functional Materials* **2020**, *30* (51), 2005400. https://doi.org/10.1002/adfm.202005400.

(33) Sotiriou, G. A. Biomedical Applications of Multifunctional Plasmonic Nanoparticles. *WIREs Nanomedicine and Nanobiotechnology* **2013**, *5* (1), 19–30. https://doi.org/10.1002/wnan.1190.

(34) Ibarra, M. R.; Khlebtsov, N. G. Magnetic and Plasmonic Nanoparticles for Biomedical Devices. *Journal of Applied Physics* **2019**, *126* (17), 170401. https://doi.org/10.1063/1.5130560.

(35) Dionne, J. A.; Baldi, A.; Baum, B.; Ho, C.-S.; Janković, V.; Naik, G. V.; Narayan, T.; Scholl, J. A.; Zhao, Y. Localized Fields, Global Impact: Industrial Applications of Resonant Plasmonic Materials. *MRS Bulletin* **2015**, *40* (12), 1138–1145. https://doi.org/10.1557/mrs.2015.233.

(36) Marimuthu, A.; Christopher, P.; Linic, S. Design of Plasmonic Platforms for Selective Molecular Sensing Based on Surface-Enhanced Raman Spectroscopy. *J. Phys. Chem. C* **2012**, *116* (17), 9824–9829. https://doi.org/10.1021/jp301443y.

(37) Wang, P.; Huang, B.; Dai, Y.; Whangbo, M.-H. Plasmonic Photocatalysts: Harvesting Visible Light with Noble Metal Nanoparticles. *Phys. Chem. Chem. Phys.* **2012**, *14* (28), 9813–9825. https://doi.org/10.1039/C2CP40823F.

(38) Ammari, H.; Romero, F.; Ruiz, M. Heat Generation with Plasmonic Nanoparticles. *Multiscale Model. Simul.* **2018**, *16* (1), 356–384. https://doi.org/10.1137/17M1125893.

(39) Yu, H.; Peng, Y.; Yang, Y.; Li, Z.-Y. Plasmon-Enhanced Light–Matter Interactions and Applications. *npj Comput Mater* **2019**, *5* (1), 1–14. https://doi.org/10.1038/s41524-019-0184-1.

(40) Wiley, B.; Sun, Y.; Mayers, B.; Xia, Y. Shape-Controlled Synthesis of Metal Nanostructures: The Case of Silver. *Chem. Eur. J.* **2005**, *11* (2), 454–463. https://doi.org/10.1002/chem.200400927.

(41) Understanding the Biosynthesis and Catalytic Activity of Pd, Pt, and Ag Nanoparticles in Hydrogenation and Suzuki Coupling Reactions at the Nano–Bio Interface - The Journal of Physical Chemistry C (ACS Publications) https://pubs.acs.org/doi/10.1021/jp508211t (accessed 2019 -02 -13).

(42) Xia, Y.; Halas, N. J. Shape-Controlled Synthesis and Surface Plasmonic Properties of Metallic Nanostructures. *MRS Bulletin* **2005**, *30* (5), 338–348. https://doi.org/10.1557/mrs2005.96.

(43) Chang, H.; Rho, W.-Y.; Son, B. S.; Kim, J.; Lee, S. H.; Jeong, D. H.; Jun, B.-H. Plasmonic Nanoparticles: Basics to Applications (I). In *Nanotechnology for Bioapplications*; Jun, B.-H., Ed.; Advances in Experimental Medicine and Biology; Springer: Singapore, 2021; pp 133–159. https://doi.org/10.1007/978-981-33-6158-4_6.

(44) Krajczewski, J.; Ambroziak, R.; Kudelski, A. Photo-Assembly of Plasmonic Nanoparticles: Methods and Applications. *RSC Adv.* **2021**, *11* (5), 2575–2595. https://doi.org/10.1039/D0RA09337H.

(45) Optimization of silver nanoparticle synthesis by chemical reduction and evaluation of its antimicrobial and toxic activity | Biomaterials Research | Full Text https://biomaterialsres.biomedcentral.com/articles/10.1186/s40824-019-0173-y (accessed 2021 -11 -06).

(46) Tadimety, A.; Wu, Z.; Molinski, J. H.; Beckerman, R.; Jin, C.; Zhang, L.; Palinski, T. J.; Zhang, J. X. J. Rational Design of On-Chip Gold Plasmonic Nanoparticles towards CtDNA Screening. *Sci Rep* **2021**, *11* (1), 14185. https://doi.org/10.1038/s41598-021-93207-7.

(47) Tan, K. H.; Tajuddin, H. A.; Johan, M. R. Feasibility Study on the Use of the Seeding Growth Technique in Producing a Highly Stable Gold Nanoparticle Colloidal System. *Journal of Nanomaterials* **2015**, *2015*, e537125. https://doi.org/10.1155/2015/537125.
(48) Jana, N. R.; Gearheart, L.; Murphy, C. J. Seeding Growth for Size Control of 5−40 Nm Diameter Gold Nanoparticles. *Langmuir* **2001**, *17* (22), 6782–6786. https://doi.org/10.1021/la0104323.
(49) Kyriakou, G.; Beaumont, S. K.; Humphrey, S. M.; Antonetti, C.; Lambert, R. M. Sonogashira Coupling Catalyzed by Gold Nanoparticles: Does Homogeneous or Heterogeneous Catalysis Dominate? *ChemCatChem* **2010**, *2* (11), 1444–1449. https://doi.org/10.1002/cctc.201000154.
(50) Fu, Z.; Zhang, X.; Zhang, H.; Li, Y.; Zhou, H.; Zhang, Y. On the Understandings of Dielectric Constant and Its Impacts on the Photovoltaic Efficiency in Organic Solar Cells. *Chinese Journal of Chemistry* **2021**, *39* (2), 381–390. https://doi.org/10.1002/cjoc.202000289.
(51) Liu, X.; Xie, B.; Duan, C.; Wang, Z.; Fan, B.; Zhang, K.; Lin, B.; Colberts, F. J. M.; Ma, W.; Janssen, R. A. J.; Huang, F.; Cao, Y. A High Dielectric Constant Non-Fullerene Acceptor for Efficient Bulk-Heterojunction Organic Solar Cells. *J. Mater. Chem. A* **2018**, *6* (2), 395–403. https://doi.org/10.1039/C7TA10136H.
(52) Ahmad, T.; Phul, R.; Alam, P.; Lone, I. H.; Shahazad, M.; Ahmed, J.; Ahamad, T.; Alshehri, S. M. Dielectric, Optical and Enhanced Photocatalytic Properties of CuCrO2 Nanoparticles. *RSC Adv.* **2017**, *7* (44), 27549–27557. https://doi.org/10.1039/C6RA26888A.
(53) Wu, J. J.; Lu, X. J.; Lü, X. J.; Huang, F. Q. Dielectric Constant Controlled Solvothermal Synthesis of a TiO2 Photocatalyst with Tunable Crystallinity: A Strategy for Solvent Selection. In *2010 3rd International Nanoelectronics Conference (INEC)*; 2010; pp 488–489. https://doi.org/10.1109/INEC.2010.5424889.
(54) Zhang, P.; Jin, W.; Liang, W. Size-Dependent Optical Properties of Aluminum Nanoparticles: From Classical to Quantum Description. *J. Phys. Chem. C* **2018**, *122* (19), 10545–10551. https://doi.org/10.1021/acs.jpcc.8b02450.
(55) Stroyuk, O. L.; Dzhagan, V. M.; Shvalagin, V. V.; Kuchmiy, S. Ya. Size-Dependent Optical Properties of Colloidal ZnO Nanoparticles Charged by Photoexcitation. *J. Phys. Chem. C* **2010**, *114* (1), 220–225. https://doi.org/10.1021/jp908879h.
(56) Jin, R.; Higaki, T. Open Questions on the Transition between Nanoscale and Bulk Properties of Metals. *Commun Chem* **2021**, *4* (1), 1–4. https://doi.org/10.1038/s42004-021-00466-6.
(57) Peng, B.; Tang, J.; Luo, J.; Wang, P.; Ding, B.; Tam, K. C. Applications of Nanotechnology in Oil and Gas Industry: Progress and Perspective. *The Canadian Journal of Chemical Engineering* **2018**, *96* (1), 91–100. https://doi.org/10.1002/cjce.23042.
(58) Hu, P.; Cao, Y.; Han, N.; Wang, D.; Chen, J. Nanomaterials for Solar Energy Harvesting and Storage. *Journal of Nanomaterials* **2015**, *2015*, e856021. https://doi.org/10.1155/2015/856021.
(59) Ahmadi, M. H.; Ghazvini, M.; Alhuyi Nazari, M.; Ahmadi, M. A.; Pourfayaz, F.; Lorenzini, G.; Ming, T. Renewable Energy Harvesting with the Application of Nanotechnology: A Review. *International Journal of Energy Research* **2019**, *43* (4), 1387–1410. https://doi.org/10.1002/er.4282.
(60) Li, J.; Cushing, S. K.; Meng, F.; Senty, T. R.; Bristow, A. D.; Wu, N. Plasmon-Induced Resonance Energy Transfer for Solar Energy Conversion. *Nature Photonics* **2015**, *9* (9), 601–607. https://doi.org/10.1038/nphoton.2015.142.
(61) Mansuripur, M.; Zakharian, A. R.; Lesuffleur, A.; Oh, S.-H.; Jones, R. J.; Lindquist, N. C.; Im, H.; Kobyakov, A.; Moloney, J. V. Plasmonic Nano-Structures for Optical Data Storage. *Opt Express* **2009**, *17* (16), 14001–14014. https://doi.org/10.1364/oe.17.014001.

(62) Vasefi, F.; Najiminaini, M.; Kaminska, B.; Carson, J. J. L. Effect of Surface Plasmon Cross-Talk on Optical Properties of Closely Packed Nano-Hole Arrays. *Opt Express* **2011**, *19* (25), 25773–25779. https://doi.org/10.1364/OE.19.025773.
(63) Fedyanin, D. Y.; Arsenin, A. V. Transmission of Surface Plasmon Polaritons through a Nanowire Array: Mechano-Optical Modulation and Motion Sensing. *Opt Express* **2010**, *18* (19), 20115–20124. https://doi.org/10.1364/OE.18.020115.
(64) Muskens, O. L.; Giannini, V.; Sánchez-Gil, J. A.; Gómez Rivas, J. Optical Scattering Resonances of Single and Coupled Dimer Plasmonic Nanoantennas. *Opt Express* **2007**, *15* (26), 17736–17746. https://doi.org/10.1364/oe.15.017736.
(65) Fischer, H.; Martin, O. J. F. Engineering the Optical Response of Plasmonic Nanoantennas. *Opt Express* **2008**, *16* (12), 9144–9154. https://doi.org/10.1364/oe.16.009144.
(66) Jia, H.; Liu, H.; Zhong, Y. Role of Surface Plasmon Polaritons and Other Waves in the Radiation of Resonant Optical Dipole Antennas. *Sci Rep* **2015**, *5*, 8456. https://doi.org/10.1038/srep08456.
(67) Farson, D. F.; Choi, H. W.; Zimmerman, B.; Steach, J. K.; Chalmers, J. J.; Olesik, S. V.; Lee, L. J. Femtosecond Laser Micromachining of Dielectric Materials for Biomedical Applications. *Journal of Micromechanics and Microengineering* **2008**, *18* (3), 1–9. https://doi.org/10.1088/0960-1317/18/3/035020.
(68) Hattenhorst, B.; Mallach, M.; Baer, C.; Musch, T.; Barowski, J.; Rolfes, I. Dielectric Phantom Materials for Broadband Biomedical Applications. In *2017 First IEEE MTT-S International Microwave Bio Conference (IMBIOC)*; 2017; pp 1–4. https://doi.org/10.1109/IMBIOC.2017.7965802.
(69) Ma, X.; Sim, S. J. Single Plasmonic Nanostructures for Biomedical Diagnosis. *J. Mater. Chem. B* **2020**, *8* (29), 6197–6216. https://doi.org/10.1039/D0TB00351D.
(70) Premaratne, G.; Dharmaratne, A. C.; Al Mubarak, Z. H.; Mohammadparast, F.; Andiappan, M.; Krishnan, S. Multiplexed Surface Plasmon Imaging of Serum Biomolecules: Fe3O4@Au Core/Shell Nanoparticles with Plasmonic Simulation Insights. *Sensors and Actuators B: Chemical* **2019**, *299*, 126956. https://doi.org/10.1016/j.snb.2019.126956.
(71) Mubarak, Z. H. A.; Premaratne, G.; Dharmaratne, A.; Mohammadparast, F.; Andiappan, M.; Krishnan, S. Plasmonic Nucleotide Hybridization Chip for Attomolar Detection: Localized Gold and Tagged Core/Shell Nanomaterials. *Lab Chip* **2020**, *20* (4), 717–721. https://doi.org/10.1039/C9LC01150A.
(72) Kang, B.; Mackey, M. A.; El-Sayed, M. A. Nuclear Targeting of Gold Nanoparticles in Cancer Cells Induces DNA Damage, Causing Cytokinesis Arrest and Apoptosis. *J. Am. Chem. Soc.* **2010**, *132* (5), 1517–1519. https://doi.org/10.1021/ja9102698.
(73) Evano, G.; Blanchard, N. *Copper-Mediated Cross-Coupling Reactions*, 1 edition.; Wiley: Hoboken, New Jersey, 2013.
(74) Diederich, F.; Stang, P. J. *Metal-Catalyzed Cross-Coupling Reactions*; John Wiley & Sons, 2008.
(75) Jana, R.; Pathak, T. P.; Sigman, M. S. Advances in Transition Metal (Pd,Ni,Fe)-Catalyzed Cross-Coupling Reactions Using Alkyl-Organometallics as Reaction Partners. *Chem. Rev.* **2011**, *111* (3), 1417–1492. https://doi.org/10.1021/cr100327p.
(76) Chorsi, H. T. Plasmonics as a Fabrication Tool. *arXiv:2005.06005 [physics]* **2020**.
(77) Zhang, G.; Lan, C.; Bian, H.; Gao, R.; Zhou, J. Flexible, All-Dielectric Metasurface Fabricated via Nanosphere Lithography and Its Applications in Sensing. *Opt. Express, OE* **2017**, *25* (18), 22038–22045. https://doi.org/10.1364/OE.25.022038.
(78) Jensen, T. R.; Duval, M. L.; Kelly, K. L.; Lazarides, A. A.; Schatz, G. C.; Van Duyne, R. P. Nanosphere Lithography: Effect of the External Dielectric Medium on the Surface Plasmon Resonance Spectrum of a Periodic Array of Silver Nanoparticles. *J. Phys. Chem. B* **1999**, *103* (45), 9846–9853. https://doi.org/10.1021/jp9926802.

(79) Mohammadparast, F.; Dadgar, A. P.; Tirumala, R. T. A.; Mohammad, S.; Topal, C. O.; Kalkan, A. K.; Andiappan, M. C–C Coupling Reactions Catalyzed by Gold Nanoparticles: Evidence for Substrate-Mediated Leaching of Surface Atoms Using Localized Surface Plasmon Resonance Spectroscopy. *J. Phys. Chem. C* **2019**, *123* (18), 11539–11545. https://doi.org/10.1021/acs.jpcc.8b12453.
(80) Jana, N. R.; Gearheart, L.; Murphy, C. J. Seeding Growth for Size Control of 5−40 Nm Diameter Gold Nanoparticles. *Langmuir* **2001**, *17* (22), 6782–6786. https://doi.org/10.1021/la0104323.
(81) Lumerical Inc. http://www.lumerical.com/tcad-products/fdtd/ (accessed 2016 -09 -29).
(82) Cao, Y.; Manjavacas, A.; Large, N.; Nordlander, P. Electron Energy-Loss Spectroscopy Calculation in Finite-Difference Time-Domain Package. *ACS Photonics* **2015**, *2* (3), 369–375. https://doi.org/10.1021/ph500408e.
(83) Palik, E. D. *Handbook of Optical Constants of Solids*, 1 edition.; Academic Press: San Diego, Calif., 1997.
(84) Hövel, H.; Fritz, S.; Hilger, A.; Kreibig, U.; Vollmer, M. Width of Cluster Plasmon Resonances: Bulk Dielectric Functions and Chemical Interface Damping. *Phys. Rev. B* **1993**, *48* (24), 18178–18188. https://doi.org/10.1103/PhysRevB.48.18178.
(85) Palik, E. D. *Handbook of Optical Constants of Solids*; Academic Press, 1998.
(86) Nanophotonic FDTD Simulation Software - Lumerical FDTD https://www.lumerical.com/products/fdtd/ (accessed 2019 -08 -24).
(87) Cao, Y.; Manjavacas, A.; Large, N.; Nordlander, P. Electron Energy-Loss Spectroscopy Calculation in Finite-Difference Time-Domain Package. *ACS Photonics* **2015**, *2* (3), 369–375. https://doi.org/10.1021/ph500408e.
(88) Hass, G.; Ramsey, J. B.; Thun, R. Optical Properties and Structure of Cerium Dioxide Films. *J. Opt. Soc. Am.* **1958**, *48* (5), 324. https://doi.org/10.1364/JOSA.48.000324.
(89) Ordal, M. A.; Bell, R. J.; Alexander, R. W.; Long, L. L.; Querry, M. R. Optical Properties of Fourteen Metals in the Infrared and Far Infrared: Al, Co, Cu, Au, Fe, Pb, Mo, Ni, Pd, Pt, Ag, Ti, V, and W. *Appl. Opt.* **1985**, *24* (24), 4493. https://doi.org/10.1364/AO.24.004493.
(90) Siefke, T.; Kroker, S.; Pfeiffer, K.; Puffky, O.; Dietrich, K.; Franta, D.; Ohlídal, I.; Szeghalmi, A.; Kley, E.; Tünnermann, A. Materials Pushing the Application Limits of Wire Grid Polarizers Further into the Deep Ultraviolet Spectral Range. *Advanced Optical Materials* **2016**, *4* (11), 1780–1786. https://doi.org/10.1002/adom.201600250.
(91) Sarkar, S.; Gupta, V.; Kumar, M.; Schubert, J.; Probst, P. T.; Joseph, J.; König, T. A. F. Hybridized Guided-Mode Resonances via Colloidal Plasmonic Self-Assembled Grating. *ACS Appl. Mater. Interfaces* **2019**, *11* (14), 13752–13760. https://doi.org/10.1021/acsami.8b20535.
(92) Merritt, J. M.; Andiappan, M.; Pietz, M. A.; Richey, R. N.; Sullivan, K. A.; Kjell, D. P. Mitigating the Risk of Coprecipitation of Pinacol during Isolation from Telescoped Miyaura Borylation and Suzuki Couplings Utilizing Boron Pinacol Esters: Use of Modeling for Process Design. *Org. Process Res. Dev.* **2016**, *20* (2), 178–188. https://doi.org/10.1021/acs.oprd.5b00324.
(93) Cooper, T. W. J.; Campbell, I. B.; Macdonald, S. J. F. Factors Determining the Selection of Organic Reactions by Medicinal Chemists and the Use of These Reactions in Arrays (Small Focused Libraries). *Angewandte Chemie International Edition* **2010**, *49* (44), 8082–8091. https://doi.org/10.1002/anie.201002238.
(94) Q3D Elemental Impurities - Guidance for Industry https://www.fda.gov/downloads/drugs/guidances/ucm371025.pdf (accessed 2017 -07 -30).
(95) Farina, V. High-Turnover Palladium Catalysts in Cross-Coupling and Heck Chemistry: A Critical Overview. *Adv. Synth. Catal.* **2004**, *346* (13–15), 1553–1582. https://doi.org/10.1002/adsc.200404178.

(96) Phan, N. T. S.; Van Der Sluys, M.; Jones, C. W. On the Nature of the Active Species in Palladium Catalyzed Mizoroki–Heck and Suzuki–Miyaura Couplings – Homogeneous or Heterogeneous Catalysis, A Critical Review. *Adv. Synth. Catal.* **2006**, *348* (6), 609–679. https://doi.org/10.1002/adsc.200505473.
(97) Balanta, A.; Godard, C.; Claver, C. Pd Nanoparticles for C–C Coupling Reactions. *Chemical Society Reviews* **2011**, *40* (10), 4973–4985. https://doi.org/10.1039/C1CS15195A.
(98) Peiris, S.; Sarina, S.; Han, C.; Xiao, Q.; Zhu, H.-Y. Silver and Palladium Alloy Nanoparticle Catalysts: Reductive Coupling of Nitrobenzene through Light Irradiation. *Dalton Transactions* **2017**, *46* (32), 10665–10672. https://doi.org/10.1039/C7DT00418D.
(99) Xiao, Q.; Sarina, S.; Bo, A.; Jia, J.; Liu, H.; Arnold, D. P.; Huang, Y.; Wu, H.; Zhu, H. Visible Light-Driven Cross-Coupling Reactions at Lower Temperatures Using a Photocatalyst of Palladium and Gold Alloy Nanoparticles. *ACS Catal.* **2014**, *4* (6), 1725–1734. https://doi.org/10.1021/cs5000284.
(100) Hutchings, G. *Nanocatalysis: Synthesis and Applications*, 1 edition.; Polshettiwar, V., Asefa, T., Eds.; Wiley, 2013.
(101) Garcia, P.; Malacria, M.; Aubert, C.; Gandon, V.; Fensterbank, L. Gold-Catalyzed Cross-Couplings: New Opportunities for C-C Bond Formation. *ChemCatChem* **2010**, *2* (5), 493–497. https://doi.org/10.1002/cctc.200900319.
(102) Molnár, Á. Efficient, Selective, and Recyclable Palladium Catalysts in Carbon-Carbon Coupling Reactions. *Chem. Rev.* **2011**, *111* (3), 2251–2320. https://doi.org/10.1021/cr100355b.
(103) Maria Thomas, A.; Sujatha, A.; Anilkumar, G. Recent Advances and Perspectives in Copper-Catalyzed Sonogashira Coupling Reactions. *RSC Advances* **2014**, *4* (42), 21688–21698. https://doi.org/10.1039/C4RA02529F.
(104) Boronat, M.; Combita, D.; Concepción, P.; Corma, A.; García, H.; Juárez, R.; Laursen, S.; de Dios López-Castro, J. Making C–C Bonds with Gold: Identification of Selective Gold Sites for Homo- and Cross-Coupling Reactions between Iodobenzene and Alkynes. *J. Phys. Chem. C* **2012**, *116* (47), 24855–24867. https://doi.org/10.1021/jp3071585.
(105) Li, Y.; El-Sayed, M. A. The Effect of Stabilizers on the Catalytic Activity and Stability of Pd Colloidal Nanoparticles in the Suzuki Reactions in Aqueous Solution†. *J. Phys. Chem. B* **2001**, *105* (37), 8938–8943. https://doi.org/10.1021/jp010904m.
(106) Pérez-Lorenzo, M. Palladium Nanoparticles as Efficient Catalysts for Suzuki Cross-Coupling Reactions. *J. Phys. Chem. Lett.* **2012**, *3* (2), 167–174. https://doi.org/10.1021/jz2013984.
(107) Feng, L.; Chong, H.; Li, P.; Xiang, J.; Fu, F.; Yang, S.; Yu, H.; Sheng, H.; Zhu, M. Pd–Ni Alloy Nanoparticles as Effective Catalysts for Miyaura–Heck Coupling Reactions. *J. Phys. Chem. C* **2015**, *119* (21), 11511–11515. https://doi.org/10.1021/jp510988m.
(108) Narayanan, R.; El-Sayed, M. A. Effect of Colloidal Catalysis on the Nanoparticle Size Distribution: Dendrimer−Pd vs PVP−Pd Nanoparticles Catalyzing the Suzuki Coupling Reaction. *J. Phys. Chem. B* **2004**, *108* (25), 8572–8580. https://doi.org/10.1021/jp037169u.
(109) Zhu, M.; Diao, G. Magnetically Recyclable Pd Nanoparticles Immobilized on Magnetic Fe3O4@C Nanocomposites: Preparation, Characterization, and Their Catalytic Activity toward Suzuki and Heck Coupling Reactions. *J. Phys. Chem. C* **2011**, *115* (50), 24743–24749. https://doi.org/10.1021/jp206116e.
(110) Pd(0) Nanoparticles Supported Organofunctionalized Clay Driving C–C Coupling Reactions under Benign Conditions through a Pd(0)/Pd(II) Redox Interplay - The Journal of Physical Chemistry C (ACS Publications) https://pubs.acs.org/doi/10.1021/jp410709n (accessed 2019 -02 -13).

(111) Facile Deposition of Pd Nanoparticles on Carbon Nanotube Microparticles and Their Catalytic Activity for Suzuki Coupling Reactions - The Journal of Physical Chemistry C (ACS Publications) https://pubs.acs.org/doi/10.1021/jp800610q (accessed 2019 -02 -13).
(112) Park, J. C.; Heo, E.; Kim, A.; Kim, M.; Park, K. H.; Song, H. Extremely Active Pd@pSiO2 Yolk–Shell Nanocatalysts for Suzuki Coupling Reactions of Aryl Halides. *J. Phys. Chem. C* **2011**, *115* (32), 15772–15777. https://doi.org/10.1021/jp2021825.
(113) Karousis, N.; Tsotsou, G.-E.; Evangelista, F.; Rudolf, P.; Ragoussis, N.; Tagmatarchis, N. Carbon Nanotubes Decorated with Palladium Nanoparticles: Synthesis, Characterization, and Catalytic Activity. *J. Phys. Chem. C* **2008**, *112* (35), 13463–13469. https://doi.org/10.1021/jp802920k.
(114) Jang, Y.; Chung, J.; Kim, S.; Jun, S. W.; Kim, B. H.; Lee, D. W.; Kim, B. M.; Hyeon, T. Simple Synthesis of Pd–Fe3O4 Heterodimer Nanocrystals and Their Application as a Magnetically Recyclable Catalyst for Suzuki Cross-Coupling Reactions. *Phys. Chem. Chem. Phys.* **2011**, *13* (7), 2512–2516. https://doi.org/10.1039/C0CP01680B.
(115) Pachón, L. D.; Thathagar, M. B.; Hartl, F.; Rothenberg, G. Palladium-Coated Nickel Nanoclusters: New Hiyama Cross-Coupling Catalysts. *Phys. Chem. Chem. Phys.* **2006**, *8* (1), 151–157. https://doi.org/10.1039/B513587G.
(116) Jia, C.-J.; Schüth, F. Colloidal Metal Nanoparticles as a Component of Designed Catalyst. *Phys. Chem. Chem. Phys.* **2011**, *13* (7), 2457–2487. https://doi.org/10.1039/C0CP02680H.
(117) Widegren, J. A.; Finke, R. G. A Review of the Problem of Distinguishing True Homogeneous Catalysis from Soluble or Other Metal-Particle Heterogeneous Catalysis under Reducing Conditions. *Journal of Molecular Catalysis A: Chemical* **2003**, *198* (1–2), 317–341. https://doi.org/10.1016/S1381-1169(02)00728-8.
(118) Biffis, A.; Zecca, M.; Basato, M. Metallic Palladium in the Heck Reaction: Active Catalyst or Convenient Precursor? *Eur. J. Inorg. Chem.* **2001**, *2001* (5), 1131–1133. https://doi.org/10.1002/1099-0682(200105)2001:5<1131::AID-EJIC1131>3.0.CO;2-3.
(119) Schmidt, A. F.; Al-Halaiqa, A.; Smirnov, V. V. New Approaches to Heck Reaction Testing for Homogeneity-Heterogeneity. *Kinet Catal* **2008**, *49* (3), 395–400. https://doi.org/10.1134/S0023158408030129.
(120) Ellis, P. J.; Fairlamb, I. J. S.; Hackett, S. F. J.; Wilson, K.; Lee, A. F. Evidence for the Surface-Catalyzed Suzuki–Miyaura Reaction over Palladium Nanoparticles: An Operando XAS Study. *Angewandte Chemie International Edition* **2010**, *49* (10), 1820–1824. https://doi.org/10.1002/anie.200906675.
(121) Song, H. M.; Moosa, B. A.; Khashab, N. M. Water-Dispersable Hybrid Au–Pd Nanoparticles as Catalysts in Ethanol Oxidation, Aqueous Phase Suzuki–Miyaura and Heck Reactions. *J. Mater. Chem.* **2012**, *22* (31), 15953–15959. https://doi.org/10.1039/C2JM32702C.
(122) Fang, P.-P.; Jutand, A.; Tian, Z.-Q.; Amatore, C. Au–Pd Core–Shell Nanoparticles Catalyze Suzuki–Miyaura Reactions in Water through Pd Leaching. *Angewandte Chemie International Edition 50* (51), 12184–12188. https://doi.org/10.1002/anie.201103465.
(123) C. Elias, W.; M. Signori, A.; Zaramello, L.; Lange Albuquerque, B.; Coelho de Oliveira, D.; Domingos, J. Mechanism of a Suzuki-Type Homocoupling Reaction Catalyzed by Palladium Nanocubes. *ACS Catalysis* **2017**, *7*, 1462–1469. https://doi.org/10.1021/acscatal.6b03490.
(124) Collins, G.; Schmidt, M.; O'Dwyer, C.; Holmes, J. D.; McGlacken, G. P. The Origin of Shape Sensitivity in Palladium-Catalyzed Suzuki–Miyaura Cross Coupling Reactions. *Angewandte Chemie International Edition 53* (16), 4142–4145. https://doi.org/10.1002/anie.201400483.
(125) González-Arellano, C.; Abad, A.; Corma, A.; García, H.; Iglesias, M.; Sánchez, F. Catalysis by Gold(I) and Gold(III): A Parallelism between Homo- and Heterogeneous Catalysts for

Copper-Free Sonogashira Cross-Coupling Reactions. *Angewandte Chemie International Edition* **2007**, *46* (9), 1536–1538. https://doi.org/10.1002/anie.200604746.
(126) Marimuthu, A.; Zhang, J.; Linic, S. Tuning Selectivity in Propylene Epoxidation by Plasmon Mediated Photo-Switching of Cu Oxidation State. *Science* **2013**, *339* (6127), 1590–1593. https://doi.org/10.1126/science.1231631.
(127) Willets, K. A.; Van Duyne, R. P. Localized Surface Plasmon Resonance Spectroscopy and Sensing. *Annu Rev Phys Chem* **2007**, *58*, 267–297. https://doi.org/10.1146/annurev.physchem.58.032806.104607.
(128) See Supporting Information. .
(129) Sagadevan, A.; Ragupathi, A.; Lin, C.-C.; Hwu, J. R.; Hwang, K. C. Visible-Light Initiated Copper(I)-Catalysed Oxidative C–N Coupling of Anilines with Terminal Alkynes: One-Step Synthesis of α-Ketoamides. *Green Chem.* **2015**, *17* (2), 1113–1119. https://doi.org/10.1039/C4GC01623H.
(130) Sagadevan, A.; Charpe, V. P.; Hwang, K. C. Copper(I) Chloride Catalysed Room Temperature Csp–Csp Homocoupling of Terminal Alkynes Mediated by Visible Light. *Catal. Sci. Technol.* **2016**, *6* (21), 7688–7692. https://doi.org/10.1039/C6CY01400C.
(131) Mulvaney, P. Surface Plasmon Spectroscopy of Nanosized Metal Particles. *Langmuir* **1996**, *12* (3), 788–800. https://doi.org/10.1021/la9502711.
(132) Cheng, Y.; Wang, M.; Borghs, G.; Chen, H. Gold Nanoparticle Dimers for Plasmon Sensing. *Langmuir* **2011**, *27* (12), 7884–7891. https://doi.org/10.1021/la200840m.
(133) Phenylacetylene. https://webbook.nist.gov/cgi/cbook.cgi?ID=C536743&Mask=400#UV-Vis-Spec (accessed 2017 -12 -02).
(134) Seeding Growth for Size Control of 5−40 nm Diameter Gold Nanoparticles | Langmuir https://pubs.acs.org/doi/10.1021/la0104323 (accessed 2020 -04 -01).
(135) Diederich, F.; Stang, P. J. Metal-Catalyzed Cross-Coupling Reactions. Wiley-VCH 1998.
(136) van Koten, G. Copper-Mediated Cross-Coupling Reactions. Editors: Gwilherm Evano and Nicolas Blanchard. *Adv. Synth. Catal.* **2014**, *356* (18), 3913–3915. https://doi.org/10.1002/adsc.201400950.
(137) Cooper, T. W. J.; Campbell, I. B.; Macdonald, S. J. F. Factors Determining the Selection of Organic Reactions by Medicinal Chemists and the Use of These Reactions in Arrays (Small Focused Libraries). *Angewandte Chemie International Edition* **2010**, *49* (44), 8082–8091. https://doi.org/10.1002/anie.201002238.
(138) Merritt, J. M.; Andiappan, M.; Pietz, M. A.; Richey, R. N.; Sullivan, K. A.; Kjell, D. P. Mitigating the Risk of Coprecipitation of Pinacol during Isolation from Telescoped Miyaura Borylation and Suzuki Couplings Utilizing Boron Pinacol Esters: Use of Modeling for Process Design. *Org. Process Res. Dev.* **2016**, *20* (2), 178–188. https://doi.org/10.1021/acs.oprd.5b00324.
(139) Singh, U. K.; Vannice, M. A. Kinetics of Liquid-Phase Hydrogenation Reactions over Supported Metal Catalysts — a Review. *Applied Catalysis A: General* **2001**, *213* (1), 1–24. https://doi.org/10.1016/S0926-860X(00)00885-1.
(140) Front Matter. In *Green Chemistry in the Pharmaceutical Industry*; Dunn, P. J., Wells, A. S., Williams, M. T., Eds.; Wiley-VCH Verlag GmbH & Co. KGaA: Weinheim, Germany, 2010; p I–XVIII. https://doi.org/10.1002/9783527629688.fmatter.
(141) Ciriminna, R.; Pagliaro, M. Green Chemistry in the Fine Chemicals and Pharmaceutical Industries. *Org. Process Res. Dev.* **2013**, *17* (12), 1479–1484. https://doi.org/10.1021/op400258a.
(142) Jana, R.; Pathak, T. P.; Sigman, M. S. Advances in Transition Metal (Pd,Ni,Fe)-Catalyzed Cross-Coupling Reactions Using Alkyl-Organometallics as Reaction Partners. *Chem. Rev.* **2011**, *111* (3), 1417–1492. https://doi.org/10.1021/cr100327p.

(143) Kasparian, A. J.; Savarin, C.; Allgeier, A. M.; Walker, S. D. Selective Catalytic Hydrogenation of Nitro Groups in the Presence of Activated Heteroaryl Halides. *J. Org. Chem.* **2011**, *76* (23), 9841–9844. https://doi.org/10.1021/jo2015664.

(144) Allgeier, A. M.; Andersen, D.; Bartberger, M. D.; Bunel, E. E.; Larsen, R. D.; Liu, P.; Storz, T.; Tedrow, J. S. Reductive Amination Without the Aldehyde: Use of a Ketolactol as an Aldehyde Surrogate. *Top Catal* **2014**, *57* (17–20), 1335–1341. https://doi.org/10.1007/s11244-014-0300-x.

(145) Moschetta, E. G.; Negretti, S.; Chepiga, K. M.; Brunelli, N. A.; Labreche, Y.; Feng, Y.; Rezaei, F.; Lively, R. P.; Koros, W. J.; Davies, H. M. L.; Jones, C. W. Composite Polymer/Oxide Hollow Fiber Contactors: Versatile and Scalable Flow Reactors for Heterogeneous Catalytic Reactions in Organic Synthesis. *Angew. Chem. Int. Ed.* **2015**, *54* (22), 6470–6474. https://doi.org/10.1002/anie.201500841.

(146) Rizkin, B. A.; Hartman, R. L. Catalytic Activity of Pd/Hydrophilic Phosphine Ligand in the Interface of an Aqueous-Phase Cu-Free Sonogashira Coupling. *React. Chem. Eng.* **2018**, *3* (3), 251–257. https://doi.org/10.1039/C8RE00021B.

(147) Domier, R. C.; Moore, J. N.; Shaughnessy, K. H.; Hartman, R. L. Kinetic Analysis of Aqueous-Phase Pd-Catalyzed, Cu-Free Direct Arylation of Terminal Alkynes Using a Hydrophilic Ligand. *Org. Process Res. Dev.* **2013**, *17* (10), 1262–1271. https://doi.org/10.1021/op4001274.

(148) Noël, T.; Naber, J. R.; Hartman, R. L.; McMullen, J. P.; Jensen, K. F.; Buchwald, S. L. Palladium-Catalyzed Amination Reactions in Flow: Overcoming the Challenges of Clogging via Acoustic Irradiation. *Chem. Sci.* **2011**, *2* (2), 287–290. https://doi.org/10.1039/C0SC00524J.

(149) Hartman, R. L.; McMullen, J. P.; Jensen, K. F. Deciding Whether To Go with the Flow: Evaluating the Merits of Flow Reactors for Synthesis. *Angew. Chem. Int. Ed.* **2011**, *50* (33), 7502–7519. https://doi.org/10.1002/anie.201004637.

(150) Wendlandt, A. E.; Suess, A. M.; Stahl, S. S. Copper-Catalyzed Aerobic Oxidative C□H Functionalizations: Trends and Mechanistic Insights. *Angew. Chem. Int. Ed.* **2011**, *50* (47), 11062–11087. https://doi.org/10.1002/anie.201103945.

(151) He, Y.; Rezaei, F.; Kapila, S.; Rownaghi, A. A. Engineering Porous Polymer Hollow Fiber Microfluidic Reactors for Sustainable C–H Functionalization. *ACS Appl. Mater. Interfaces* **2017**, *9* (19), 16288–16295. https://doi.org/10.1021/acsami.7b04092.

(152) Gao, H.-Y.; Wagner, H.; Zhong, D.; Franke, J.-H.; Studer, A.; Fuchs, H. Glaser Coupling at Metal Surfaces. *Angewandte Chemie International Edition* **2013**, *52* (14), 4024–4028. https://doi.org/10.1002/anie.201208597.

(153) Ajitha, M. J.; Pary, F.; Nelson, T. L.; Musaev, D. G. Unveiling the Role of Base and Additive in the Ullmann-Type of Arene-Aryl C–C Coupling Reaction. *ACS Catal.* **2018**, *8* (6), 4829–4837. https://doi.org/10.1021/acscatal.8b00837.

(154) Bryan, M. C.; Wernick, D.; Hein, C. D.; Petersen, J. V.; Eschelbach, J. W.; Doherty, E. M. Evaluation of a Commercial Packed Bed Flow Hydrogenator for Reaction Screening, Optimization, and Synthesis. *Beilstein J. Org. Chem.* **2011**, *7*, 1141–1149. https://doi.org/10.3762/bjoc.7.132.

(155) Sulmonetti, T. P.; Pang, S. H.; Claure, M. T.; Lee, S.; Cullen, D. A.; Agrawal, P. K.; Jones, C. W. Vapor Phase Hydrogenation of Furfural over Nickel Mixed Metal Oxide Catalysts Derived from Layered Double Hydroxides. *Applied Catalysis A: General* **2016**, *517*, 187–195. https://doi.org/10.1016/j.apcata.2016.03.005.

(156) A Snapshot of Priority Technology Areas Across the Federal Government https://www.whitehouse.gov/sites/whitehouse.gov/files/images/Blog/NSTC%20SAM%20technology%20areas%20snapshot.pdf (accessed 2017 -02 -01).

(157) Bhanage, B. M.; Arai, M. CATALYST PRODUCT SEPARATION TECHNIQUES IN HECK REACTION. *Catalysis Reviews* **2001**, *43* (3), 315–344. https://doi.org/10.1081/CR-100107480.
(158) Garrett, C. E.; Prasad, K. The Art of Meeting Palladium Specifications in Active Pharmaceutical Ingredients Produced by Pd-Catalyzed Reactions. *Advanced Synthesis & Catalysis* **2004**, *346* (8), 889–900. https://doi.org/10.1002/adsc.200404071.
(159) *Nanocatalysis: Synthesis and Applications*; Polshettiwar, V., Asefa, T., Eds.; John Wiley & Sons, Inc: Hoboken, New Jersey, 2013.
(160) Fihri, A.; Bouhrara, M.; Nekoueishahraki, B.; Basset, J.-M.; Polshettiwar, V. Nanocatalysts for Suzuki Cross-Coupling Reactions. *Chem. Soc. Rev.* **2011**, *40* (10), 5181. https://doi.org/10.1039/c1cs15079k.
(161) Beaumont, S. K. Heterogeneously Catalyzing C-C Coupling Reactions with Precious Metal Nanoparticles. *J. Chem. Technol. Biotechnol.* **2012**, *87* (5), 595–600. https://doi.org/10.1002/jctb.3748.
(162) Balanta, A.; Godard, C.; Claver, C. Pd Nanoparticles for C–C Coupling Reactions. *Chem. Soc. Rev.* **2011**, *40* (10), 4973. https://doi.org/10.1039/c1cs15195a.
(163) Yin; Liebscher, J. Carbon−Carbon Coupling Reactions Catalyzed by Heterogeneous Palladium Catalysts. *Chem. Rev.* **2007**, *107* (1), 133–173. https://doi.org/10.1021/cr0505674.
(164) Widegren, J. A.; Finke, R. G. A Review of the Problem of Distinguishing True Homogeneous Catalysis from Soluble or Other Metal-Particle Heterogeneous Catalysis under Reducing Conditions. *Journal of Molecular Catalysis A: Chemical* **2003**, *198* (1–2), 317–341. https://doi.org/10.1016/S1381-1169(02)00728-8.
(165) Schmidt, A. F.; Al-Halaiqa, A.; Smirnov, V. V. New Approaches to Heck Reaction Testing for Homogeneity-Heterogeneity. *Kinet Catal* **2008**, *49* (3), 395–400. https://doi.org/10.1134/S0023158408030129.
(166) Molnár, Á. Efficient, Selective, and Recyclable Palladium Catalysts in Carbon−Carbon Coupling Reactions. *Chem. Rev.* **2011**, *111* (3), 2251–2320. https://doi.org/10.1021/cr100355b.
(167) Phan, N. T. S.; Van Der Sluys, M.; Jones, C. W. On the Nature of the Active Species in Palladium Catalyzed Mizoroki–Heck and Suzuki–Miyaura Couplings – Homogeneous or Heterogeneous Catalysis, A Critical Review. *Adv. Synth. Catal.* **2006**, *348* (6), 609–679. https://doi.org/10.1002/adsc.200505473.
(168) Pérez-Lorenzo, M. Palladium Nanoparticles as Efficient Catalysts for Suzuki Cross-Coupling Reactions. *J. Phys. Chem. Lett.* **2012**, *3* (2), 167–174. https://doi.org/10.1021/jz2013984.
(169) Song, H. M.; Moosa, B. A.; Khashab, N. M. Water-Dispersable Hybrid Au–Pd Nanoparticles as Catalysts in Ethanol Oxidation, Aqueous Phase Suzuki–Miyaura and Heck Reactions. *J. Mater. Chem.* **2012**, *22* (31), 15953. https://doi.org/10.1039/c2jm32702c.
(170) Fang, P.-P.; Jutand, A.; Tian, Z.-Q.; Amatore, C. Au-Pd Core-Shell Nanoparticles Catalyze Suzuki-Miyaura Reactions in Water through Pd Leaching. *Angew. Chem. Int. Ed.* **2011**, *50* (51), 12184–12188. https://doi.org/10.1002/anie.201103465.
(171) Collins, G.; Schmidt, M.; O'Dwyer, C.; Holmes, J. D.; McGlacken, G. P. The Origin of Shape Sensitivity in Palladium-Catalyzed Suzuki-Miyaura Cross Coupling Reactions. *Angew. Chem. Int. Ed.* **2014**, *53* (16), 4142–4145. https://doi.org/10.1002/anie.201400483.
(172) Elias, W. C.; Signori, A. M.; Zaramello, L.; Albuquerque, B. L.; de Oliveira, D. C.; Domingos, J. B. Mechanism of a Suzuki-Type Homocoupling Reaction Catalyzed by Palladium Nanocubes. *ACS Catal.* **2017**, *7* (2), 1462–1469. https://doi.org/10.1021/acscatal.6b03490.

(173) Farina, V. High-Turnover Palladium Catalysts in Cross-Coupling and Heck Chemistry: A Critical Overview. *Adv. Synth. Catal.* **2004**, *346* (13–15), 1553–1582. https://doi.org/10.1002/adsc.200404178.
(174) Peiris, S.; Sarina, S.; Han, C.; Xiao, Q.; Zhu, H.-Y. Silver and Palladium Alloy Nanoparticle Catalysts: Reductive Coupling of Nitrobenzene through Light Irradiation. *Dalton Trans* **2017**, *46* (32), 10665–10672. https://doi.org/10.1039/c7dt00418d.
(175) Xiao, Q.; Sarina, S.; Bo, A.; Jia, J.; Liu, H.; Arnold, D. P.; Huang, Y.; Wu, H.; Zhu, H. Visible Light-Driven Cross-Coupling Reactions at Lower Temperatures Using a Photocatalyst of Palladium and Gold Alloy Nanoparticles. *ACS Catal.* **2014**, *4* (6), 1725–1734. https://doi.org/10.1021/cs5000284.
(176) Garcia, P.; Malacria, M.; Aubert, C.; Gandon, V.; Fensterbank, L. Gold-Catalyzed Cross-Couplings: New Opportunities for C□C Bond Formation. *ChemCatChem* **2010**, *2* (5), 493–497. https://doi.org/10.1002/cctc.200900319.
(177) Kyriakou, G.; Beaumont, S. K.; Humphrey, S. M.; Antonetti, C.; Lambert, R. M. Sonogashira Coupling Catalyzed by Gold Nanoparticles: Does Homogeneous or Heterogeneous Catalysis Dominate? *ChemCatChem* **2010**, *2* (11), 1444–1449. https://doi.org/10.1002/cctc.201000154.
(178) Biffis, A.; Zecca, M.; Basato, M. Metallic Palladium in the Heck Reaction: Active Catalyst or Convenient Precursor? 3.
(179) Ellis, P. J.; Fairlamb, I. J. S.; Hackett, S. F. J.; Wilson, K.; Lee, A. F. Evidence for the Surface-Catalyzed Suzuki-Miyaura Reaction over Palladium Nanoparticles: An Operando XAS Study. *Angew. Chem. Int. Ed.* **2010**, *49* (10), 1820–1824. https://doi.org/10.1002/anie.200906675.
(180) Thomas, A. M.; Sujatha, A.; Anilkumar, G. Recent Advances and Perspectives in Copper-Catalyzed Sonogashira Coupling Reactions. *RSC Adv.* **2014**, *4* (42), 21688–21698. https://doi.org/10.1039/C4RA02529F.
(181) Marimuthu, A.; Zhang, J.; Linic, S. Tuning Selectivity in Propylene Epoxidation by Plasmon Mediated Photo-Switching of Cu Oxidation State. *Science* **2013**, *339* (6127), 1590–1593. https://doi.org/10.1126/science.1231631.
(182) Xiao, Q.; Sarina, S.; Jaatinen, E.; Jia, J.; Arnold, D. P.; Liu, H.; Zhu, H. Efficient Photocatalytic Suzuki Cross-Coupling Reactions on Au–Pd Alloy Nanoparticles under Visible Light Irradiation. *Green Chem.* **2014**, *16* (9), 4272. https://doi.org/10.1039/C4GC00588K.
(183) Arunachalam, S.; Ragupathi, A.; Lin, C.-C.; Hwu, J. R.; Hwang, K. C. Visible-Light Initiated Copper(I)-Catalysed Oxidative C–N Coupling of Anilines with Terminal Alkynes: One-Step Synthesis of α-Ketoamides. *Green Chem.* **2015**, *17* (2), 1113–1119. https://doi.org/10.1039/C4GC01623H.
(184) Arunachalam, S.; Charpe, V. P.; Hwang, K. C. Copper(I) Chloride Catalysed Room Temperature C_{sp}–C_{sp} Homocoupling of Terminal Alkynes Mediated by Visible Light. *Catal. Sci. Technol.* **2016**, *6* (21), 7688–7692. https://doi.org/10.1039/C6CY01400C.
(185) Prakash, J.; Kumar, V.; Kroon, R. E.; Asokan, K.; Rigato, V.; Chae, K. H.; Gautam, S.; Swart, H. C. Optical and Surface Enhanced Raman Scattering Properties of Au Nanoparticles Embedded in and Located on a Carbonaceous Matrix. *Phys. Chem. Chem. Phys.* **2016**, *18* (4), 2468–2480. https://doi.org/10.1039/C5CP06134B.
(186) Ross, M. B.; Mirkin, C. A.; Schatz, G. C. Optical Properties of One-, Two-, and Three-Dimensional Arrays of Plasmonic Nanostructures. *J. Phys. Chem. C* **2016**, *120* (2), 816–830. https://doi.org/10.1021/acs.jpcc.5b10800.
(187) Lu, X.; Rycenga, M.; Skrabalak, S. E.; Wiley, B.; Xia, Y. Chemical Synthesis of Novel Plasmonic Nanoparticles. *Annual Review of Physical Chemistry* **2009**, *60* (1), 167–192. https://doi.org/10.1146/annurev.physchem.040808.090434.

(188) Sherry, L. J.; Chang, S.-H.; Schatz, G. C.; Van Duyne, R. P.; Wiley, B. J.; Xia, Y. Localized Surface Plasmon Resonance Spectroscopy of Single Silver Nanocubes. *Nano Lett.* **2005**, *5* (10), 2034–2038. https://doi.org/10.1021/nl0515753.
(189) Wang, H.; Brandl, D. W.; Nordlander, P.; Halas, N. J. Plasmonic Nanostructures: Artificial Molecules. *Acc. Chem. Res.* **2007**, *40* (1), 53–62. https://doi.org/10.1021/ar0401045.
(190) Brus, L. Noble Metal Nanocrystals: Plasmon Electron Transfer Photochemistry and Single-Molecule Raman Spectroscopy. *Acc. Chem. Res.* **2008**, *41* (12), 1742–1749. https://doi.org/10.1021/ar800121r.
(191) Michaels, A. M.; Jiang; Brus, L. Ag Nanocrystal Junctions as the Site for Surface-Enhanced Raman Scattering of Single Rhodamine 6G Molecules. *J. Phys. Chem. B* **2000**, *104* (50), 11965–11971. https://doi.org/10.1021/jp0025476.
(192) Link, S.; El-Sayed, M. A. Optical Properties and Ultrafast Dynamics of Metallic Nanocrystals. *Annual Review of Physical Chemistry* **2003**, *54* (1), 331–366. https://doi.org/10.1146/annurev.physchem.54.011002.103759.
(193) Jarrett, J. W.; Zhao, T.; Johnson, J. S.; Knappenberger, K. L. Investigating Plasmonic Structure-Dependent Light Amplification and Electronic Dynamics Using Advances in Nonlinear Optical Microscopy. *J. Phys. Chem. C* **2015**, *119* (28), 15779–15800. https://doi.org/10.1021/acs.jpcc.5b02494.
(194) Devaux, E.; Laluet, J.-Y.; Stein, B.; Genet, C.; Ebbesen, T.; Weeber, J.-C.; Dereux, A. Refractive Micro-Optical Elements for Surface Plasmons: From Classical to Gradient Index Optics. *Opt. Express, OE* **2010**, *18* (20), 20610–20619. https://doi.org/10.1364/OE.18.020610.
(195) Andiappan Marimuthu, J. Z. Tuning Selectivity in Propylene Epoxidation by Plasmon Mediated Photo-Switching of Cu Oxidation State. *Science (New York, N.Y.)* **2013**, *339* (6127), 1590–1593. https://doi.org/10.1126/science.1231631.
(196) Christopher, P.; Xin, H.; Marimuthu, A.; Linic, S. Singular Characteristics and Unique Chemical Bond Activation Mechanisms of Photocatalytic Reactions on Plasmonic Nanostructures. *Nat Mater* **2012**, *11* (12), 1044–1050. https://doi.org/10.1038/nmat3454.
(197) Hou, W.; Cronin, S. B. A Review of Surface Plasmon Resonance-Enhanced Photocatalysis. *Adv. Funct. Mater.* **2013**, *23* (13), 1612–1619. https://doi.org/10.1002/adfm.201202148.
(198) Cushing, S. K.; Li, J.; Meng, F.; Senty, T. R.; Suri, S.; Zhi, M.; Li, M.; Bristow, A. D.; Wu, N. Photocatalytic Activity Enhanced by Plasmonic Resonant Energy Transfer from Metal to Semiconductor. *J. Am. Chem. Soc.* **2012**, *134* (36), 15033–15041. https://doi.org/10.1021/ja305603t.
(199) Thrithamarassery, G. D.; Xu, Z.; Liu, Y.; Izquierdo, R.; Ma, D. Recent Advancements in Plasmon-Enhanced Promising Third-Generation Solar Cells. *Nanophotonics* **2017**, *6* (1), 153–175. https://doi.org/10.1515/nanoph-2016-0111.
(200) Sandén, S.; Akitsu, K.; Törngren, B.; Ylinen, A.; Smått, J.-H.; Kubo, T.; Matsumura, M.; Otani, N.; Segawa, H.; Österbacka, R. Plasmon-Enhanced Polymer-Sensitized Solar Cells. *J. Phys. Chem. C* **2015**, *119* (10), 5570–5576. https://doi.org/10.1021/jp5097458.
(201) Jang, Y. H.; Jang, Y. J.; Kim, S.; Quan, L. N.; Chung, K.; Kim, D. H. Plasmonic Solar Cells: From Rational Design to Mechanism Overview. *Chem. Rev.* **2016**, *116* (24), 14982–15034. https://doi.org/10.1021/acs.chemrev.6b00302.
(202) Feng, L.; Niu, M.; Wen, Z.; Hao, X. Recent Advances of Plasmonic Organic Solar Cells: Photophysical Investigations. *Polymers* **2018**, *10* (2), 123. https://doi.org/10.3390/polym10020123.
(203) Şarlı, N. Artificial Magnetism in a Carbon Diamond Nanolattice with the Spin Orientation Effect. *Diamond and Related Materials* **2016**, *64*. https://doi.org/10.1016/j.diamond.2016.01.027.

(204) Cong, J.; Zhou, Z.; Yun, B.; Yao, H.; Ren, N. Artificial Magnetism of Cross Shaped Metamaterial in Green Light Frequencies. *Optical Materials* **2015**, *50*, 123–127. https://doi.org/10.1016/j.optmat.2015.10.009.
(205) Markovich, D.; Baryshnikova, K.; Shalin, A.; Samusev, A.; Krasnok, A.; Belov, P.; Ginzburg, P. Enhancement of Artificial Magnetism via Resonant Bianisotropy. *Scientific Reports* **2016**, *6*, 22546. https://doi.org/10.1038/srep22546.
(206) Liu, Y.; Zhang, X. Metasurfaces for Manipulating Surface Plasmons. *Appl. Phys. Lett.* **2013**, *103* (14), 141101. https://doi.org/10.1063/1.4821444.
(207) Cai, W.; Chettiar, U. K.; Kildishev, A. V.; Shalaev, V. M. Optical Cloaking with Metamaterials. *Nature Photon* **2007**, *1* (4), 224–227. https://doi.org/10.1038/nphoton.2007.28.
(208) Shin, D.; Urzhumov, Y.; Jung, Y.; Kang, G.; Baek, S.; Choi, M.; Park, H.; Kim, K.; Smith, D. R. Broadband Electromagnetic Cloaking with Smart Metamaterials. *Nat Commun* **2012**, *3* (1), 1–8. https://doi.org/10.1038/ncomms2219.
(209) Cortés, L. R.; Seghilani, M.; Maram, R.; Azaña, J. Full-Field Broadband Invisibility through Reversible Wave Frequency-Spectrum Control. *Optica, OPTICA* **2018**, *5* (7), 779–786. https://doi.org/10.1364/OPTICA.5.000779.
(210) Duan, X.; Kamin, S.; Liu, N. Dynamic Plasmonic Colour Display. *Nature Communications* **2017**, *8*, 14606. https://doi.org/10.1038/ncomms14606.
(211) Kuznetsov, A. I.; Miroshnichenko, A. E.; Brongersma, M. L.; Kivshar, Y. S.; Luk'yanchuk, B. Optically Resonant Dielectric Nanostructures. *Science* **2016**, *354* (6314), aag2472. https://doi.org/10.1126/science.aag2472.
(212) Manthiram, K.; Alivisatos, A. P. Tunable Localized Surface Plasmon Resonances in Tungsten Oxide Nanocrystals. *J. Am. Chem. Soc.* **2012**, *134* (9), 3995–3998. https://doi.org/10.1021/ja211363w.
(213) Mattox, T. M.; Ye, X.; Manthiram, K.; Schuck, P. J.; Alivisatos, A. P.; Urban, J. J. Chemical Control of Plasmons in Metal Chalcogenide and Metal Oxide Nanostructures. *Advanced Materials* **2015**, *27* (38), 5830–5837. https://doi.org/10.1002/adma.201502218.
(214) Krasnok, A.; Makarov, S.; Petrov, M.; Savelev, R.; Belov, P.; Kivshar, Y. Towards All-Dielectric Metamaterials and Nanophotonics. *arXiv:1503.08857 [physics]* **2015**.
(215) García-Etxarri, A.; Gómez-Medina, R.; Froufe-Pérez, L. S.; López, C.; Chantada, L.; Scheffold, F.; Aizpurua, J.; Nieto-Vesperinas, M.; Sáenz, J. J. Strong Magnetic Response of Submicron Silicon Particles in the Infrared. *Optics Express* **2011**, *19* (6), 4815. https://doi.org/10.1364/OE.19.004815.
(216) Zhang, J.; MacDonald, K. F.; Zheludev, N. I. Near-Infrared Trapped Mode Magnetic Resonance in an All-Dielectric Metamaterial. *Optics Express* **2013**, *21* (22), 26721. https://doi.org/10.1364/OE.21.026721.
(217) Evlyukhin, A. B.; Reinhardt, C.; Chichkov, B. N. Multipole Light Scattering by Nonspherical Nanoparticles in the Discrete Dipole Approximation. *Physical Review B* **2011**, *84* (23). https://doi.org/10.1103/PhysRevB.84.235429.
(218) Grzela, G.; Paniagua-Domínguez, R.; Barten, T.; Fontana, Y.; Sánchez-Gil, J. A.; Gómez Rivas, J. Nanowire Antenna Emission. *Nano Lett.* **2012**, *12* (11), 5481–5486. https://doi.org/10.1021/nl301907f.
(219) Cao, L.; Fan, P.; Vasudev, A. P.; White, J. S.; Yu, Z.; Cai, W.; Schuller, J. A.; Fan, S.; Brongersma, M. L. Semiconductor Nanowire Optical Antenna Solar Absorbers. *Nano Lett.* **2010**, *10* (2), 439–445. https://doi.org/10.1021/nl9036627.
(220) Cao, L.; White, J. S.; Park, J.-S.; Schuller, J. A.; Clemens, B. M.; Brongersma, M. L. Engineering Light Absorption in Semiconductor Nanowire Devices. *Nature Mater* **2009**, *8* (8), 643–647. https://doi.org/10.1038/nmat2477.

(221) Schuller, J. A.; Zia, R.; Taubner, T.; Brongersma, M. L. Dielectric Metamaterials Based on Electric and Magnetic Resonances of Silicon Carbide Particles. *Phys. Rev. Lett.* **2007**, *99* (10), 107401. https://doi.org/10.1103/PhysRevLett.99.107401.
(222) Person, S.; Jain, M.; Lapin, Z.; Sáenz, J. J.; Wicks, G.; Novotny, L. Demonstration of Zero Optical Backscattering from Single Nanoparticles. *Nano Letters* **2013**, *13* (4), 1806–1809. https://doi.org/10.1021/nl4005018.
(223) Ginn, J. C.; Brener, I.; Peters, D. W.; Wendt, J. R.; Stevens, J. O.; Hines, P. F.; Basilio, L. I.; Warne, L. K.; Ihlefeld, J. F.; Clem, P. G.; Sinclair, M. B. Realizing Optical Magnetism from Dielectric Metamaterials. *Phys. Rev. Lett.* **2012**, *108* (9), 097402. https://doi.org/10.1103/PhysRevLett.108.097402.
(224) Rybin, M. V.; Filonov, D. S.; Samusev, K. B.; Belov, P. A.; Kivshar, Y. S.; Limonov, M. F. Phase Diagram for the Transition from Photonic Crystals to Dielectric Metamaterials. *Nat Commun* **2015**, *6* (1), 1–6. https://doi.org/10.1038/ncomms10102.
(225) Nian, J.-N.; Hu, C.-C.; Teng, H. Electrodeposited P-Type Cu2O for H2 Evolution from Photoelectrolysis of Water under Visible Light Illumination. *International Journal of Hydrogen Energy* **2008**, *33* (12), 2897–2903. https://doi.org/10.1016/j.ijhydene.2008.03.052.
(226) Nolan, M.; Elliott, S. D. The P-Type Conduction Mechanism in Cu2O: A First Principles Study. *Phys. Chem. Chem. Phys.* **2006**, *8* (45), 5350–5358. https://doi.org/10.1039/B611969G.
(227) Diphenyldiacetylene. https://webbook.nist.gov/cgi/inchi?ID=C886668&Mask=200#Mass-Spec (accessed 2018 -05 -28).
(228) Isotope Distribution Calculator and Mass Spec Plotter. https://www.sisweb.com/mstools/isotope.htm (accessed 2016 -09 -29).

APPENDICES

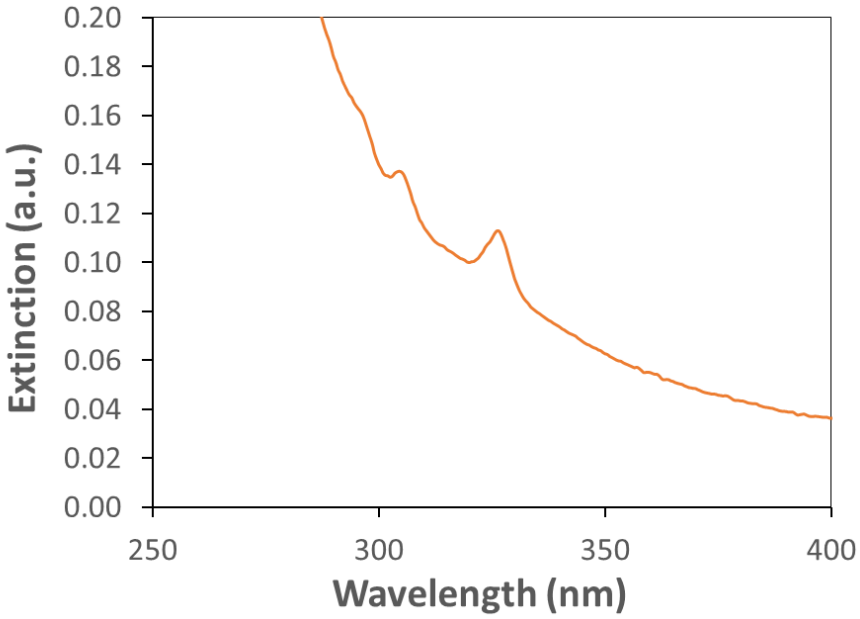

Figure S1. UV-Vis extinction spectrum of diphenyldiacetylene (DPDA).

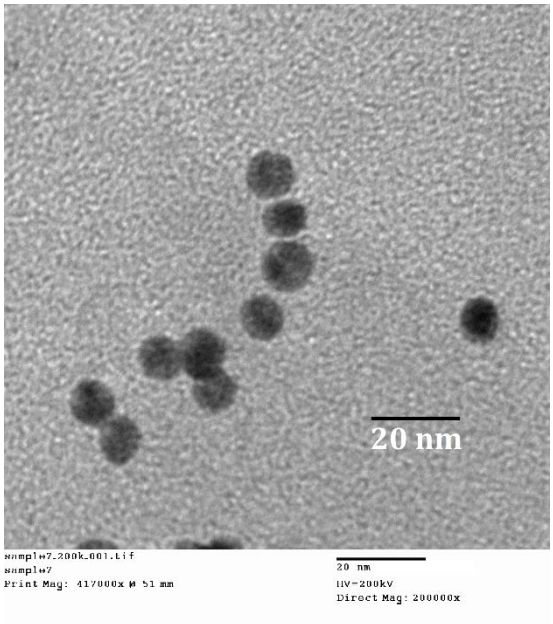

Figure S2. Representative TEM image of larger spherical Au nanoparticles obtained at the end of growth process.

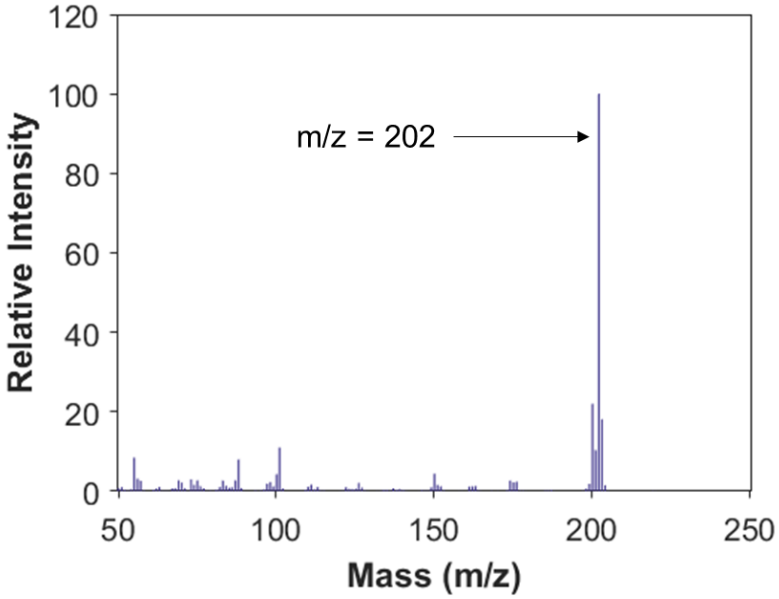

Figure S3. GC-MS (electron ionization) spectrum of diphenyldiacetylene (DPDA) observed in reaction mixture taken from Au nanoparticles-catalyzed homo-coupling of phenylacetylene. This spectrum observed in our reaction sample matches very well with the mass spectrum of DPDA reported in NIST Chemistry WebBook.[227]

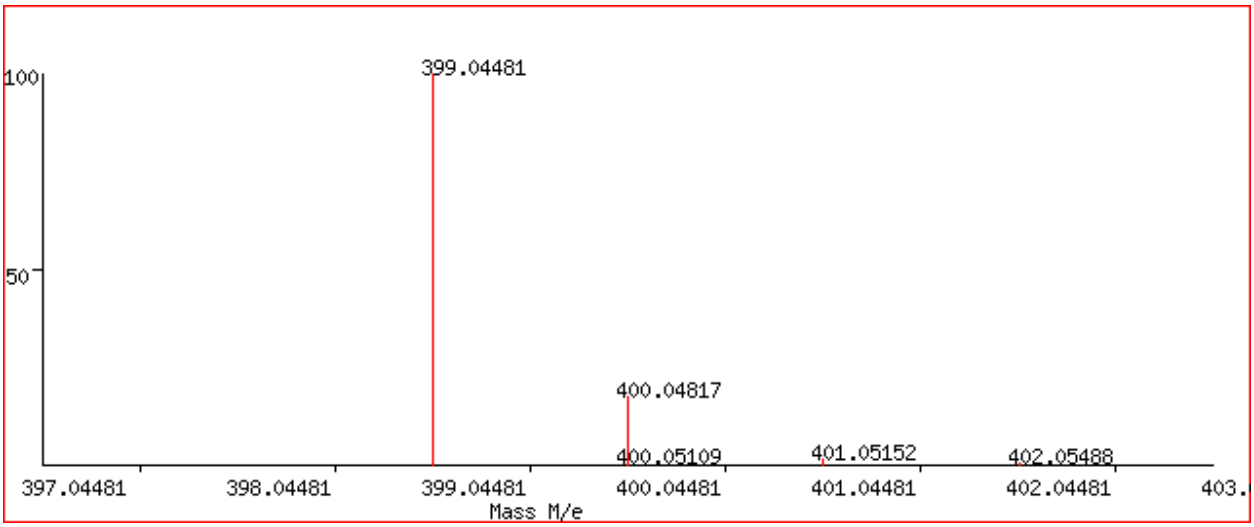

Figure S4. Predicted HR-MS spectrum for the proposed gold complex, $[Au(PA)_2]^-$ with chemical formula, $[AuC_{16}H_{10}]^-$. [228]

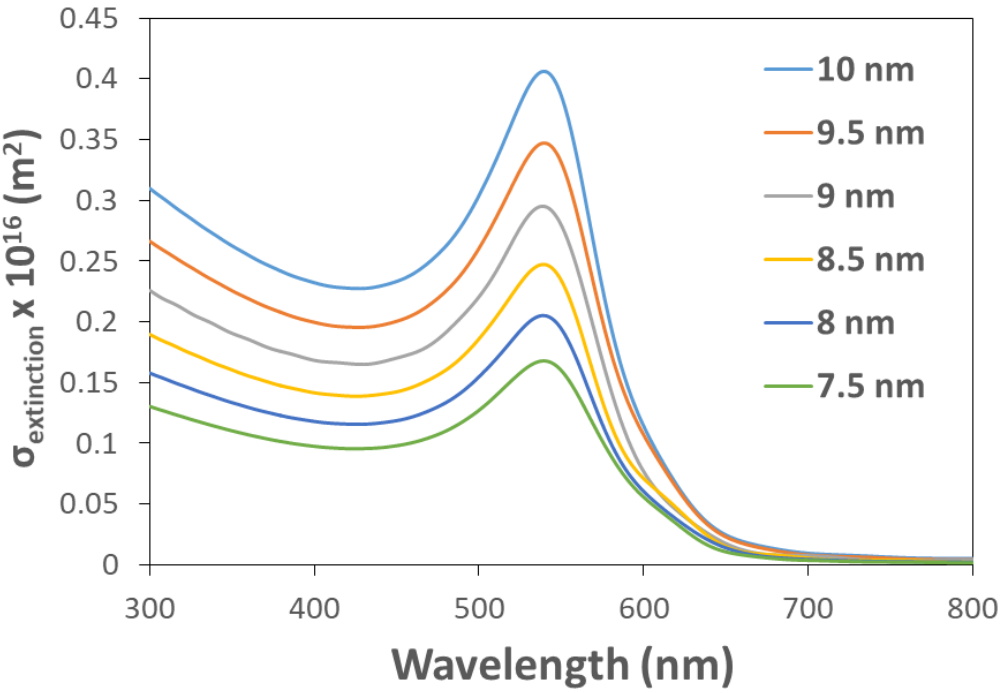

Figure S5. Simulated extinction spectra, extinction cross section as a function of wavelength, for Au nanospheres of various diameters.

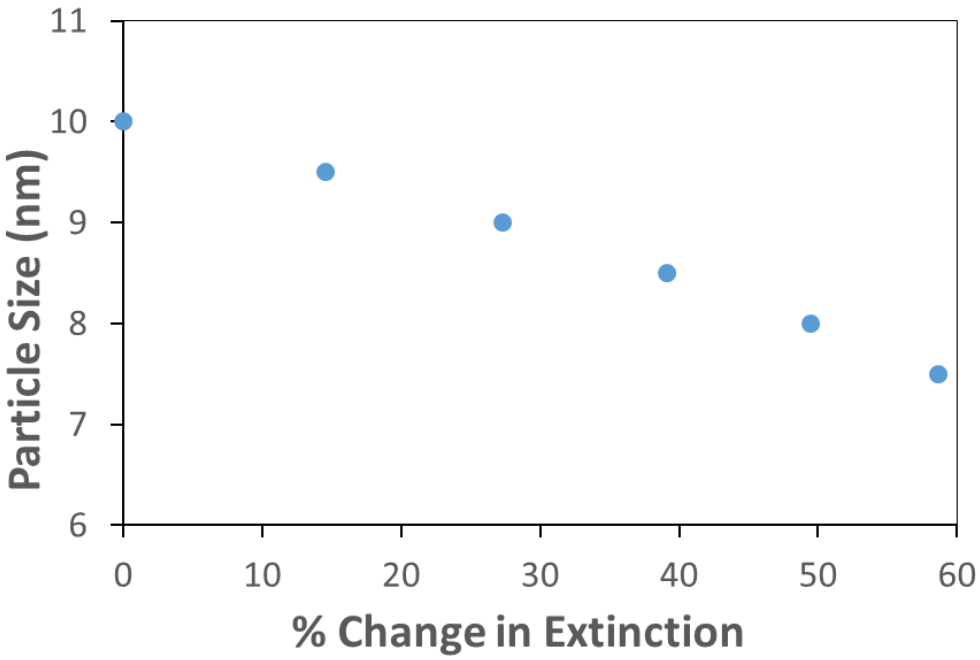

Figure S6. Particle size versus percent change in extinction for Au nanospheres at LSPR peak wavelength.

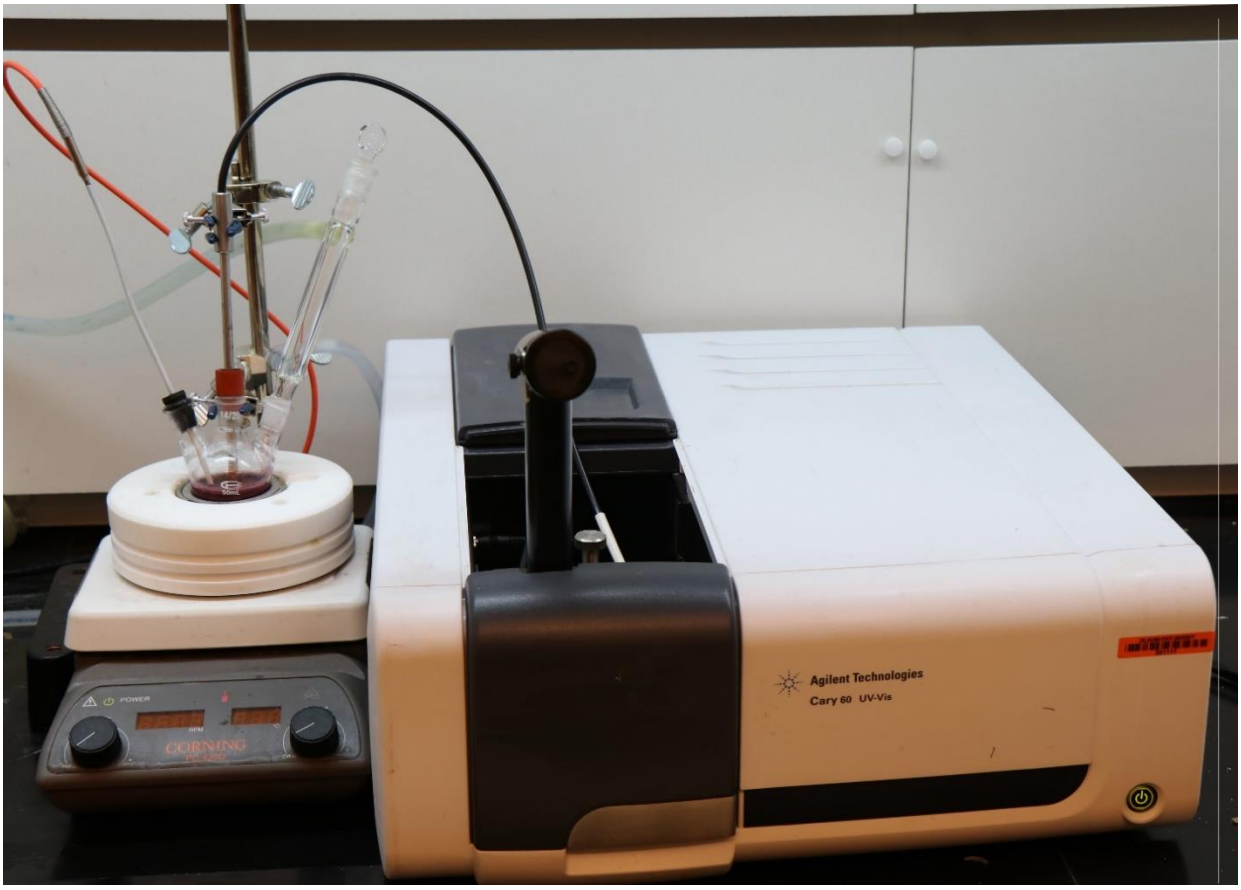

Figure S7. Picture of experimental set-up used for operando UV-Vis extinction measurements of Au nanoparticles during the C-C coupling reaction.

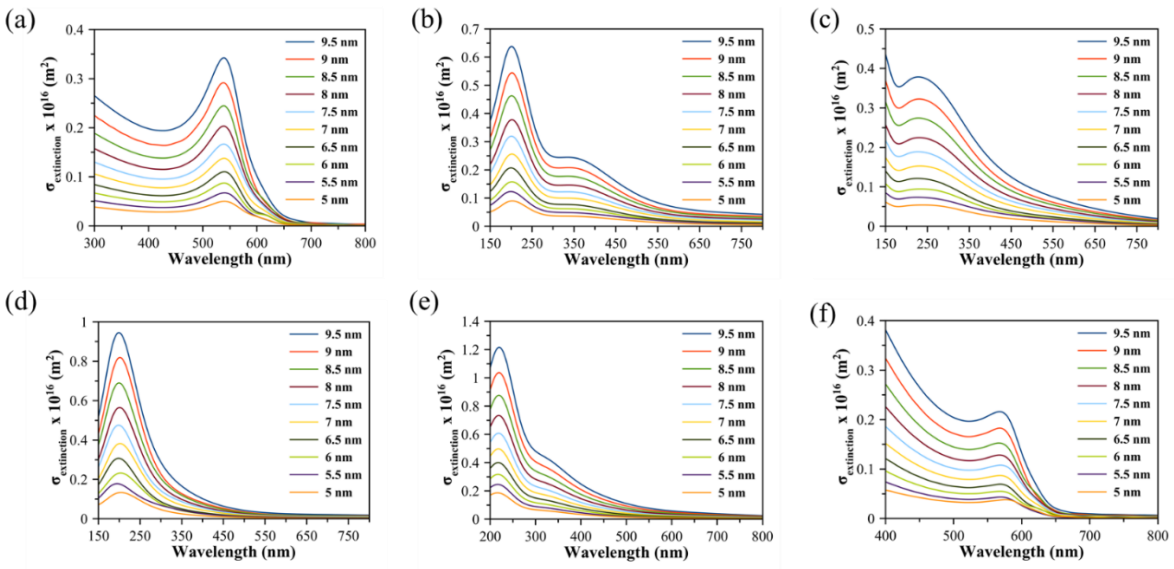

Figure S8. Finite-difference time-domain (FDTD) simulated extinction spectra for **(a)** Au, **(b)** Ni, **(c)** Pt, **(d)** Rh, **(e)** Pd, and **(f)** Cu nanoparticles of various diameters, respectively. The legends show the particle diameter.

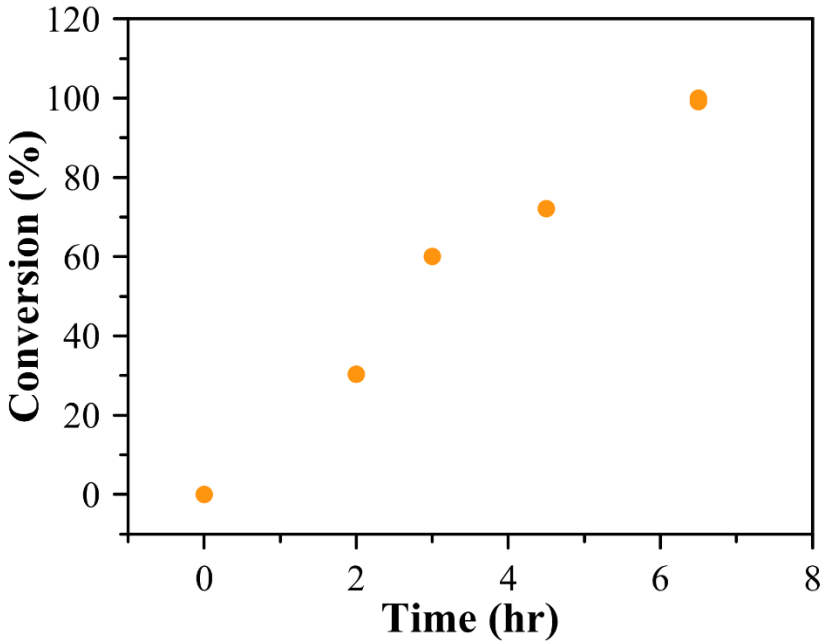

Figure S9. Phenylacetylene conversion into diphenyldiacetylene as a function of reaction time for Au nanoparticle-catalyzed C-C coupling reaction.

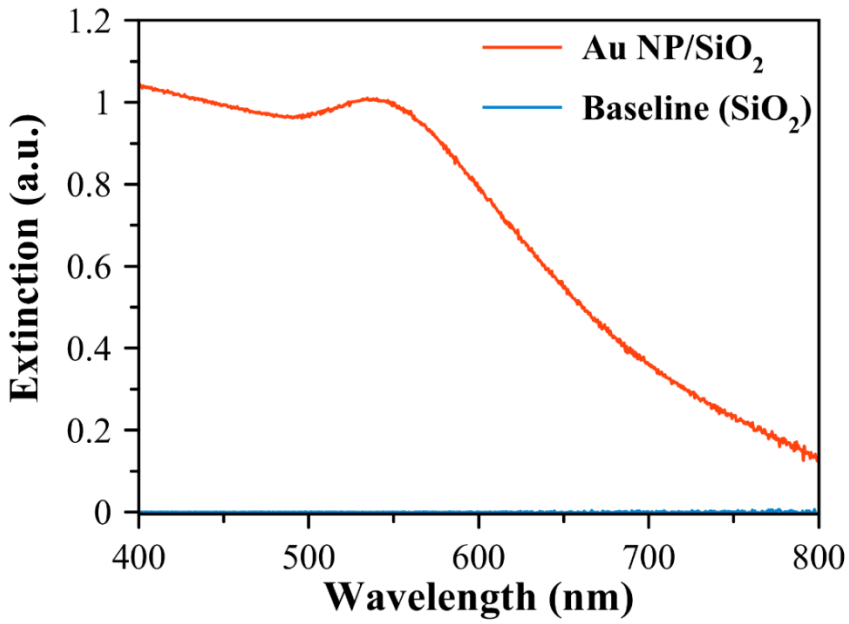

Figure S10. Representative diffuse-reflectance UV-Vis extinction spectra of Au nanoparticles supported on silica (SiO_2).

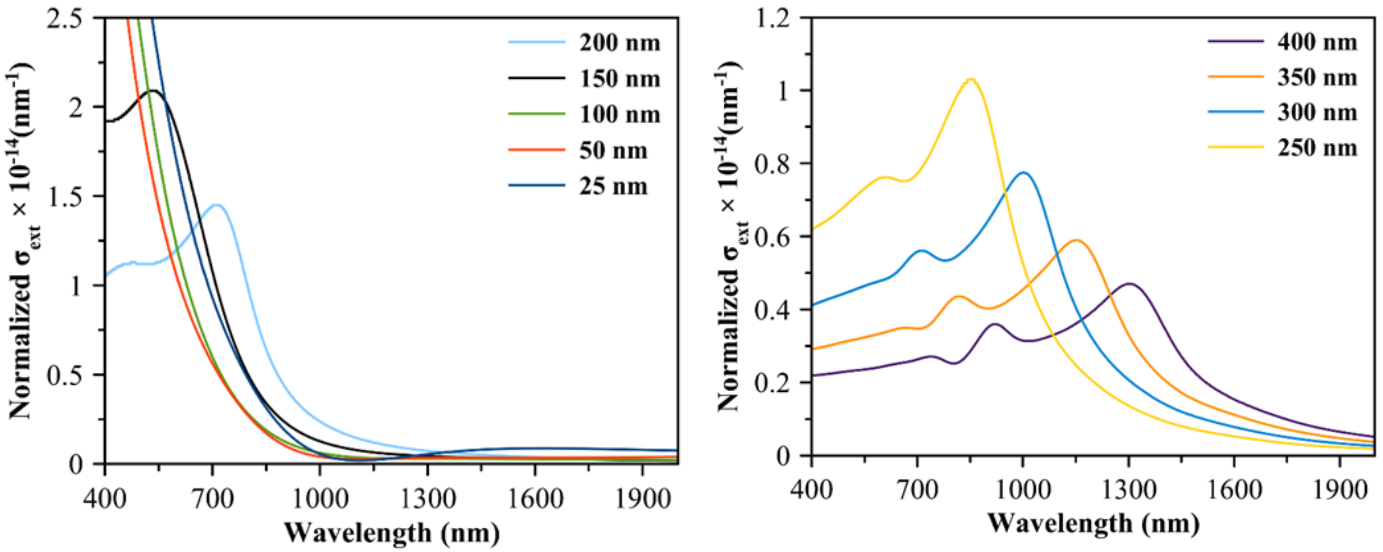

Figure S11. Simulated extinction cross section as a function of wavelength for CuO cubes of various diameters ranging from (a) 25 to 200 nm, and (b) 250 to 400 nm.

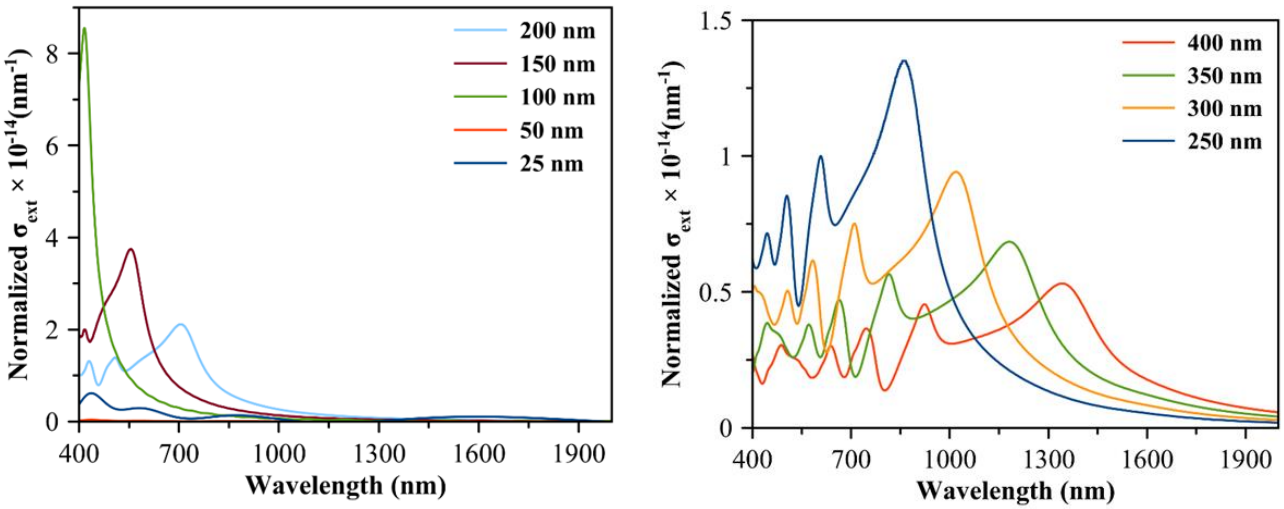

Figure S12. Simulated extinction cross section as a function of wavelength for TiO_2 cubes of various diameters ranging from (a) 25 to 200 nm, and (b) 250 to 400

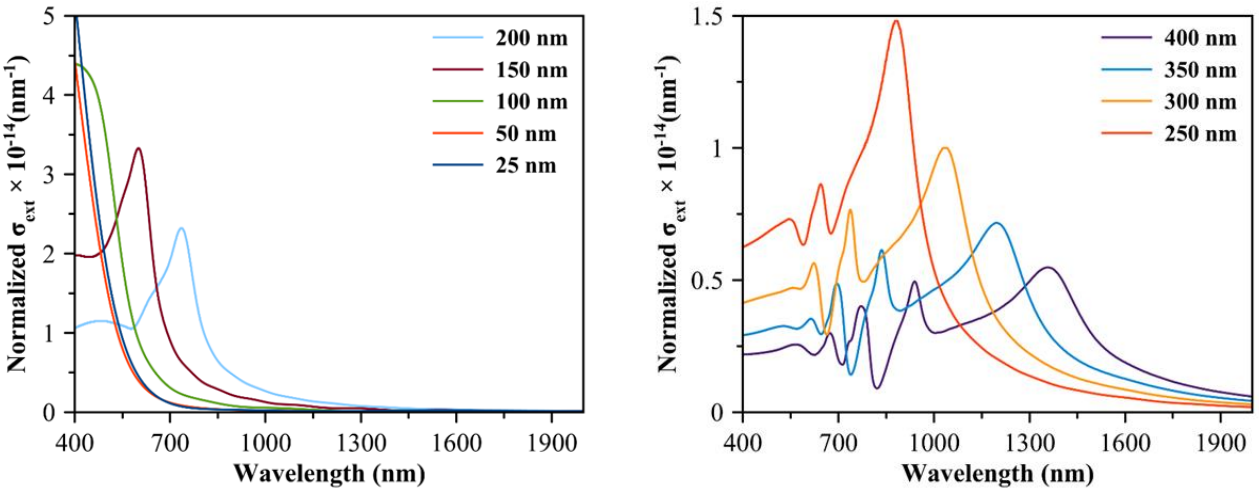

Figure 13. Simulated extinction cross section as a function of wavelength for Fe_2O_3 cubes of various diameters ranging from (a) 25 to 200 nm, and (b) 250 to 400 nm.

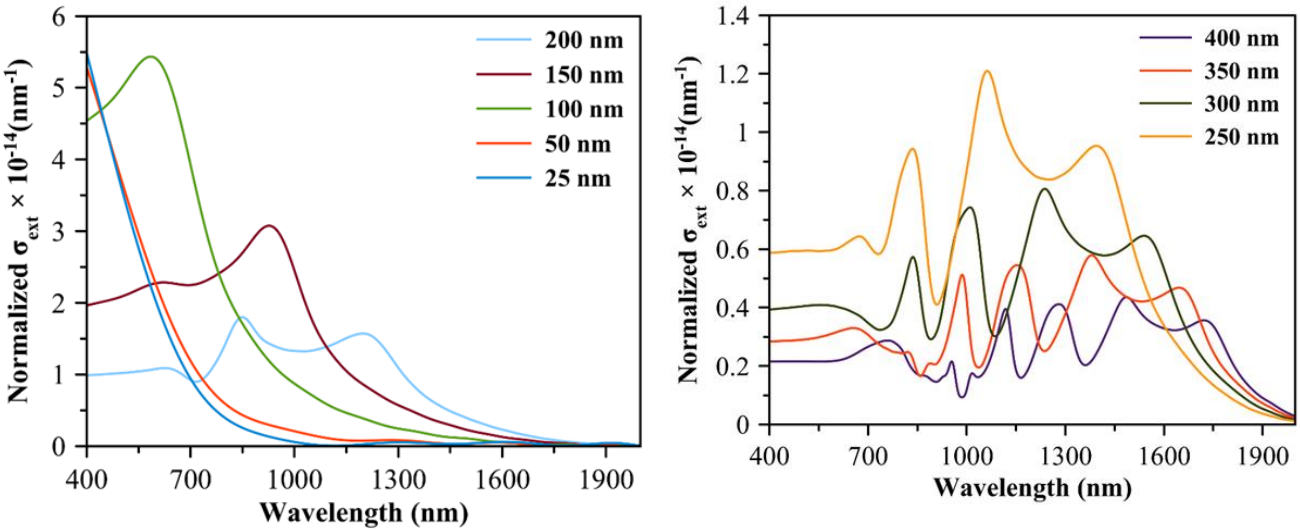

Figure 14. Simulated extinction cross section as a function of wavelength for CeO_2 Cubes of various diameters ranging from (a) 25 to 200 nm, and (b) 250 to 400 nm.

VITA

Farshid Mohammadparast

Candidate for the Degree of

Doctor of Philosophy

Thesis: EXPLORING THE OPTICAL PROPERTIES OF MIE RESONATOR NANOPARTICLES FOR CATALYTIC AND PHOTOCATALYTIC APPLICATIONS

Major Field: Chemical Engineering

Biographical:

Education:

Completed the requirements for the Doctoral of Philosophy in Chemical Engineering at Oklahoma State University, Stillwater, Oklahoma in December, 2021.
Completed the requirements for the Master of Engineering in Chemical Engineering at AmirKabir University of Technology, Tehran/Iran in 2014.

Completed the requirements for the Bachelor of Engineering in Chemical Engineering at Sistan & Baluchestan University, Zahedan/Iran in 2011.

Experience:

Professional Memberships:
Member of American Chemistry Society (ACS), American Institute of Chemical Engineers (AICHE) and Great Plain Catalysis Society (GPCS).